



The University of
Nottingham

UNIVERSITY OF NOTTINGHAM

SCHOOL OF PHYSICS AND ASTRONOMY

SIR PETER MANSFIELD MAGNETIC RESONANCE CENTRE

**Development of Arterial
Spin Labelling Methods
for Monitoring
Cerebral Haemodynamics**

Roman Wesółowski, M.Sc. Eng.

Thesis submitted to the University of Nottingham

for the degree of Doctor of Philosophy

December, 2009

BEST COPY

AVAILABLE

Variable print quality

Abstract

The work described in this thesis was carried out at the Sir Peter Mansfield Magnetic Resonance Centre at the University of Nottingham between March 2006 and December 2009. All work described in this thesis was performed by the author, except where indicated. This thesis aims to develop and implement ASL techniques to measure haemodynamic responses to neural activity.

The development of a new technique Double Acquisition Background Suppression (DABS) is presented as a remedy for a newly discovered artefact affecting Philips Achieva 7 T scanners and other sources of variation in baseline signals such as physiological noise. The new technique (DABS) was developed for simultaneous acquisition of ASL (with suppressed static tissue signal) and BOLD data using the FAIR scheme. This method not only provided a solution to obtaining ASL data at 7 T, despite the Roman Artefact, but also proved to reduce the contribution of physiological noise to ASL images, which is problematic, especially at ultra-high magnetic field strengths. The statistical verification was carried out based on the neural activation induced by a finger-tapping stimulus.

A simplified model for quantifying CBV_a with the Look-Locker sampling method is proposed in this thesis to overcome the need for the Step-wise Compartmental Model (SCM). The Look-Locker sampling scheme acquires multiple readout pulses following the labelling and provides an estimation of transit time as well as CBV_a . Here the simplified model is used to assess changes due

to visual stimulation and validated against the SCM model.

The application of LL-FAIR to form CBF and CBV_a weighted data with improved SNR compared to traditional single TI FAIR technique is then shown. This method uses a summation over LL-EPI readout pulses and is used to assess the temporal characteristics and absolute changes in CBF and CBV_a haemodynamic responses to a short (4.8 s) and long (9.6 s) visual stimulus.

LL-FAIR methods are then used to appraise the neural coupling of haemodynamic parameters and assess Grubb's relationship. CBF and CBV_a data were collected together with CBV_{tot} data from a bolus injection of contrast agent. Assessing Grubb's power-law ($CBV_{tot} = CBF^\alpha$) for neuronal activation, which was originally derived in primates during a steady state response of hypercapnia, α was found in this human study to be between 0.22 ± 0.08 and 0.29 , dependent on the analysis method. In addition, the power-law relationship between CBV_{tot} and CBV_a was assessed, and resulted in a similar relation, yielding $\alpha_{TA} = 0.42 \pm 0.14$ and 0.40 . Since CBF is thought to be driven by CBV_a the power-law between these parameters was also tested with a value of $\alpha_{FA} = 1.35 \pm 0.64$ and 1.21 , found in close agreement with earlier animal work.

I dedicate this thesis to my family for sacrificing many life's perks in order to provide for my education and for a gargantuan moral support when needed the most.

Niniejszą pracę dedykuję mojej Rodzinie w podziękowaniu za poświęcenie, na które zdobyli się wszyscy jej członkowie, by umożliwić mi dalszą edukacją oraz za ogromne wsparcie moralne w chwilach, gdy najbardziej go potrzebowałem.

Acknowledgements

I would like to thank my supervisors, Penny Gowland and Susan Francis, for guiding my work and giving me the opportunity to expand my knowledge and, on more personal note, for being good friends.

I would also like to acknowledge all my colleagues from the "downstairs office" for creating an exceptionally pleasant working environment. Special thanks to Rosita Panchuelo for endless MR discussions (many times over certain beverages) and being a great friend, Mike Poole and Emily Leverton for creating a special MATLAB function ("help mike" and "help emily") at the beginning of my studies, and others that have contributed to creating this thesis in any way.

Also special thanks to my sister Ewa and my friends Sid Baker and Jon Reynolds for taking care of all my bureaucratic ties I had to leave behind at various places in the world.

Contents

1	Introduction	1
2	Nuclear Magnetic Resonance Theory	4
2.1	Single Spin	6
2.2	Bulk Magnetisation	9
2.2.1	Rotating Reference Frame	10
2.2.2	Radio Frequency Excitation Pulses	12
2.2.3	Relaxation	14
2.2.3.1	Longitudinal T_1 Relaxation	15
2.2.3.2	Transverse T_2 Relaxation	17
2.2.3.3	Transverse T_2^* Relaxation	18
2.3	Bloch Equations	20
2.3.1	Bloch Equation without Relaxation	20
2.3.2	Bloch Equation with T_1 and T_2 Relaxation	21
3	Magnetic Resonance Imaging and Instrumentation	23
3.1	Fourier Transform	23
3.2	k-Space	25
3.3	Imaging Gradients	27
3.3.1	Frequency-Encoding Gradient	28
3.3.1.1	Gradient Echo	29
3.3.1.2	Spin Echo	30

3.3.1.3	Quantitative Description	32
3.3.2	Phase-Encoding Gradient	33
3.3.3	Slice-Selection Gradient	36
3.4	Two-Dimensional Acquisition	38
3.5	Echo Planar Imaging	40
3.6	Instrumentation	44
3.6.1	Main Magnet	45
3.6.2	Shimming Coils	46
3.6.3	Gradient Coils	46
3.6.4	RF System	47
4	Perfusion and Functional Imaging Techniques	48
4.1	Overview of Techniques to Measure Blood Flow and Volume . .	48
4.1.1	PET and SPECT	49
4.1.2	Angiography	49
4.2	Arterial Spin Labelling - What Does It Measure?	52
4.2.1	Cerebral Blood Flow (CBF) and Perfusion	53
4.2.2	Arterial Cerebral Blood Volume (CBV _a)	53
4.3	ASL Methods	54
4.3.1	Continuous ASL (CASL)	55
4.3.2	Pulsed ASL (PASL)	57
4.3.2.1	STAR	58
4.3.2.2	PICORE	59
4.3.2.3	TILT	61
4.3.2.4	FAIR	61
4.3.3	Image Readout	64
4.4	ASL Applications: Functional and Pharmaceutical	64
4.5	Blood Oxygenation Level Dependent: Origin and Limitations .	66

5	Perfusion Imaging: Removing Noise Contributions from Static Tissue	69
5.1	The Roman Artefact	69
5.1.1	3 T versus 7 T: Comparison	70
5.1.2	Effect of Scan Parameters on the Magnitude of the Roman Artefact	72
5.1.2.1	Mechanical Vibrations Effect	72
5.1.2.2	RA Dependence on Head Coil	73
5.1.2.3	RA Dependence on Phase-Encoding Direction and Slice Orientation	73
5.1.2.4	RA Dependence on Readout Flip Angle, Repetition Time, and Echo Time	75
5.2	Double Acquisition Background Suppression (DABS)	78
5.2.1	Optimising Timing of BS Pulses	80
5.2.1.1	3 T Optimisation	82
5.2.1.2	7 T Optimisation	91
5.2.1.3	Perfusion-Weighted Images Acquired at 7 T Using FAIR-DABS	96
5.2.2	Assessing Advantages of DABS to fMRI Studies	98
5.2.2.1	Method	98
5.2.2.2	Image Analysis	99
5.2.2.3	Results	100
5.3	Discussion	107
6	Simple model of measuring Arterial Cerebral Blood Volume (CBV_a) from LL-FAIR	108
6.1	Theory	112
6.1.1	Traditional FAIR	112

6.1.2	Look-Locker FAIR	117
6.2	Experimental Methods and Data Analysis	121
6.3	Results	122
6.4	Discussion	127
7	Applications	128
7.1	Assessing the Temporal Responses of CBF and CBV_a Measures	129
7.1.1	Experimental Methods and Data Analysis	130
7.1.2	Results and Discussion	133
7.1.2.1	CBF	133
7.1.2.2	CBV_a	137
7.1.3	Conclusions	139
7.2	Functional Changes in CBV_a , CBF and contrast enhanced CBV_{tot}	140
7.2.1	Experimental Methods and Analysis	142
7.2.2	Results	147
7.2.3	Discussion	149
7.3	Conclusions	157
8	Summary	159
	Glossary	162
	Bibliography	165

Chapter 1

Introduction

Arterial Spin Labelling (ASL) methods were first introduced over fifteen years ago [1], however the idea of measuring blood in vessels and perfusion using saturated and excited spins was suggested a few years earlier [2]. Despite this, ASL is still very much a research tool though clinical interest is now rapidly growing. The reason for this is that ASL measurements are non-invasive and can provide not only qualitative information (in the form of Perfusion Weighted (PW) images) but also quantitative measures of perfusion (in $\left[\frac{\text{ml}}{100\text{g}\cdot\text{min}}\right]$). This being very important in diagnostic medicine of acute and chronic diseases affecting blood flow and perfusion. Also the interest in ASL approaches for pharmaceutical trials have started to increase, since the long term and frequent monitoring using a natural contrast (of ASL) is possible. New ASL techniques are being developed and existing methods improved. This is allowing ASL to become a more powerful tool every day, and this thesis presents an example of such measures.

Chapter 2 introduces the phenomenon of Nuclear Magnetic Resonance (NMR) outlining the key basic physics concepts behind it. Definitions of important terms, and explanations of the basic physics principles are provided along with the defining equations key to the main subject of this chapter.

The concept of Magnetic Resonance Imaging (MRI) is outlined in Chapter 3. Using notations from Chapter 2, the basic idea behind MRI is explained and the main hardware components of an MR system introduced. This chapter elaborates on the role of various equipment in forming an image using the NMR phenomenon.

Chapter 4 introduces different techniques used to measure blood flow and perfusion. The imaging techniques using MR are explained and the various ASL pulse sequences described, which are the main subject of this thesis. The application of ASL to functional MRI (fMRI) and the typical Blood Oxygenation Level Dependent (BOLD) contrast used for fMRI are introduced.

Chapters 5, 6 and 7 are the experimental chapters of this thesis. In Chapter 5 advantages and challenges of acquiring ASL data at ultra-high (7 T) field are described. The first section of this chapter describes an artefact discovered on all Philips 7 T scanners which impacts on ASL data collection. The second part proposes a remedy, allowing ASL data acquisitions, which also benefits in reduction of other noise signals associated with high and ultra-high field scanning, such as physiological noise.

The second experimental chapter, Chapter 6, addresses the quantification of Arterial Cerebral Blood Volume (CBV_a) using traditional FAIR technique and a Look-Locker EPI (LL-EPI) acquisition. An alternative quantification method to quantify (CBV_a) to the Stepwise Compartmental Model (SCM) used previously for the LL-EPI acquisition technique is proposed and verified.

Chapter 7 introduces applications of the LL-EPI acquisition technique with FAIR scheme, particularly interesting for pharmaceutical trials – a single acquisition approach. Also, a cross-field study combining three measures (CBV_a , CBF and CBV_{tot}) to obtain more detailed information of their contribution in haemodynamic processes, is conducted in this chapter.

This thesis concludes with a summary of the findings in Chapter 8. This is

followed by a brief outline of potential applications and suggested future work can also be found. For example, perhaps in the future, it will be possible to obtain fMRI images using ASL in real time within just an ultra-fast single trial – reconstructing images just like the one below...



Chapter 2

Nuclear Magnetic Resonance

Theory

Nuclear Magnetic Resonance (NMR) is one of many methods used by science and technology nowadays to investigate matter. NMR was first described independently by Purcell [3] and Bloch [4] in 1946. Six years later these two scientists were awarded a Nobel Prize for their achievements. In principle, NMR uses magnetic properties of nuclei as well as a radio frequency electromagnetic wave for excitation purposes. Rotating particles possess an angular momentum vector \vec{J} (Fig. 2.1), which points in the direction orthogonal to the rotating plane. Spin angular momentum \vec{S} (spin) is a particle's intrinsic property [5]. Not all nuclei are NMR sensitive, only certain nuclei that have non-zero spin can be used from the NMR perspective. Associated with the spin is magnetic moment vector $\vec{\mu}$, which expresses the particles' interactions with an external magnetic field. The spin angular momentum and the magnetic moment are proportional:

$$\hat{\mu} = \gamma \hat{S}, \quad (2.1)$$

where $\hat{\mu}$ and \hat{S} are quantum mechanical operators and γ is the gyromagnetic ratio, a characteristic constant of a nucleus, typically described in units of $[\frac{\text{MHz}}{\text{T}}]$,

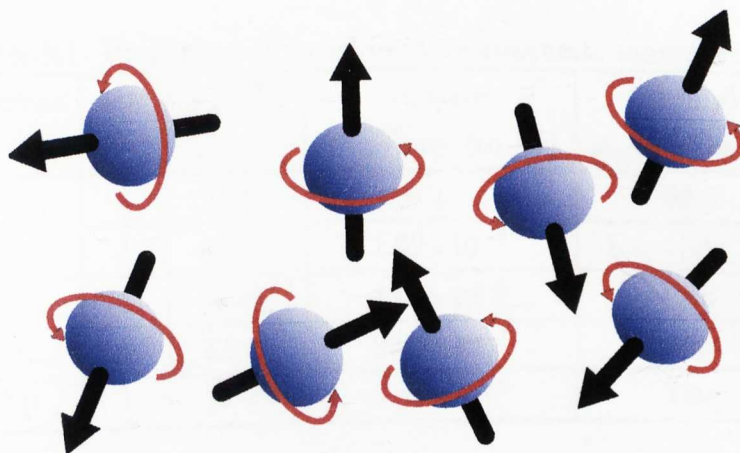


Figure 2.1: Schematic of various directions of the angular momentum of rotating particles.

see Table 2.1. The magnetic energy E_{mag} of these interactions can be determined as a scalar product of the particle's magnetic moment $\vec{\mu}$ and the external magnetic field \vec{B} (Eq. 2.2).

$$E_{\text{mag}} = -\vec{\mu} \cdot \vec{B} \quad (2.2)$$

The negative sign indicates that a lower energy state corresponds to parallel vectors and antiparallel vectors results in a higher energy configuration.

Interactions of particles having a magnetic moment with an external magnetic field form the core of the NMR phenomenon. NMR interest lies in nuclei with high γ such as hydrogen ^1H , carbon ^{13}C , nitrogen ^{14}N , sodium ^{23}Na , or phosphorus ^{31}P . The values of the gyromagnetic ratio, together with relative sensitivity of nuclei compared to ^1H and relative abundance are shown in Table 2.1. Hydrogen nuclei can be seen to be the most common and widely present in biological matter. Since no other nuclei was used in any experiment in this thesis, ^1H NMR is the main subject of this chapter.

Table 2.1: Properties of nuclei used for magnetic resonance [5].

nucleus	spin	γ [$\frac{\text{MHz}}{\text{T}}$]	relative sensitivity (to ^1H)	natural abundance [%]
^1H	$\frac{1}{2}$	42.58	1	99.8
^{13}C	$\frac{1}{2}$	10.71	1.59×10^{-2}	1.11
^{14}N	1	3.08	1.01×10^{-3}	99.6
^{23}Na	$\frac{3}{2}$	11.26	9.25×10^{-2}	100
^{31}P	$\frac{1}{2}$	17.24	6.63×10^{-2}	100

2.1 Single Spin

In quantum mechanics, both angular momentum and spin angular momentum are quantised, which means that there are only discrete energy levels that a particle (or system) can occupy. The angular momentum quantum number, J , represents the quantised energy levels, therefore can only have positive integer numbers ($J = 0, 1, 2, \dots$). Total angular momentum, L_{tot} , represents the entire group of stable states of the system and can be calculated from:

$$L_{\text{tot}} = \hbar \sqrt{J(J+1)}, \quad (2.3)$$

where \hbar is the Planck constant ($6.626 \times 10^{-34} \text{ J} \cdot \text{s}$) divided by 2π . The measurable values of the the z-component of the angular momentum, L_z , are given by:

$$L_z = M_j \hbar, \quad (2.4)$$

where M_j is the azimuthal (or projectional) quantum number, which has $2J+1$ values ($M_j = -J, -J+1, -J+2, \dots, J-2, J-1, J$). M_j physically determines the number of degenerate (the same) energy states that the system possesses in the absence of the external magnetic field. Total spin angular momentum S_{tot} uses the same form of equation, (Eq. 2.3), however S can have posi-

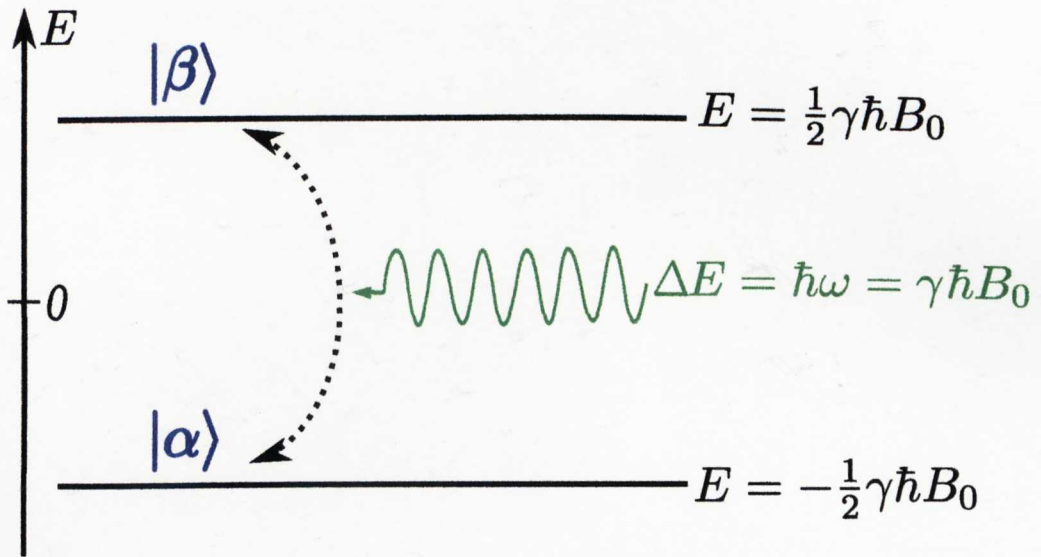


Figure 2.2: Energy level diagram of the hydrogen nucleus (spin $\frac{1}{2}$) in a magnetic field B_0 . Transitions can be induced between the spin states by adding energy ΔE , equal to the difference between energy levels of the split, to the system.

tive integer numbers ($S = 0, 1, 2, \dots$) for particles called “bosons” and half-integer numbers ($S = \frac{1}{2}, \frac{3}{2}, \frac{5}{2}, \dots$) for particles called “fermions”. Similarly, the azimuthal quantum number for spin angular momentum has $2S+1$ values ($M_s = -S, -S+1, -S+2, \dots, S-2, S-1, S$). The energy levels are also quantised and in the case of ^1H (a $\frac{1}{2}$ spin system) this concept is crucial in understanding the effects of the external magnetic field on spins. For an $S = \frac{1}{2}$ spin system, the measurable z -component of the total spin angular momentum M_s has $2 \cdot \frac{1}{2} + 1 = 2$ values of $-S$ ($-\frac{1}{2}$) and $+S$ ($+\frac{1}{2}$)

Quantum-mechanically, a presence of the external magnetic field causes the degeneracy of both angular momentum and spin angular momentum to break down, splitting them into $2J+1$ and $2S+1$ sublevels, respectively. This phenomenon is known as the “Zeeman effect”. The allowed energy levels are also split in the same manner, as shown in Figure 2.2. However, because of the rotating nature of the particles, spins actually precess around \vec{B}_0 (Fig. 2.3) with an angular velocity ω_L called Larmor frequency. The Larmor frequency is

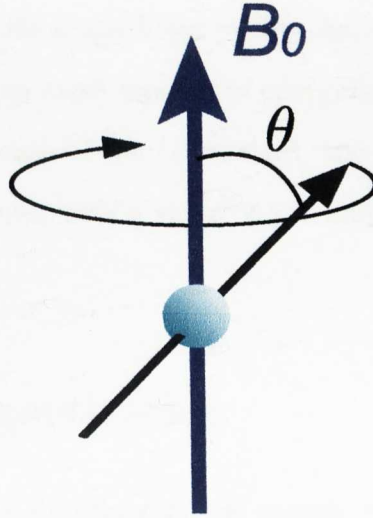


Figure 2.3: Schematic of the spin precession in presence of external magnetic field B_0 with θ being a precession angle, which only depends on the spin state.

proportional to the magnetic field and is given by

$$\omega_L = -\gamma B_0. \quad (2.5)$$

As stated earlier, from the NMR perspective, only nuclei of high γ such as hydrogen ^1H , are interesting.

The energy states (Fig. 2.2) of the Zeeman splitting depend on the spin configuration (spin number S), and can be derived from a simple energy equation $E = h\nu$:

$$E_S = -S\hbar\gamma B_0. \quad (2.6)$$

As mentioned before, there are two spin configurations for ^1H in a magnetic field, therefore there are two energy levels. The energy difference between these two levels is $\Delta E = E_\beta - E_\alpha$ (where α and β represent the parallel and antiparallel spin, respectively, with reference to the magnetic field \vec{B}_0) and is equal to:

$$\Delta E = \hbar\gamma B_0. \quad (2.7)$$

To cause excitation of spins in the lower energy state (α) to the higher energy state (β), there must be an exact amount of energy (ΔE) absorbed by the particle to the system. In case of the ^1H nucleus, this energy falls in the radio frequency energy spectrum, with a value of 128 and 298 MHz for 3 and 7 T, respectively.

2.2 Bulk Magnetisation

Despite NMR having its origin at the atomic level, in MRI experiments we actually measure a macroscopic phenomenon. Figure 2.4 shows the state of thermal equilibrium of multiple magnetic moments (about 6.7×10^{22} protons per 1 cm^3 of water) in the external magnetic field. Superposition of those moments is called the “bulk magnetisation” $\sum \vec{\mu} = \vec{M}$, however for simplicity, I will refer to this as the “magnetisation”. There are more proton’s spins occupying the lower energy level of the Zeeman splitting rather than the higher

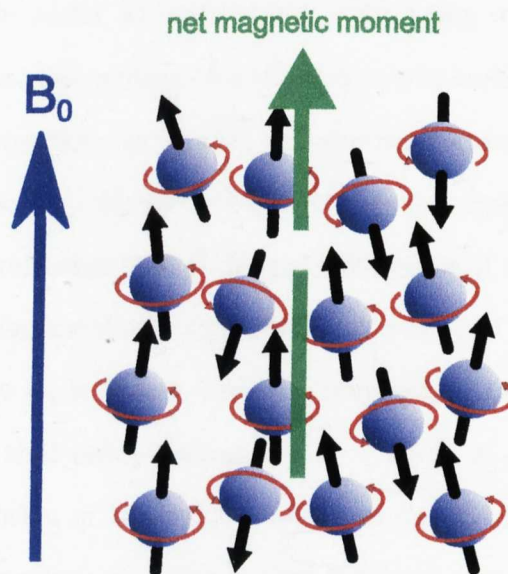


Figure 2.4: Schematic of the thermal equilibrium of spins in an external magnetic field \vec{B}_0 .

energy state. The distribution of both parallel and antiparallel number of spins in the magnetic field follows the Boltzmann distribution (Eq. 2.8):

$$\frac{N_\beta}{N_\alpha} = e^{-\frac{\Delta E}{k \cdot T}} = e^{-\frac{\hbar \gamma B_0}{k \cdot T}}, \quad (2.8)$$

where N_α and N_β indicate the number of parallel and antiparallel spins, respectively, ΔE is the difference between the energy levels of both states, “ k ” is the Boltzmann constant ($= 1.38 \times 10^{-23} \frac{\text{J}}{\text{K}}$), and T is the temperature. The z -component of the magnetisation (in the direction of the external magnetic field), M_z , defines the thermal equilibrium of the system, $M_z = M_0$ and thus depends on the temperature T and the strength of the external magnetic field B_0 .

2.2.1 Rotating Reference Frame

Behaviour of magnetisation in the external magnetic field and excitation processes are made easier to understand when using a “rotating reference frame”. The precessional motion of a single spin was explained in Section 2.1, and the net magnetisation vector, \vec{M} , also precesses around the \vec{B}_0 field with the Larmor frequency ω_L . Figure 2.5(a) shows the precessing magnetisation \vec{M} in the “laboratory reference frame” (x, y, z). However, if a “rotating reference frame” (x', y', z') that rotates around the z -axis (the axis of the \vec{B}_0 field) with the angular velocity ω , is chosen then the magnetisation rotates at a slower angular velocity in that reference frame (Fig. 2.5(b)). If $\omega = \omega_L$, we “freeze” the precessional motion of the magnetisation in the rotating reference frame and \vec{M} becomes a stationary vector in that reference frame.

The mathematical description of the transition between the two reference frames is easiest to show on an arbitrary, time-dependent vector $\vec{p}(t)$ in the laboratory reference frame whose three components in Cartesian coor-

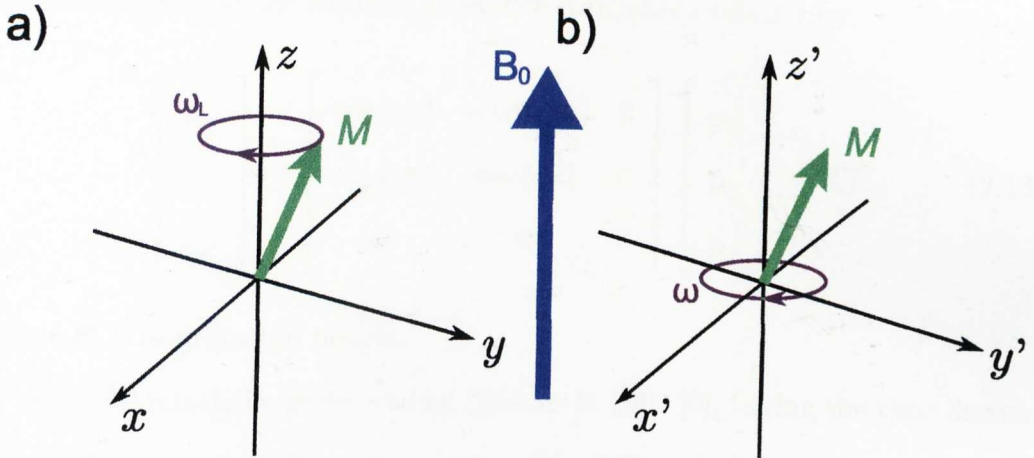


Figure 2.5: Comparison of two reference frames, laboratory (a), where the magnetisation vector \vec{M} precesses around the direction of the external magnetic field \vec{B}_0 with the Larmor frequency ω_L , and rotating (b), where the reference frame rotates around the \vec{B}_0 (z -axis) with the frequency ω . When $\omega = \omega_L$, \vec{M} becomes a stationary vector.

coordinates are $p_x(t)$, $p_y(t)$, $p_z(t)$:

$$\vec{p}(t) = p_x(t)\hat{x} + p_y(t)\hat{y} + p_z(t)\hat{z}, \quad (2.9)$$

where the symbol $\hat{}$ denotes a unit vector. The same vector in the rotating reference frame will be:

$$\vec{p}'(t) = p_{x'}(t)\hat{x}' + p_{y'}(t)\hat{y}' + p_{z'}(t)\hat{z}', \quad (2.10)$$

The z -component is equal in both reference frames whilst, for the transverse axes, the relation is:

$$x' = x \cos(\omega t) - y \sin(\omega t) \quad (2.11)$$

$$y' = x \sin(\omega t) + y \cos(\omega t), \quad (2.12)$$

where ω is the angular velocity of the rotating reference frame (Fig. 2.5(b)). Considering Equations 2.11 and 2.12 and that $z' = z$, the components of both

the laboratory and the rotating reference frames are related by:

$$\begin{bmatrix} p_{x'} \\ p_{y'} \\ p_{z'} \end{bmatrix} = \begin{bmatrix} \cos(\omega t) & -\sin(\omega t) & 0 \\ \sin(\omega t) & \cos(\omega t) & 0 \\ 0 & 0 & 1 \end{bmatrix} \begin{bmatrix} p_x \\ p_y \\ p_z \end{bmatrix} = \mathfrak{R} \vec{p}, \quad (2.13)$$

where \mathfrak{R} is the rotation matrix.

A useful relation was derived by Slichter in 1989 [6], taking the time derivative of the given time-dependent vector (Eq. 2.9):

$$\left(\frac{d\vec{p}(t)}{dt} \right)_{\text{lab}} = \left(\frac{d\vec{p}(t)}{dt} \right)_{\text{rot}} + \vec{\Omega} \times \vec{p}(t) \quad (2.14)$$

$$\vec{\Omega} = -\omega \hat{z}, \quad (2.15)$$

where the subscripts “lab” and “rot” represent laboratory and rotating reference frames respectively, and $\vec{\omega}$ is a rotational angular velocity vector (the negative sign refers to the clock-wise rotation, shown as a vector pointing in the negative z-direction in Figure 2.5).

The introduction of the rotating reference frame considerably simplifies many explanations of NMR phenomena.

2.2.2 Radio Frequency Excitation Pulses

Radio Frequency (RF) excitation pulses are only one type of RF pulses, however they are very important as they play a role in all of MR sequences – creating the MR signal which is subsequently sampled. RF pulses create a modulation of the net magnetisation in the direction orthogonal to the external magnetic field \vec{B}_0 (conventionally, “x” is the direction of the RF pulse and “z” is the direction of the external magnetic field) so that the magnetisation is redirected from its equilibrium state towards the direction of the applied mod-

ulation. Mathematically, the behaviour of the magnetisation can be described by the Bloch equations (see also Section 2.3):

$$\left(\frac{d\vec{M}}{dt}\right) = \gamma\vec{M} \times \vec{B} \quad (2.16)$$

For an RF pulse applied in the x-direction with RF frequency ω_{RF} , the Bloch equation in the rotating frame is:

$$\left(\frac{d\vec{M}}{dt}\right)_{\text{rot}} = \gamma\vec{M} \times \left[\hat{x}B_1(t) + \hat{z}\left(B_0 - \frac{\omega_{\text{RF}}}{\gamma}\right) \right], \quad (2.17)$$

where $B_1(t)$ is a time-dependent radio-frequency wave function. The angle that the magnetisation \vec{M} is diverted from the z-direction is termed the flip angle (θ), and can be determined by the area under the curve representing the amplitude of the modulation (B_1), expressed as:

$$\theta(t) = \gamma \int_{t'=0}^t B_1(t') dt' \quad (2.18)$$

Expressing Eq. 2.17 in spherical coordinates and assuming initial conditions ($M_x = 0, M_y = 0, M_z = M_0$ at $t = 0$), results in:

$$\begin{aligned} M_x &= M_0 \cos \phi \sin \theta \\ M_y &= M_0 \sin \phi \cos \theta \\ M_z &= M_0 \cos \theta \end{aligned} \quad (2.19)$$

where ϕ is an angle between the magnetisation and x-axis in the transverse plane (physically, ϕ is an angular representation between Larmor frequency and RF pulse frequency; $\phi \equiv \Delta\omega = \gamma B_0 - \omega_{\text{RF}}$) and θ is an angle that the magnetisation forms with the z-axis.

Figure 2.6 shows an example of the “normal” laboratory reference frame (Fig. 2.6(a)) and the rotating reference frame (Fig. 2.6(b)). A fairly compli-

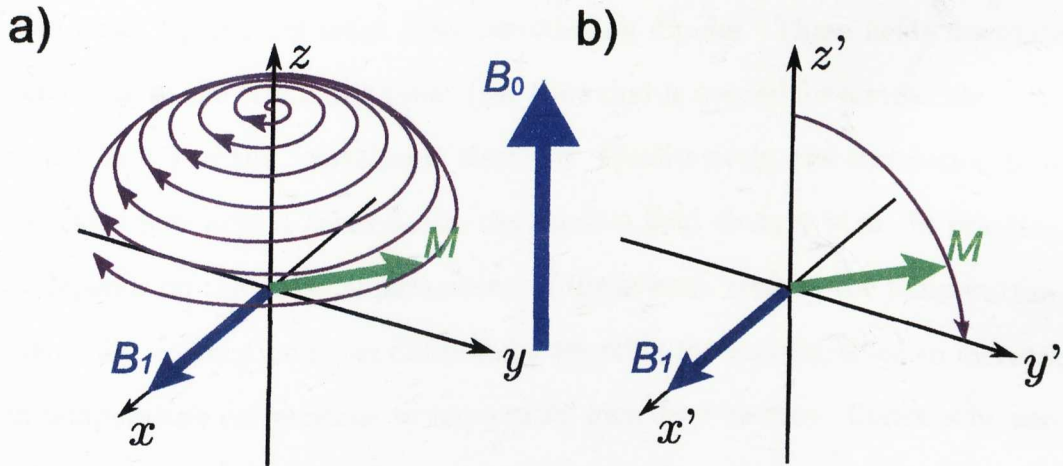


Figure 2.6: Comparison of the magnetisation's behaviour in two reference frames, laboratory (a), where the magnetisation vector \vec{M} spirals down around the direction of the external magnetic field \vec{B}_0 after applying a radio frequency magnetic pulse \vec{B}_1 , and rotating (b), where "frozen" magnetisation is flipped into the transverse (xy) plane by a 90° excitation pulse.

cated spiral motion of magnetisation during the application of an RF excitation pulse becomes a very simple and easily describable one-dimensional "flip" of the magnetisation.

The B_1 waveform that determines the RF pulse profile is never perfect, i.e. the ideal is a perfectly squared profile, but in reality this always results in side lobes caused by modulation of sin and cos (or exponential) wave functions.

2.2.3 Relaxation

Relaxation is the process of returning to equilibrium after a disturbance of the system. In the case of spins, the disturbance is caused by an RF pulse. The relaxation mechanism varies depending on the matter in which it occurs. For the purpose of this thesis, we are only interested in spins in liquid phase, where dipole-dipole interactions dominate. We then have to consider that each spin is not only under the influence of the external magnetic field \vec{B}_0 but

also local, fluctuating fields from surrounding dipoles. These fields fluctuate according to the “tumbling time” (the time that is needed for a molecule to re-orient by 1°) or the “correlation time”, τ_c . Qualitatively, the correlation time indicates how long it takes before the random field changes sign. In practice, τ_c depends on the physical parameters of the system, such as the temperature. Generally, correlation times decrease by warming the sample, since an increase in temperature corresponds to more rapid molecular motion. Conversely, correlation times are increased by cooling the sample.

These fluctuated fields are small, however, they still affect the relaxation processes by inducing transitions for field fluctuating at ω_L .

2.2.3.1 Longitudinal T_1 Relaxation

Relaxation in the z -axis (the axis of \vec{B}_0) is called longitudinal, spin-lattice, or simply T_1 relaxation. T_1 relaxation describes the mechanism of the spins returning to their equilibrium position aligned along the external magnetic field. For the spins to return to their thermal equilibrium, the behaviour of the z -component of the magnetisation is described by the Bloch equation (described in detail in Section 2.3):

$$\frac{dM_z}{dt} = \frac{M_0 - M_z}{T_1}, \quad (2.20)$$

where M_0 is the longitudinal magnetisation at equilibrium and T_1 is the longitudinal relaxation time. T_1 is specific for different kinds of matter and is dependent on the magnetic field strength (B_0) - the higher the magnetic field, the longer the T_1 for the same matter. The spin-lattice relaxation results from fluctuations of the dipole-dipole magnetic fields at the Larmor frequency. In addition to the magnetic field B_0 , relaxation time T_1 also depends on the correlation time τ_c , which is inversely proportional to temperature. Figure 2.7

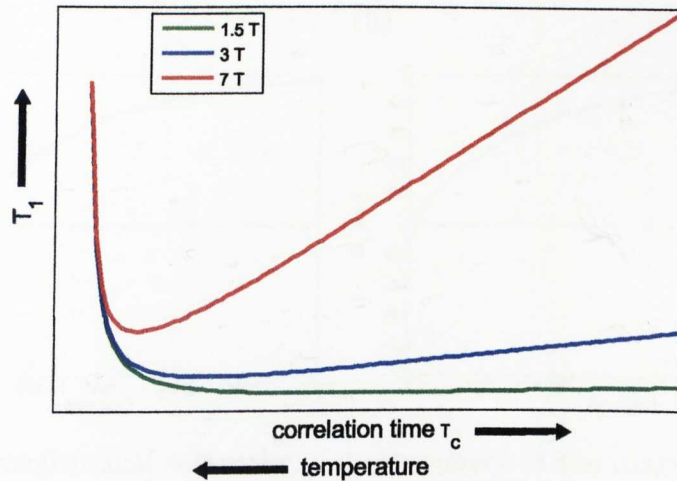


Figure 2.7: Schematic representation of dependencies between the longitudinal relaxation time T_1 , correlation time τ_c and temperature for 1.5 (green), 3 (blue), and 7 T (red).

shows schematically the dependence of the longitudinal relaxation time on correlation time and temperature for three external magnetic field strengths (1.5, 3 and 7 T).

The solution of Bloch equation shows that when a 180° inversion pulse is applied, the magnetisation is inverted, $M_z(0) = -M_0$, and the recovery then follows an exponential curve (Fig. 2.8(a)) according to:

$$M_z(t) = M_0 \left(1 - 2e^{-\frac{t}{T_1}} \right). \quad (2.21)$$

Following a 90° readout pulse, the longitudinal component of the magnetisation is $M_z(0) = 0$, and the recovery curve (Fig. 2.8(b)) is expressed by the saturation recovery curve:

$$M_z(t) = M_0 \left(1 - e^{-\frac{t}{T_1}} \right). \quad (2.22)$$

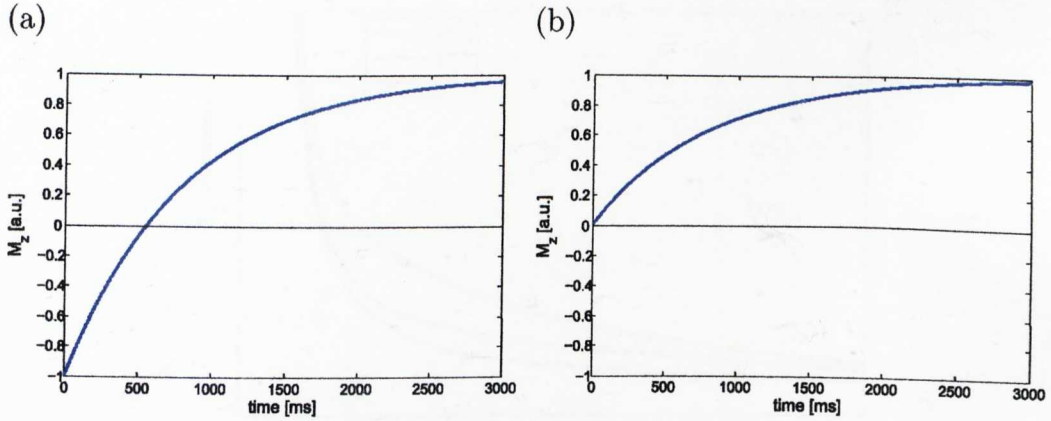


Figure 2.8: Longitudinal relaxation – z-component of the magnetisation (relative to M_0) as a function of time for inversion recovery (a) and saturation recovery (b). T_1 in this example is 800 ms.

2.2.3.2 Transverse T_2 Relaxation

Relaxation that is the result of short-range spin-spin interactions is called transverse or T_2 relaxation. T_2 relaxation describes the decay of transverse magnetisation and can also result from dipole-dipole interactions. Similarly, T_2 relaxation depends on the magnetic field, B_0 , correlation time, τ_c , and temperature. However temperature and correlation time are mutually dependent values. Figure 2.9 illustrates again the dependency of the transverse relaxation time on B_0 , τ_c , and temperature.

The transverse component of the Bloch equation, describing the behaviour of magnetisation in the transverse plane (xy) is:

$$\frac{dM_{xy}}{dt} = -\frac{M_{xy}}{T_2}, \quad (2.23)$$

where T_2 is the transverse relaxation time ($M_{xy} = 0$ at thermal equilibrium). Because of the nature of these interactions, the T_2 value is always smaller than T_1 and is dependent on the B_0 field strength. There is a tendency for the T_2 decay time to be longer when the spins are more mobile (such as in water) and to be shorter when the spins are more rigid (molecules containing

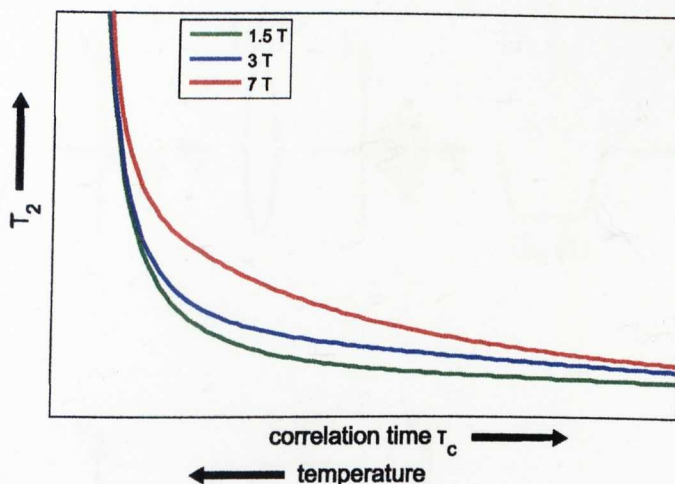


Figure 2.9: Schematic representation of dependencies between the longitudinal relaxation time T_2 , correlation time τ_c and temperature for 1.5 (green), 3 (blue), and 7 T (red).

rigid structures). A 90° pulse is required to incur full M_{xy} polarisation, and the solution of Bloch equation results in the exponential signal decay:

$$M_{xy}(t) = M_0 e^{-\frac{t}{T_2}}. \quad (2.24)$$

This signal decay after an excitation pulse is known as a Free Induction Decay (FID). It plays a key role in creation of “echoes”, where under the envelope of the FID multiple echoes can be formed within a single FID (see Section 3.5).

2.2.3.3 Transverse T_2^* Relaxation

The transverse magnetisation is also sensitive to B_0 field inhomogeneities. This additional contribution to the FID of transverse magnetisation is called T_2' and can be reversed with a 180° pulse. Figure 2.10 shows the spins' behaviour when using a spin echo sequence (a) and gradient echo (b). When a refocusing pulse (180°) is applied, not only does it reverse the changes to spins induced by the gradient, but also those variations in frequency modulations induced by B_0 field inhomogeneities.

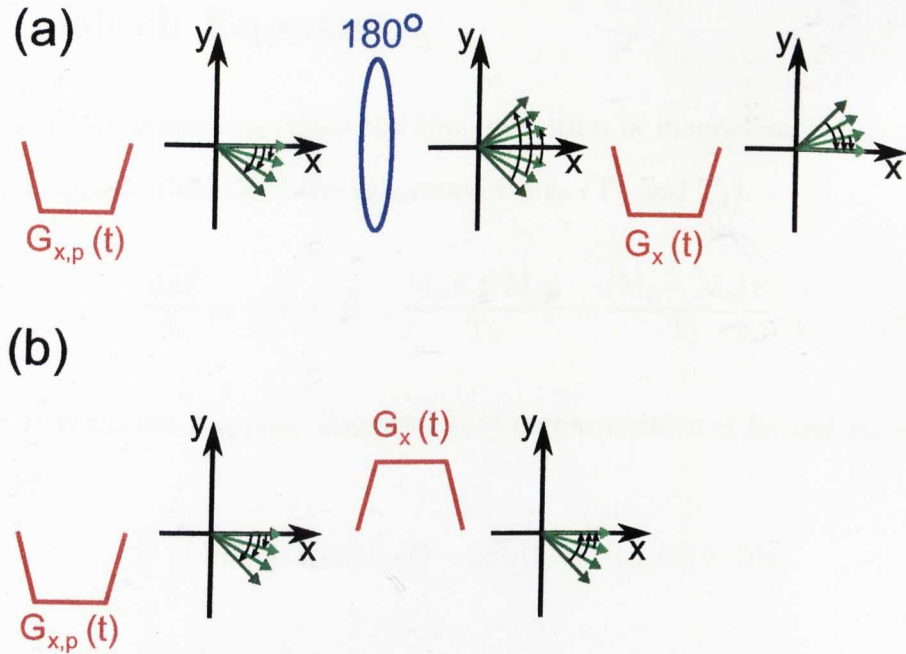


Figure 2.10: Schematic diagram of the spins' behaviour under the influence of a spin-echo (a) and gradient-echo (b) sequence. Different shades of green represent "fast" (dark green) and "slow" (bright green) spins.

The T_2^* relaxation time combines these elements:

$$\frac{1}{T_2^*} = \frac{1}{T_2} + \frac{1}{T_2'} \quad (2.25)$$

This relation indicates that $T_2^* \leq T_2$ and as B_0 increases, the inhomogeneities are greater and T_2^* shortens.

As described above, T_2' is reversible, and this can be achieved by employing spin-echo based sequences with refocusing pulses (Spin Echo – Echo Planar Image sequence, SE-EPI, is described later in Section 3.5).

2.3 Bloch Equations

The Bloch equations relate the time evolution of magnetisation to the external magnetic fields and the relaxation times (T_1 and T_2).

$$\frac{d\vec{M}}{dt} = \gamma\vec{M} \times \vec{B} - \frac{M_x\hat{x} + M_y\hat{y}}{T_2} + \frac{(M_0 - M_z)\hat{z}}{T_1}, \quad (2.26)$$

where \vec{B} is the total applied magnetic field (superposition of B_0 and B_1 effects) Eq. 2.27.

$$\vec{B} = \hat{x}B_1(t) \cos(\omega_{\text{RF}}t) - \hat{y}B_1(t) \sin(\omega_{\text{RF}}t) + \hat{z}B_0 \quad (2.27)$$

2.3.1 Bloch Equation without Relaxation

Using the basic relation (Eq. 2.14 and 2.15) and the conversion of the \vec{B} vector (Eq. 2.27) neglecting relaxation and diffusion processes according to the Eq. 2.13, the Bloch equation in the rotating reference frame is:

$$\left(\frac{d\vec{M}(t)}{dt} \right)_{\text{rot}} = \gamma\vec{M} \times \vec{B}_{\text{eff}} \quad (2.28)$$

$$\vec{B}_{\text{eff}} = \left[B_1(t) [\hat{x} \cos((\omega_{\text{RF}} - \omega)t) - \hat{y} \sin((\omega_{\text{RF}} - \omega)t)] + \hat{z} \left(B_0 - \frac{\omega}{\gamma} \right) \right] \quad (2.29)$$

A special case of this equation is when $\omega_{\text{RF}} = \omega = \omega_L$, in which the magnetisation precesses about the applied B_1 field and the effective field reduces to $\vec{B}_{\text{eff}} = \hat{x}B_1(t)$.

After explicitly carrying out the vector cross product, Equations 2.28 and 2.29 can be expressed as three scalar equations:

$$\left(\frac{dM_x}{dt}\right)_{\text{rot}} = \gamma M_y \left(B_0 - \frac{\omega}{\gamma}\right) + \gamma M_z B_1(t) \sin((\omega_{\text{RF}} - \omega)t), \quad (2.30)$$

$$\left(\frac{dM_y}{dt}\right)_{\text{rot}} = -\gamma M_x \left(B_0 - \frac{\omega}{\gamma}\right) + \gamma M_z B_1(t) \cos((\omega_{\text{RF}} - \omega)t), \quad (2.31)$$

$$\left(\frac{dM_z}{dt}\right)_{\text{rot}} = -\gamma M_x B_1(t) \sin((\omega_{\text{RF}} - \omega)t) - \gamma M_y B_1(t) \cos((\omega_{\text{RF}} - \omega)t). \quad (2.32)$$

If we define our magnetisation in a transverse plane as a complex number:

$$M_c = M_x + iM_y, \quad (2.33)$$

and write M_c explicitly based on equations (2.30) and (2.31) we have:

$$\begin{aligned} \left(\frac{dM_c}{dt}\right)_{\text{rot}} &= -i\gamma \left(B_0 - \frac{\omega}{\gamma}\right) (M_x + iM_y) \\ &\quad + i\gamma M_z B_0(t) [\cos((\omega_{\text{RF}} - \omega)t) - i \sin((\omega_{\text{RF}} - \omega)t)] \\ &= -i\gamma M_c \left(B_0 - \frac{\omega}{\gamma}\right) + i\gamma M_z B_0(t) e^{-i(\omega_{\text{RF}} - \omega)t} \end{aligned} \quad (2.34)$$

2.3.2 Bloch Equation with T_1 and T_2 Relaxation

The consideration of longitudinal and transverse relaxations to the Bloch equation is fundamental for all NMR processes, therefore relaxation components must be included:

$$\left(\frac{d\vec{M}}{dt}\right)_{\text{rot}} = \gamma \vec{M} \times \vec{B}_{\text{eff}} - M_T. \quad (2.35)$$

To accomplish the true equation, we need to convert the relaxation components into the rotating reference frame using equation (2.13):

$$\begin{aligned}
 \begin{bmatrix} M_{Tx'} \\ M_{Ty'} \\ M_{Tz'} \end{bmatrix} &= \begin{bmatrix} \cos(\omega t) & -\sin(\omega t) & 0 \\ \sin(\omega t) & \cos(\omega t) & 0 \\ 0 & 0 & 1 \end{bmatrix} \begin{bmatrix} \frac{M_x}{T_2} \\ \frac{M_y}{T_2} \\ \frac{M_0 - M_z}{T_1} \end{bmatrix} \\
 &= \begin{bmatrix} -\frac{M_x \cos(\omega t) - M_y \sin(\omega t)}{T_2} \\ -\frac{M_x \sin(\omega t) + M_y \cos(\omega t)}{T_2} \\ \frac{M_0 - M_z}{T_1} \end{bmatrix}. \tag{2.36}
 \end{aligned}$$

Therefore, our explicit expressions (Eqs. 2.30-2.32) for individual components of the magnetisation in the rotating reference frame, and including the T_1 and T_2 relaxations, are as follows:

$$\begin{aligned}
 \left(\frac{dM_x}{dt} \right)_{\text{rot}} &= \gamma \left[M_y \left(B_0 - \frac{\omega}{\gamma} \right) + M_z B_1(t) \sin((\omega_{\text{RF}} - \omega)t) \right] \\
 &\quad - \frac{M_x \cos(\omega t) - M_y \sin(\omega t)}{T_2}, \tag{2.37}
 \end{aligned}$$

$$\begin{aligned}
 \left(\frac{dM_y}{dt} \right)_{\text{rot}} &= -\gamma \left[M_x \left(B_0 - \frac{\omega}{\gamma} \right) - M_z B_1(t) \cos((\omega_{\text{RF}} - \omega)t) \right] \\
 &\quad - \frac{M_x \sin(\omega t) + M_y \cos(\omega t)}{T_2}, \tag{2.38}
 \end{aligned}$$

$$\begin{aligned}
 \left(\frac{dM_z}{dt} \right)_{\text{rot}} &= -\gamma [M_x B_1(t) \sin((\omega_{\text{RF}} - \omega)t) + M_y B_1(t) \cos((\omega_{\text{RF}} - \omega)t)] \\
 &\quad + \frac{M_0 - M_z}{T_1}. \tag{2.39}
 \end{aligned}$$

Chapter 3

Magnetic Resonance Imaging and Instrumentation

Magnetic Resonance Imaging (MRI) is an imaging technique entirely based on the NMR phenomenon. MRI was simultaneously discovered by two independent groups led by Peter Mansfield [7] and Paul Lauterbur [8] in 1973. The first *in vivo* images were produced in 1977 [9] and following the development of this new and exciting method avalanched with its most practical application in diagnostic medicine.

3.1 Fourier Transform

One of the most important tools in NMR, together with implementation of the rotating reference frame (Section 2.2.1), is the Fourier transform (FT). The FT was named after the French mathematician Jean Baptiste Joseph Fourier (1768 – 1830) and it is a mathematical operation that yields the spectral content of a signal [10]. If $g(x)$ is a function of the real variable “ x ”, the output of the Fourier transform, $G(k)$, of that function can be calculated

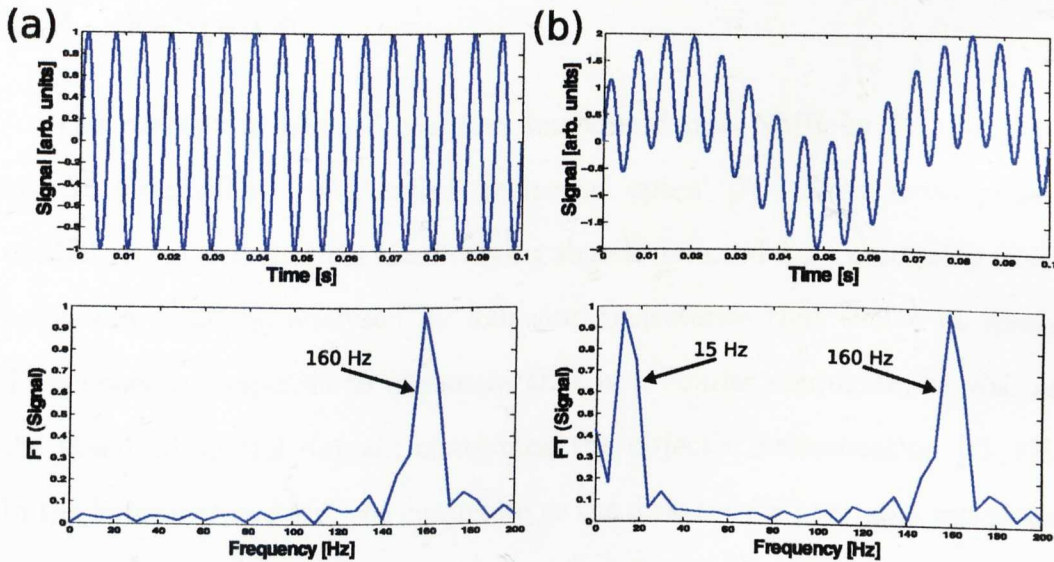


Figure 3.1: Schematic representations of the Fourier transform using the step function in Matlab. (a) time domain containing only one frequency (a) and its Fourier transform showing only one peak at that frequency (≈ 160 Hz); (b) time response of the signal containing superposition of two different frequencies with the same amplitude and its Fourier transform revealing two peaks at those frequencies (≈ 15 and ≈ 160 Hz).

using the following equation:

$$\text{FT}[g(x)] = G(k) = \int_{-\infty}^{\infty} g(x)e^{-2\pi i k x} dx, \quad (3.1)$$

where “x” and “k” are two real variables called Fourier conjugates and represent a pair of conjugate domains, such as time and frequency or distance and spatial frequency.

Figure 3.1 shows two examples of decoding the signal in the time domain using FT to reveal the frequency information of the function’s representation. This shows functions composing one frequency (Fig. 3.1(a)) and two frequencies (Fig. 3.1(b)). These examples are only to visualise the mechanism of the Fourier transform; real time-domain signals are far more complex and so are the corresponding frequency-domain spectra.

3.2 k-Space

The concept of k-space was first introduced into NMR by P. Mansfield and P. Grannell in 1973, called 'reciprocal space' [7]. Early development of MRI recognised that the time-varying signals detected from precessing magnetisation could be analysed by following trajectories that evolve in space. That space corresponds to a domain that is a Fourier conjugate, as well as the standard spatial domain containing the object's magnetisation [11, 12]. In the Fourier transform, the conjugate to the distance (\vec{r}) variable was given a letter "k" and the domain was then called "k-space". This concept brings simplicity to the understanding of many pulse sequences. Figure 3.2 shows the k-space representation of an image.

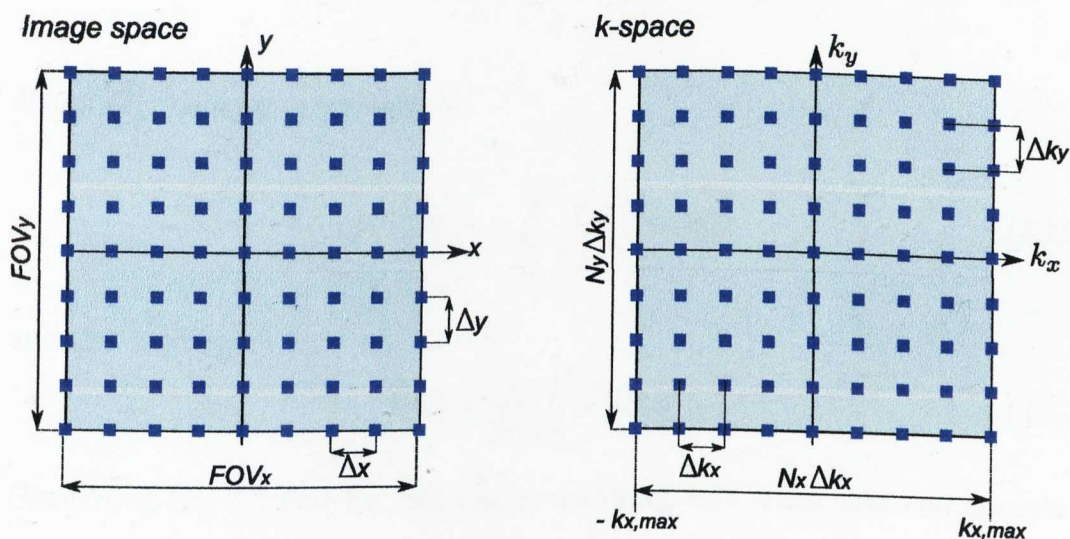


Figure 3.2: The relationship between image space (left) and k-space (right).

The introduction of k-space helped visualise the trajectories of spins' phase in the presence of field gradients. An example of a trajectory typically used in most Echo Planar Imaging sequences (see Section 3.5), is shown in Figure 3.3. k-space represents the spatial frequency distribution of an MR image where the accumulated phase, under the influence of time-dependent field gra-

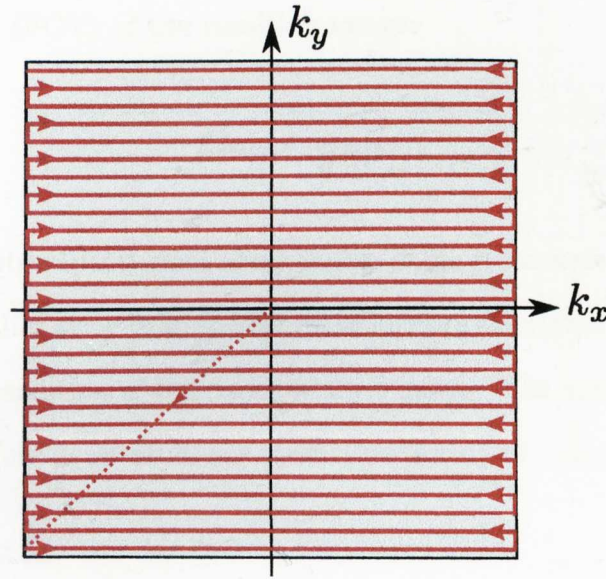


Figure 3.3: Example of a k-space acquisition trajectory commonly used in Echo Planar Imaging sequences. The dotted line indicates a prephasing trajectory and arrows indicate direction of k-space traversal.

dients $\vec{G}(\tau)$, can be expressed as:

$$\phi(\vec{r}, t) = \gamma \int_0^t \vec{r} \cdot \vec{G}(\tau) d\tau, \quad (3.2)$$

and the \vec{k} vector:

$$\vec{k}(t) = \frac{\gamma}{2\pi} \int_0^t \vec{G}(\tau) d\tau, \quad (3.3)$$

Combining Eq. 3.2 and Eq. 3.3 and considering only transverse components of magnetisation, $M_{\perp}(\vec{r})$, and B_1 field - $B_{\perp}(\vec{r})$, the time-domain signal created is:

$$S(t) = \int M_{\perp}(\vec{r}) B_{\perp}(\vec{r}) e^{-i2\pi \vec{k}(t) \cdot \vec{r}} d^3r. \quad (3.4)$$

The trajectories of the k-vector traverse a continuous path (Fig. 3.3), however the signal is sampled only at discrete intervals (Δk_x) along the path (Fig. 3.2). The spacing of the measurements made in k-space determines

the field of view (FOV) of the resulting image:

$$\Delta k_{x,y} = \frac{1}{\text{FOV}_{x,y}}, \quad (3.5)$$

where x and y subscripts denote components of the transverse plane. With this in mind, the further away from the centre of k-space the signal is being sampled, the higher the resolution of the reconstructed image. The maximum amplitude of k-space therefore determines the spatial resolution of a reconstructed image.

3.3 Imaging Gradients

To produce an MRI image, the signal has to carry spatial information, which is made possible by employing imaging gradients (Fig. 3.4) applied in all directions (x, y and z). Gradients cause spatial variation with the following mathematical representation:

$$G_x = \frac{\partial B_z}{\partial x}, G_y = \frac{\partial B_z}{\partial y}, G_z = \frac{\partial B_z}{\partial z}. \quad (3.6)$$

Commonly used is a Cartesian planar scheme, under which there are conventionally entitled frequency-encoding gradients (x-axis), phase-encoding (y-axis), and slice selection gradients (z-axis).

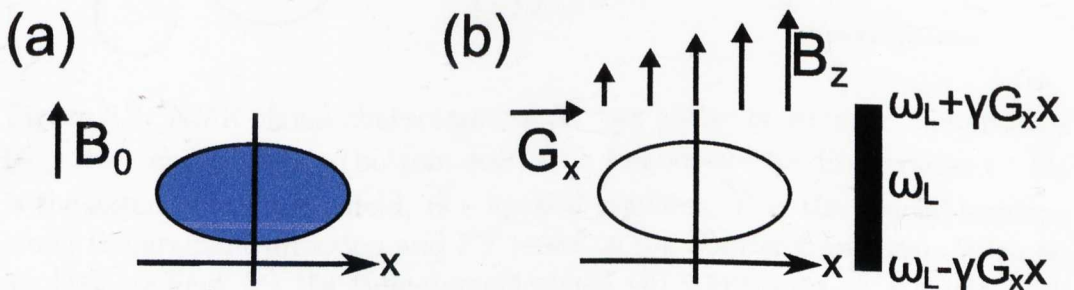


Figure 3.4: Schematic image of a gradient application; object in the external magnetic field \vec{B}_0 (a), Larmor frequency modulations after application of the \vec{G} gradient in a given direction.

3.3.1 Frequency-Encoding Gradient

A frequency-encoding gradient spatially encodes NMR signal by assigning a unique precession frequency to each spin cluster (if the cluster contains spins precessing with the same frequency, it is called an isochromat). Figure 3.5 illustrates the difference in outgoing signal before and after applying a frequency-encoding gradient. It shows an example of two objects containing water. The first is placed in a uniform magnetic field \vec{B}_0 (Fig. 3.5(a)), producing a single-frequency NMR signal (Fig. 3.5(b)); the second is placed in the same magnetic field, but with an applied gradient along the horizontal direction $\vec{G} \cdot \vec{r}$ (Fig. 3.5(d)), producing a complex signal in the time domain (Fig. 3.5(e)). After applying a Fourier transform, the first case reveals

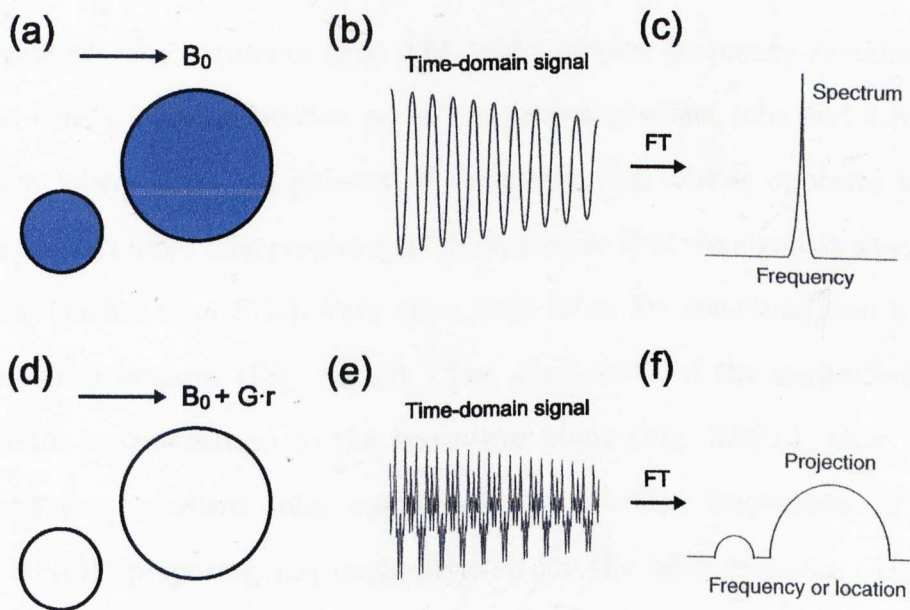


Figure 3.5: NMR signal characteristics for two plates of water in the absence (top row) and presence (bottom row) of a frequency-encoding gradient. \vec{B}_0 is the external magnetic field, \vec{G} - applied gradient, \vec{r} is the spacial location along the gradient direction and FT refers to the Fourier transform. With no applied gradient (a) the time-domain signal (b) transforms to a single peak frequency-domain spectrum (c). Applied gradient modulates the frequencies of spin isochromats (d) causing changes in time-domain signal (e), which transforms to a projection in a frequency-domain (f).

a single peak spectrum (frequency domain) without any spatial information (Fig. 3.5(c)). However, when a Fourier transform is applied to the second time-domain signal, the spectrum is a projection of the two objects in the direction of gradient (Fig. 3.5(f)). Therefore, spatial information is encoded into the NMR signal by the frequency-encoding gradient, and can be decoded by the Fourier transform.

Frequency encoding is commonly used in spin-echo and gradient-echo sequences such as EPI (Echo Planar Imaging), RARE (Rapid Acquisition with Refocused Echoes) and GRASE (GRAdient And Spin Echo). Their mechanisms are slightly different as well as their basic applications.

3.3.1.1 Gradient Echo

Gradient echo sequences (Fig. 3.6), which employ frequency-encoding gradients, consist of an excitation pulse, prephasing gradient lobe and a readout gradient lobe. Note, the polarity of the prephasing lobe is opposite to that of the readout lobe. The prephasing lobe is used so that the signal is a symmetric echo (rather than FID). Very often both lobes are combined into a single continuous waveform (Fig. 3.6(a)). The application of the excitation pulse brings the magnetisation to the transverse plane (Fig. 3.6(b)), after which, a prephasing gradient lobe modulates the resonant frequencies of spins (Fig. 3.6(c)), preparing the magnetisation for the echo creation. Different spins are at different frequencies – spin dephasing (Fig. 3.6(c)). The opposite polarisation of the readout gradient lobe modulates the spins frequencies in the opposite direction causing the spins in isochromats to rephase and to produce an echo in the middle of the readout lobe (Fig. 3.6(d)). In multi-echo sequences, the second half of the readout lobe is also used as a prephasing lobe for the following echo. The absence of the 180° refocusing pulse results in no compensation for off-resonance effects (chemical shift, B_0 inho-

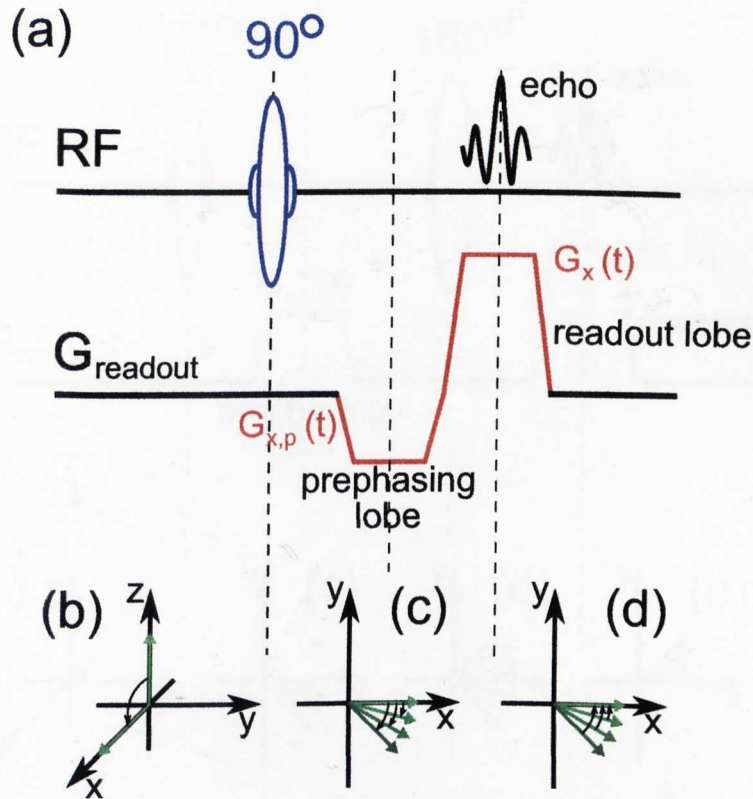


Figure 3.6: Schematic of a simple gradient-echo sequence employing a frequency encoding gradient (a) and diagrams of magnetisation behaviour with the phase accumulation during: excitation pulse (b), prephasing lobe (c) and readout lobe (d).

mogeneities or susceptibility variations), therefore, this method provides a T_2^* contrast mechanism.

3.3.1.2 Spin Echo

A frequency-encoding gradient waveform typically consist of two parts, a 'prephasing gradient' lobe (dephasing gradient lobe) and a 'readout gradient' lobe. Figure 3.7(a) shows a schematic example of the gradient configuration in the case of spin-echo sequences. Firstly, an excitation (90°) RF pulse is applied to bring the magnetisation to the transverse plane (Fig. 3.7(b)). A prephasing gradient lobe is then applied in order to dephase spins, therefore, spins of different isochromats precess with a different, modulated angular

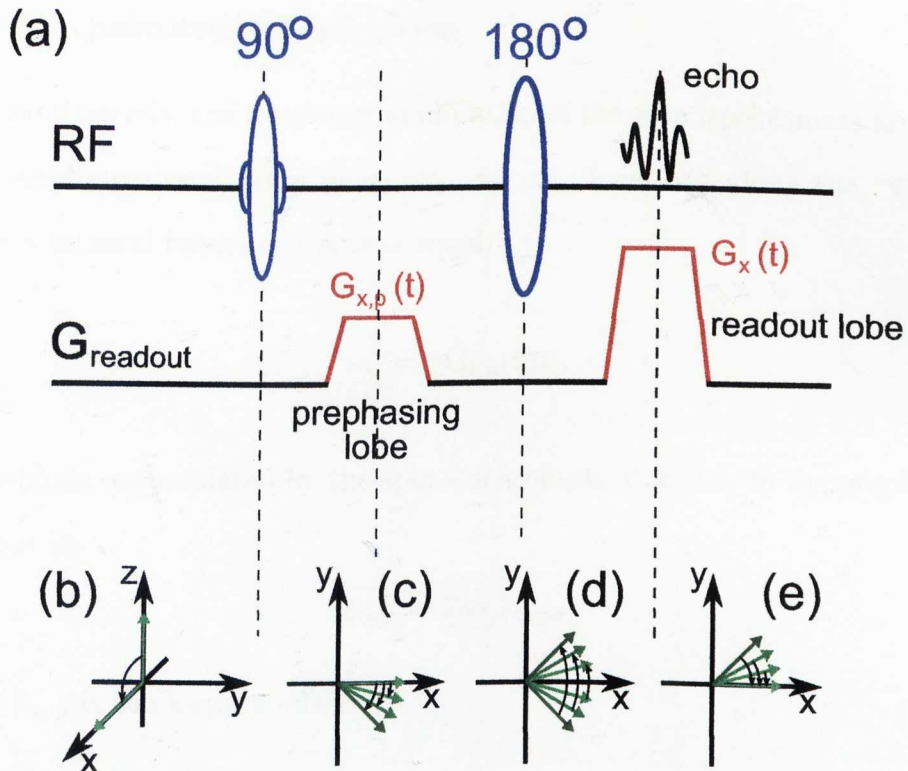


Figure 3.7: Schematic of a simple spin-echo sequence employing a frequency encoding gradient (a) and diagrams of magnetisation behaviour during: excitation pulse (b), prephasing lobe (c), refocusing RF pulse (d) and readout lobe (e).

velocity (Fig. 3.7(c)). Next, a 180° RF pulse is applied to flip the spins about the x-axis (an axis of the applied gradient) (Fig. 3.7(d)). Because the spins were flipped (the 180° pulse reverses the phase so that “fast” spins are now behind the “slow” spins) the readout lobe (of the same polarisation as the prephasing lobe) will modulate their precession frequencies back to return them to their original positions (Fig. 3.7(e)). The echo is formed in the middle of the readout lobe duration as the area under the gradient shape is twice as big as the one of the prephasing lobe. In multiecho sequences, the second part of the readout lobe is used as a prephasing lobe for the next echo. The refocusing (180°) RF pulse also refocuses phase accumulation from off-resonance effects, therefore this method is used when T_2 contrast is required.

3.3.1.3 Quantitative Description

Quantitatively, the frequency modulation of the spin isochromats arranged in a one-dimensional array at $x_1, x_2, x_3, \dots, x_n$ locations along the “x” axis in the rotational reference frame is equal:

$$\omega_{x_j} = \gamma G_{x,p}(t)x_j, \quad (3.7)$$

so the phase accumulated by the spin isochromats at x_j due to the prephasing gradient is:

$$\phi_{x_j,p} = 2\pi x_j k_{x_j,p}, \quad (3.8)$$

where $k_{x_j,p}$ is the k-space offset:

$$k_{x_j,p} \equiv \frac{\gamma}{2\pi} \int_0^T G_{x_j,p}(t) dt. \quad (3.9)$$

The NMR signal in the transverse plane can be obtained by summing up all the isochromat vectors weighted by their spin densities in various locations ($\rho_{x_1}, \rho_{x_2}, \rho_{x_3}, \dots, \rho_{x_n}$):

$$S_{x,p} = \sum_{j=1}^n \rho_{x_j} e^{-i\phi_{x_j,p}} \approx \int_{-\infty}^{+\infty} \rho(x) e^{-i\phi_p(x)} dx, \quad (3.10)$$

where $\rho(x)$ and $\phi_p(x)$ are the continuous representations of the spin density and the phase dispersion, respectively. In a spin-echo sequence, the 180° refocusing RF pulse, inverts the $\phi_p(x)$ phase dispersion, so the signal after that becomes:

$$S_{x,p}^{se} = \int_{-\infty}^{+\infty} \rho(x) e^{i\phi_p(x)} dx. \quad (3.11)$$

At the beginning of the readout lobe $G_x(t)$, another time-dependent mod-

ulation is introduced:

$$\phi(x,t) = 2\pi x k_x(t), \quad (3.12)$$

with the k-space offset:

$$k_x(t) \equiv \frac{\gamma}{2\pi} \int_0^t G_x(t) dt. \quad (3.13)$$

Here the time origin is defined as the beginning of the readout gradient lobe.

With the new phase previously introduced the time dependent signal (Eq. 3.10)

is now equal to:

$$S(t) = \int_{-\infty}^{+\infty} \rho(x) e^{-i(\phi(x,t) - \phi_p(x))} dx. \quad (3.14)$$

3.3.2 Phase-Encoding Gradient

Spatial localisation of the MRI signal normally employs both phase and frequency encoding. As one can intuitively predict, a phase-encoding gradient modulates the phase of the precession of the magnetisation instead of manipulating its frequency (as described in Section 3.3.1). The idea behind phase encoding is to create a linear spatial variation of the phase of the magnetisation orthogonal to readout gradients (frequency encoding). Figure 3.8 shows the behaviour of the transverse magnetisation of an object after introducing a phase-encoding gradient in one direction. In a pulse sequence, the phase-encoding gradient must be implemented before the readout but after the excitation pulse, such that magnetisation is in the transverse plane (Fig. 3.9). The phase modulation can be adjusted by changing the area under the phase-encoding lobe, and the signal can be reconstructed with FT to recover spatial information about the object. Phase encoding is used with k-space sampling (Section 3.2) and, as mentioned before, usually used in the direction orthogonal to the frequency-encoding gradient. Both gradients can be played concurrently.

The implementation of the phase-encoding gradient is the same for the spin-

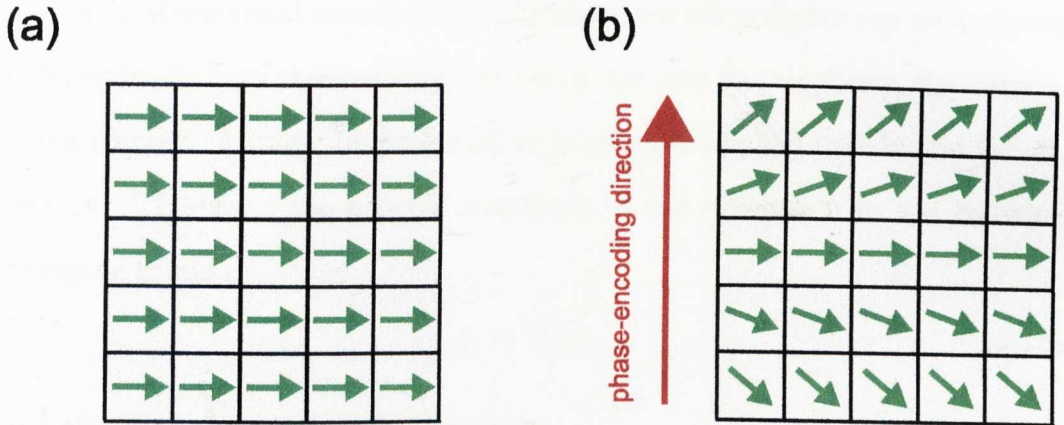


Figure 3.8: Transverse magnetisation of the object (divided into 25 pixels) commencing the excitation pulse before (a) and after (b) employing a phase-encoding gradient. Phase of the lines of the magnetisations are modulated according to the applied gradient.

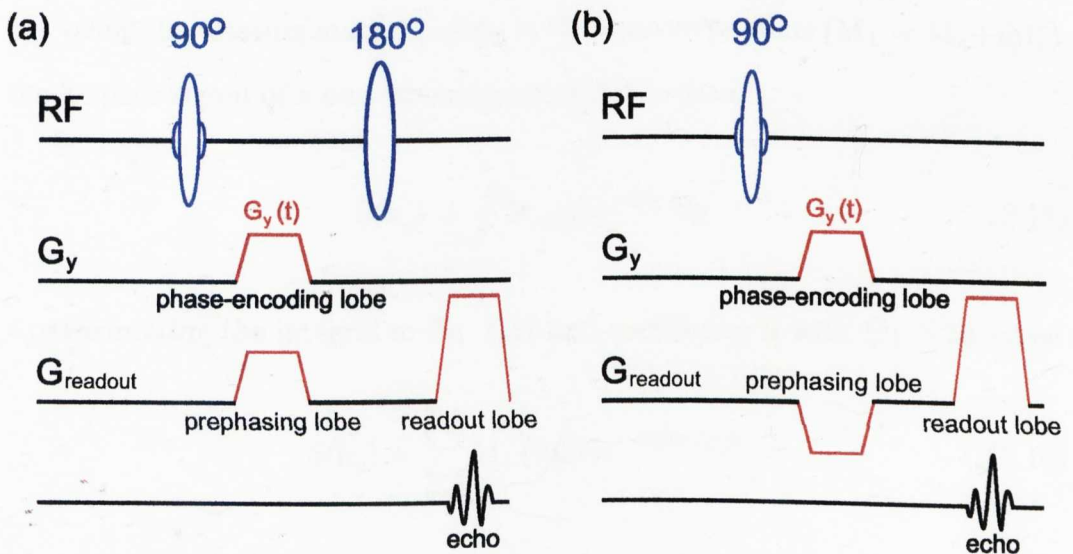


Figure 3.9: Schematic of a simple spin-echo (a) and gradient-echo (b) sequence employing a phase-encoding lobe. Readout gradient configuration is also shown for both sequences, played concurrently to the phase-encoding lobes. For the spin-echo pulse sequence, the gradient can occur either before or after the 180° refocusing pulse.

echo (Fig. 3.9(a)) and gradient-echo (Fig. 3.9(b)) sequences.

The mathematical description of the phase-encoding signal can be analysed independently from the frequency-encoding one, and for simplicity, the latter is being ignored. A linear phase-encoding gradient is applied here in the “y” direction. Therefore, the angular frequency of the precession in the rotating reference frame is:

$$\omega = \gamma G_y y, \quad (3.15)$$

and the phase at the end of the lobe is:

$$\phi(y) = 2\pi k_y y, \quad (3.16)$$

where k_y is k-space location defined in Section 3.2. The signal detected is the vector sum of the magnetisation of all the nuclear spins in the object (Section 2.2 and 2.3). Using complex notation to describe the rotation with M_{\perp} being the rotating magnetisation in the transverse plane ($M_{\perp} = M_x + iM_y$), the k-space signal of a one-dimensional object is then:

$$S(k_y) = \int M_{\perp}(y) e^{-i\phi(y)} dy. \quad (3.17)$$

Approximating the integral in Eq. 3.17 and combining it with Eq. 3.16 gives:

$$S(k_y) = \sum_{n=0}^{N-1} M_{\perp}(n\Delta y) e^{-2\pi i(n\Delta y)k_y}, \quad (3.18)$$

where $y = n\Delta y$, and Δy and N are the pixel size and number of pixels, respectively.

The prephasing lobe (also called “dephasing lobe”) of a readout gradient can be played concurrently with the phase-encoding gradient lobe (Fig. 3.9). In case of the spin-echo sequence, the prephasing lobe and the readout lobe are

applied in the same direction (positive sign in Fig. 3.9(a)), whereas gradient-echo-based sequences employ the prephasing lobe with a reversed polarity compared to the readout gradient lobe.

3.3.3 Slice-Selection Gradient

Spatially selective RF pulses are used for many purposes in MRI, including excitation, inversion, refocusing or spatial presaturation of magnetisation. Each of these applications require a slice-selection gradient [13–15] to achieve the desired spatial localisation. The slice-selection gradient is normally a constant gradient that, in the pulse sequence, is applied simultaneously with the RF pulse (Fig. 3.10).

The radio frequency bandwidth represents a range of frequencies that are contained within the RF pulse. Figure 3.11 illustrates the selection of the RF

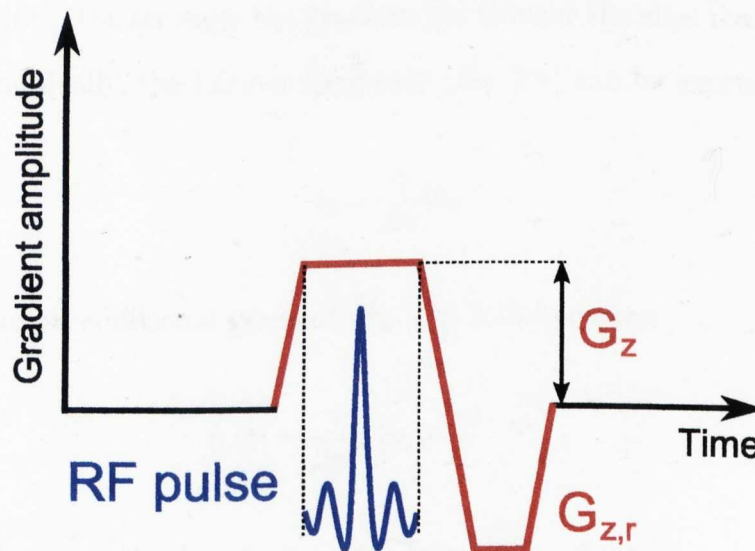


Figure 3.10: The slice-selection gradient (red) is a constant gradient (plateau) occurring simultaneously with a selective radio frequency pulse. The amplitude of the gradient, G_z , and RF pulse bandwidth determine the thickness of the slice. The slice selective excitation is followed by a negative gradient lobe ($G_{z,r}$), which has half the area of the positive lobe, to refocus the dephasing effects induced by the slice selection gradient.

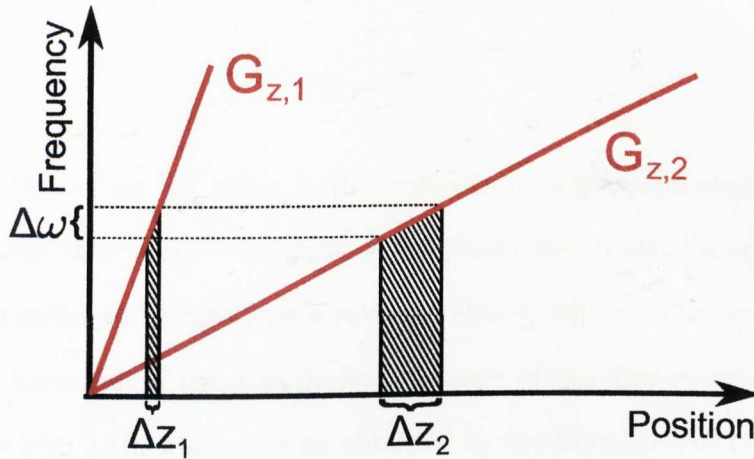


Figure 3.11: Larmor frequency as a function of position along the slice-selective gradient direction (z -axis) for two different strengths of the gradient (red lines, $G_{z,1}$ and $G_{z,2}$). For the same RF pulse bandwidth, $\Delta\omega$, the excited slice thickness (Δz_1 and Δz_2) decreases with gradient strength ($G_{z,1} > G_{z,2}$).

bandwidth ($\Delta\omega$), which then is translated by an appropriate slice-selective gradient ($G_{z,1}$, $G_{z,2}$) to a range of locations (Δz_1 , Δz_2) — a slice. For a fixed RF bandwidth, the stronger the gradient the thinner the slice that is selected.

Mathematically, the Larmor frequency (Eq. 2.5) can be expressed as:

$$f_L = \frac{\gamma}{2\pi} B_0. \quad (3.19)$$

By applying an additional gradient \vec{B}_0 , Eq. 3.19 becomes:

$$f_L(\mathbf{r}) = \frac{\gamma}{2\pi} \left(B_0 + \vec{G} \cdot \vec{r} \right), \quad (3.20)$$

where \vec{r} denotes a displacement vector from the gradient isocentre. In the rotating reference frame, the \vec{B}_0 term vanishes. Only a displacement in the direction of the slice-selection gradient affects the resonant frequency, therefore, considering the direction along the z -axis, \vec{G} and \vec{r} become G_z and Δz (slice thickness), respectively. The slice thickness can then be determined from

Eq. 3.20 as:

$$\Delta z = \frac{2\pi\Delta f}{\gamma G_z}. \quad (3.21)$$

Application of an RF pulse in the presence of a gradient results in a continuous phase shift across the slice. This phase shift must be corrected and this is accomplished by applying a reversed slice gradient. The correcting gradient must have half of the area under the curve of the slice selection gradient, as shown in Fig. 3.10, which can be obtained by modifications of both duration and amplitude.

3.4 Two-Dimensional Acquisition

Two-dimensional imaging, also known as planar imaging, involves: slice selection (Section 3.3.3) and spatial encoding within that slice (Section 3.3.1 and 3.3.2). Following the slice selection and sampling k-space along the trajectory during the decay of transverse magnetisation, a 2D image is produced by an inverse 2D Fourier transform.

To cover a required volume of an object with 2D acquisition, multiple slices must be acquired, where the spatial information is individually encoded into its own k-space data matrix for each slice. There are two main algorithms to obtain images of multiple slices: sequential and interleaved (Fig. 3.12).

In the first method (Fig. 3.12(a)), after obtaining the points of one k-space line, the sampling is moved to the next k-space line, this process is repeated until all the k-space lines (following the sampling trajectory) are acquired within one slice. Only after completing the acquisition of the entire slice, does this process move to the next slice. The entire image is completed, when all the predefined slices have been collected. In practice, this method is commonly used in sequences with the repetition time, TR, close to the actual length of the pulse sequence waveform, T_{seq} ($TR \simeq T_{\text{seq}}$).

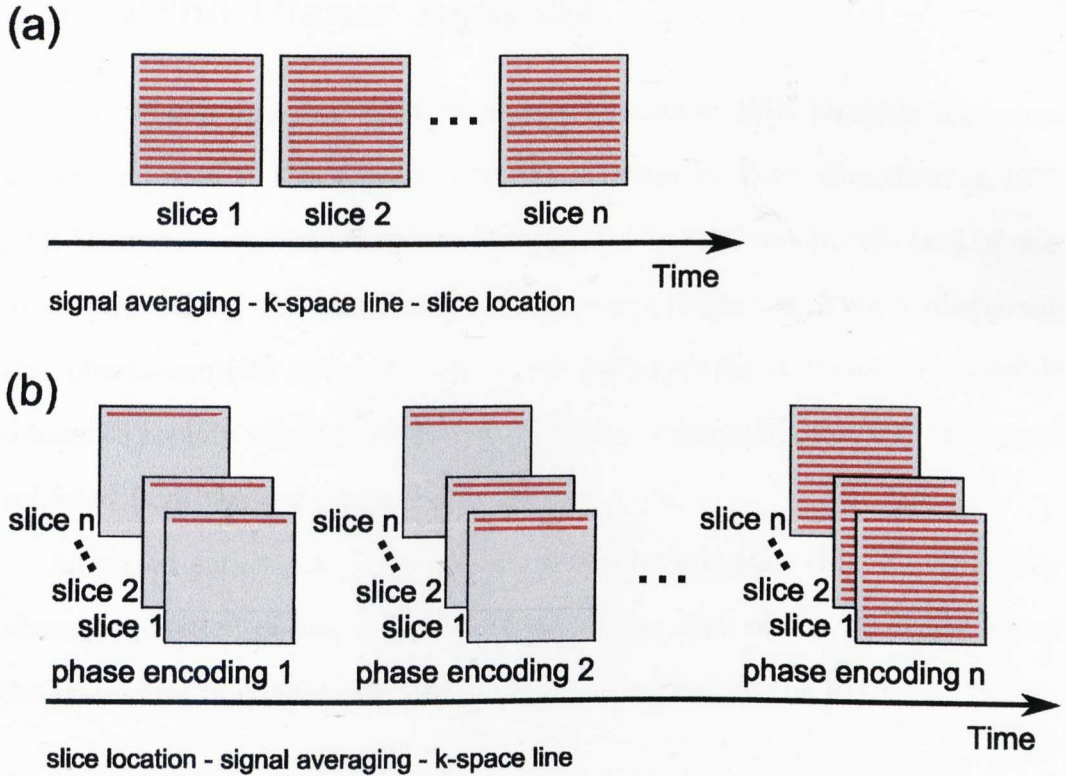


Figure 3.12: Sequential (a) and interleaved (b) acquisition in 2D imaging. Grey boxes represent slices and red lines represent lines of k-space. The looping order for each acquisition is presented.

In the interleaved method, (Fig. 3.12(b)), after selecting the first slice and obtaining the average signals of each interval point within the k-space line, the acquisition continues by collecting signals in the same line, but from the next slice. The sampling moves to the next k-space line when the first line of the k-space was acquired in all the predefined slices. The entire image is collected, when all the lines of k-space have been completed. This method is used in sequences with $TR \gg T_{seq}$, to achieve desired image contrast (i.e. T_1 weighing) and high signal-to-noise ratio.

3.5 Echo Planar Imaging

Echo Planar Imaging (EPI) is one of the fastest MRI imaging sequences known and used to this day since its development by Peter Mansfield in 1977 [16]. Using modern technology, a 2D image can be produced in only tens of milliseconds, making this sequence very attractive, especially from a diagnostic and pharmaceutical point of view. Such a fast sweep of k-space is possible thanks to rapidly varying additional gradients, maximising usage of the signal collected from the transverse magnetisation.

As stated earlier, the standard gradient-echo sequence (Fig. 3.13(b)) only allows acquisition of one k-space line within the time of the T_2^* decay, where the transverse magnetisation signal decays according to the FID:

$$M_{\perp}(t) = M_{\perp}(0)e^{-\frac{t}{T_2^*}} \quad (3.22)$$

EPI introduces a series of gradients, reversing the scattered spins by negating accumulated frequencies and phases (Fig. 3.13(c)). This configuration allows creation of multiple gradient echoes within one signal decay, without applying additional RF excitation. The number of usable signal echoes is determined by the T_2^* of the tissue, applied readout gradient (both the slew rate and the amplitude), time between echoes (echo spacing time - t_{esp}), receiver bandwidth, and the k-space matrix size.

In gradient-echo EPI (GE-EPI) (Fig. 3.14), an RF excitation pulse (normally 90° to maximise the signal in the transverse plane) is applied to create an FID. After the initial excitation, a prephasing gradient lobe is applied (as described in Section 3.3.2) to prepare for the signal acquisition, which determines the beginning of k-space. The readout gradient (frequency-encoding) creates echoes, whilst the phase-encoding gradient changes the acquisition lines of k-space (blips in Fig. 3.14) according to the trajectory. The blips of

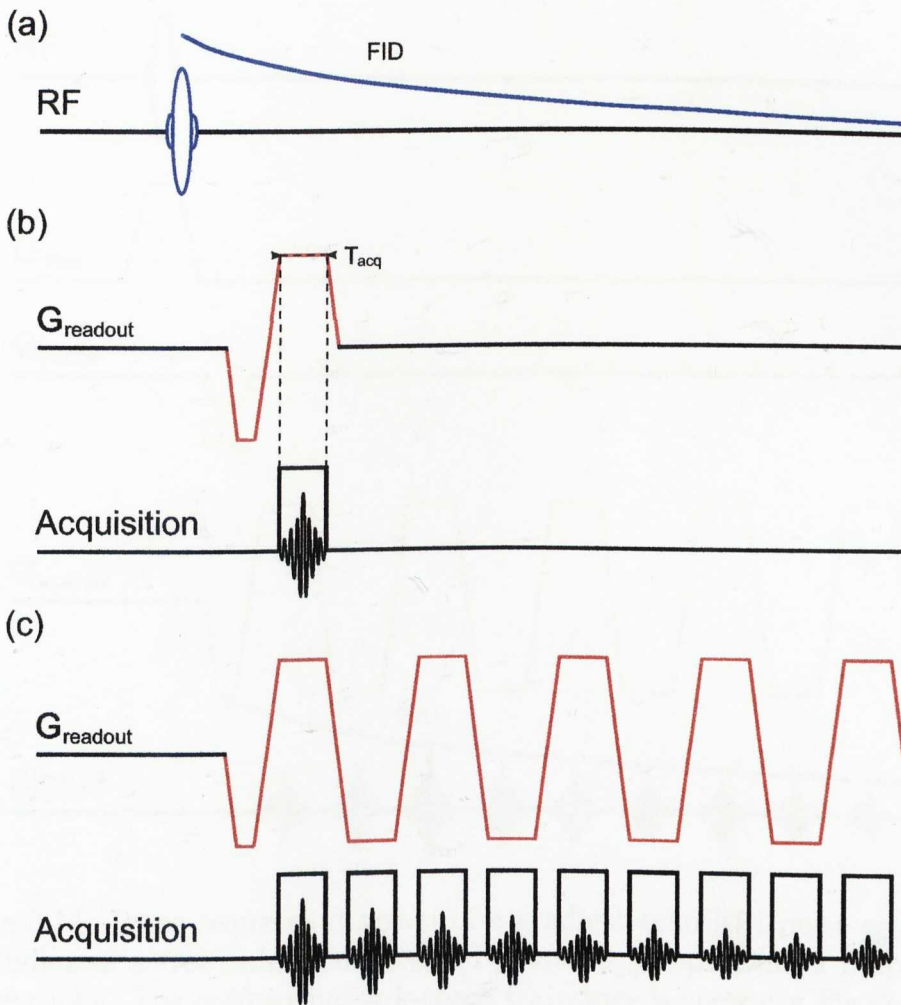


Figure 3.13: An RF excitation pulse (a) and comparison between a conventional gradient-echo (b) and EPI (c) acquisition. T_{acq} indicated the acquisition time and FID - free induction decay (in this case - gradient echo - it is a T_2^* decay).

the phase-encoding gradient in Fig. 3.14 refer to the trajectory shown in Section 3.2 Fig. 3.3. Each echo is formed at a different echo time (TE), and the corresponding signal decays as follows:

$$S(n) = S_0 e^{-\frac{\text{TE}(n)}{T_2^*}}, \quad (3.23)$$

where "n" is the echo index in the echo train, and S_0 is the signal at $t=0$. Equation 3.23 neglects the contribution of the initial phase-encoding gradi-

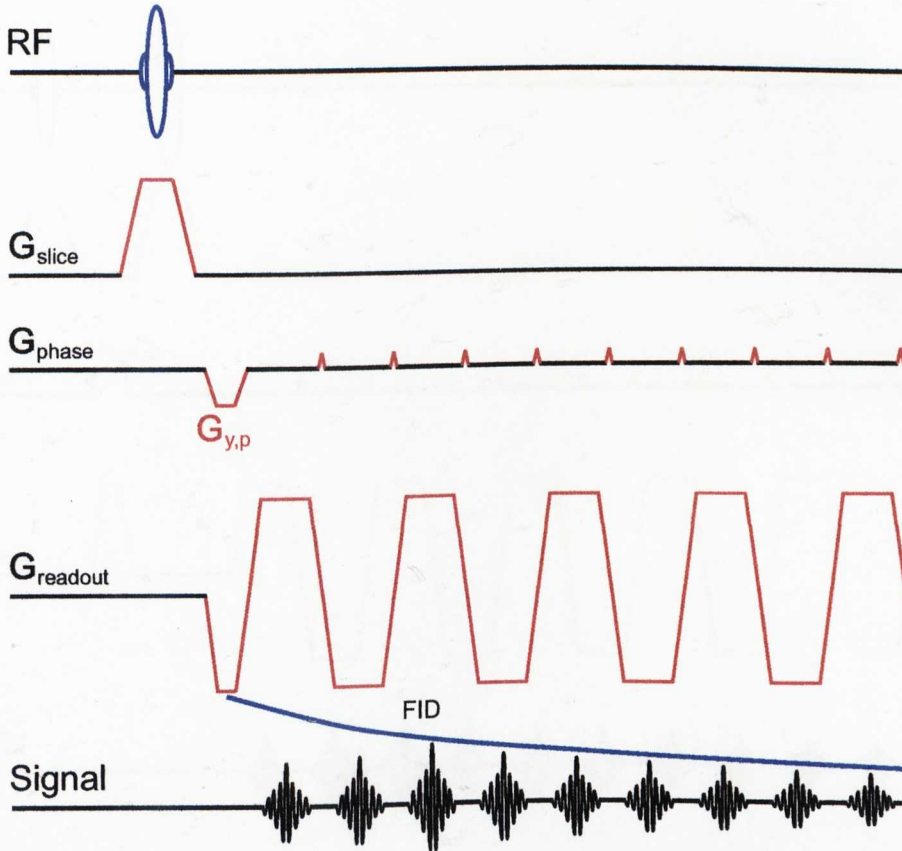


Figure 3.14: Pulse sequence diagram of a gradient-echo EPI pulse sequence. FID indicates a free induction decay (T_2^*) and $G_{y,p}$ represents a prephasing gradient lobe. The corresponding k-space trajectory is shown in Fig. 3.3.

ent to the overall signal amplitude of the echoes; only an FID component is considered.

As gradient-echo EPI is based on the T_2^* contrast it plays an important role in neurofunctional MRI (fMRI) such as Blood Oxygenation Level Dependent (BOLD) contrast [17], which is based on susceptibility variations (Section 4.5).

Spin-echo EPI (SE-EPI) employs an additional refocusing RF pulse (180°) in the transverse plane (Section 3.3). When applying the 180° RF pulse, the prephasing gradient lobe has to be applied with reversed polarity to the one in the gradient-echo sequence, as the 180° pulse already reverses the spins' polarity. It is common to use the prephasing lobe before the refocusing pulse, so that the time after the pulse can be more efficiently used to produce echoes.

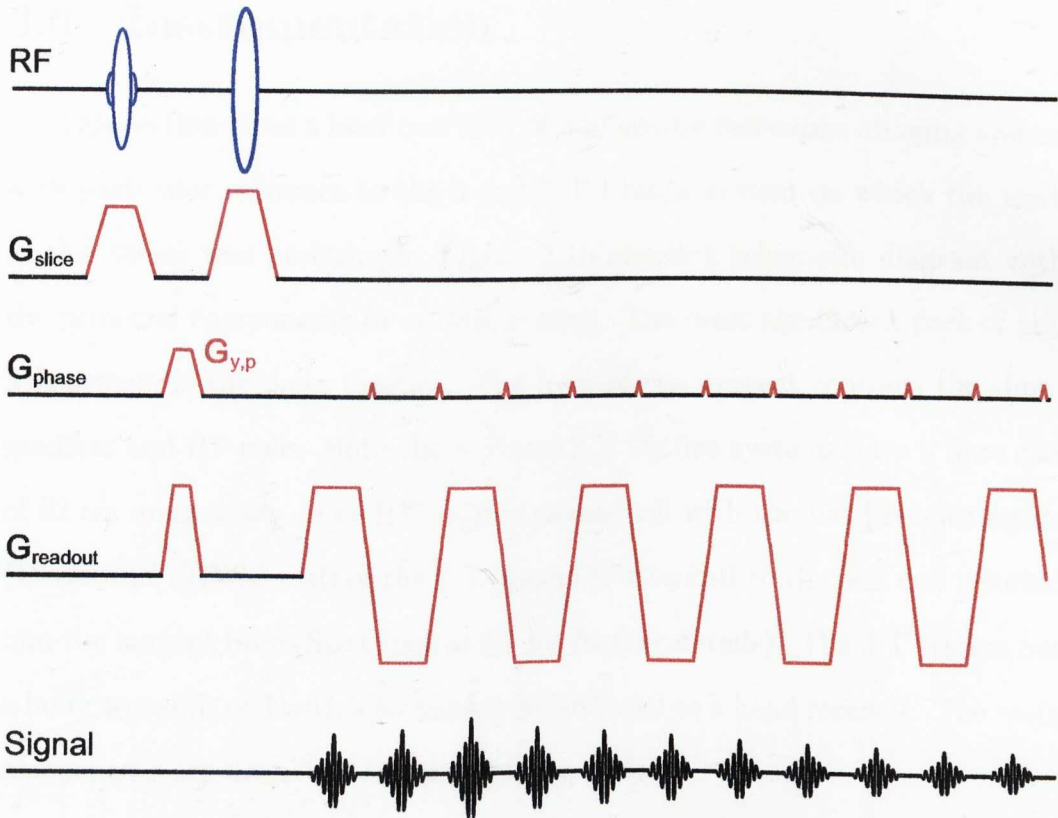


Figure 3.15: Pulse sequence diagram of a spin-echo EPI pulse sequence. $G_{y,p}$ represents a prephasing gradient lobe, note the polarity here is the same as the blips.

Figure 3.15 represents a typical spin-echo EPI pulse sequence, where the signal echoes are being formed under the envelope of spin-echo instead of FID. The rest of the mechanism is the same as in the gradient-echo EPI.

As described in Section 3.3, spin-echo sequences (including for EPI) reduce the influence of off-resonance effects, therefore the contrast obtained due to this acquisition is based on T_2 .

Inversion-Recovery EPI (IR-EPI) is another alteration of the EPI pulse sequence, frequently used to attenuate cerebrospinal fluid (CSF), produce T_1 -weighted images, or produce T_1 maps. As suggested, IR-EPI images are based on the T_1 relaxation time and this sequence employs an inversion recovery module prior to either GE or SE-EPI pulse sequence acquisition [18].

3.6 Instrumentation

This section gives a brief overview of a magnetic resonance imaging system with particular reference to the 3 and 7 T Philips system on which the work in this thesis was performed. Figure 3.16 shows a schematic diagram with the principal components of an MR system. The most significant part of any MR system is the main magnet. The bore of the magnet contains the shim, gradient and RF coils. Both the 3 T and 7 T Philips systems have a bore size of 92 cm in diameter. The RF head transmit coil with the head receive inside (16-channel SENSE coil) of the 7 T system is attached to the bed and inserted into the magnet bore (See Chapter 4.1 for further details). The 3 T system has a body transmit coil with a 8-channel SENSE coil as a head receiver. The main components are described in the following sections.

Figure 3.17 shows a diagram of a typical setup of the MR System. Arrows indicate the exchange of information between the different components of the system.

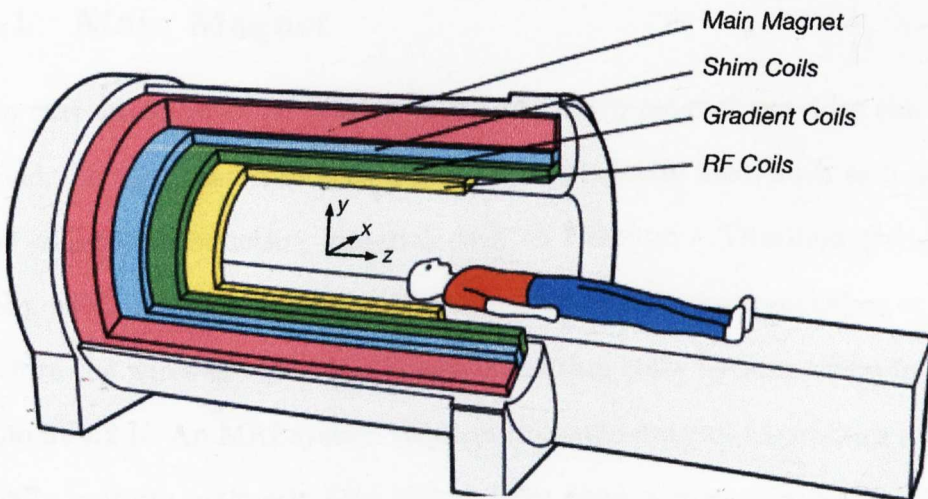


Figure 3.16: Schematic of a whole-body MRI scanner with cut-away section to show the principal components. Courtesy of Mike Poole [19].

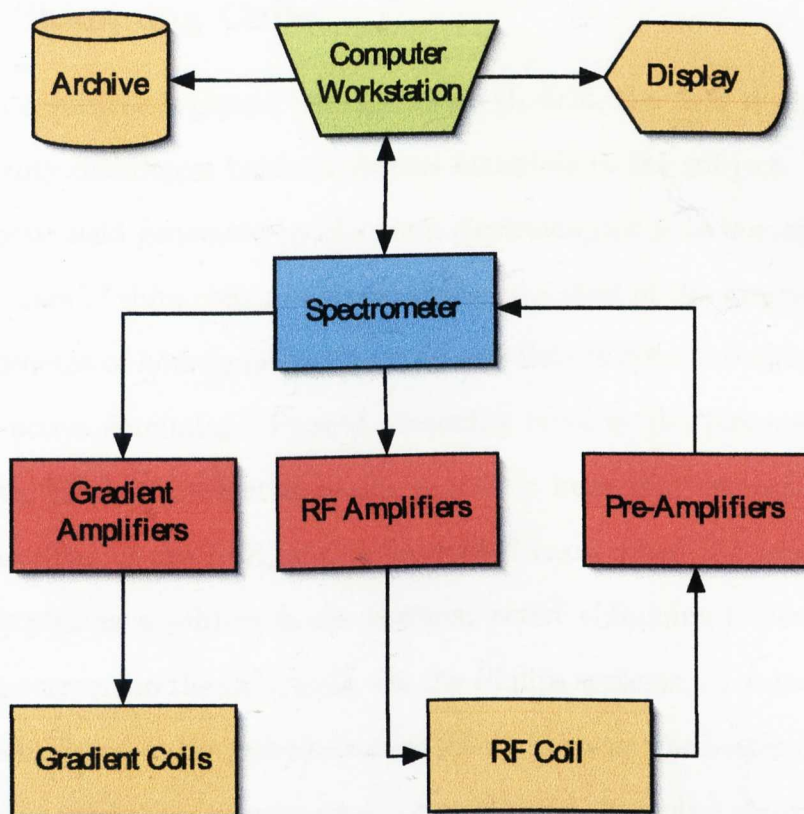


Figure 3.17: A diagram of a typical MR System setup. Courtesy of Nic Blockley [20].

3.6.1 Main Magnet

In current commercial MRI systems an electro-magnet provides the static B_0 field. To produce an intense homogenous magnetic field, such as 3 or 7 T, a coil of super-conducting material such as Niobium - Titanium (Nb_3Ti) is usually used. Nb_3Ti becomes superconducting at temperatures below ≈ 10 K, therefore the wires are held in a superconducting state by immersion in liquid helium at 4.2 K. An MRI system requires the main magnet to produce a highly spatially uniform magnetic field and to have good temporal stability. For the Philips 3 T and 7 T systems, the field stability is of the order of 0.10 ppm in a 25 cm diameter spherical volume and 0.24 ppm over a 30 cm diameter spherical volume, respectively.

3.6.2 Shimming Coils

When a subject is placed into the static B_0 -field, the field is distorted by susceptibility differences between various materials in the subject. To ensure the magnetic field generated by the main electromagnet is as homogeneous as possible, a set of shim coils are placed within the bore of the magnet.

The process of homogenising the magnetic field is done through both passive and active shimming. Passive shimming involves the placement of ferromagnetic blocks of material in the magnet's bore that correct for minor inhomogeneities of the field, and is assembled once, when the magnet is set up. After placing a subject in the scanner, active shimming is performed by adjusting currents in the shim coils. On the Philips systems, an auto-shimming routine is included in the pulse sequence set-up process. For better quality images, some experiments require small volume-based shimming assuring images free from artefacts in the area of interest [21].

3.6.3 Gradient Coils

Gradient coils are large resistive coils, usually positioned inside the shim coils, used to produce magnetic fields in the "x", "y", and "z" directions. These fields are used for spatially encoding the NMR signal for MRI as described in Section 3.3. Due to the high current carried by coils during an imaging sequence (≈ 600 A), the coils are often water-cooled to prevent overheating. The Philips gradient systems for the 3 T scanner produces a peak field strength of $80 \frac{\text{mT}}{\text{m}}$ while 7 T 40 $\frac{\text{mT}}{\text{m}}$, both using a slew rate of $200 \frac{\text{mT}}{\text{m}\cdot\text{ms}}$. 7 T was limited to $33 \frac{\text{mT}}{\text{m}}$ and $166 \frac{\text{mT}}{\text{m}\cdot\text{ms}}$ at time of scanning.

3.6.4 RF System

The RF system generates the oscillating B_1 -field to excite the sample and detect the resulting NMR signal. The RF coil is located within the gradient coils closest to the object that is to be scanned. The RF signal is generated by the spectrometer. An adjustable frequency synthesiser produces the pure radio frequency signal ω_0 , which is then mixed with a pulse envelope (for example a sinc function) and amplified: the Philips Achieva 3 T has an amplifier of 12 kW (whole body coil), the 7 T system is equipped with a 4 kW amplifier. The RF probe then converts the electrical signal from the power amplifier into a homogeneous oscillating magnetic field inside the sample. Following excitation, the system switches to receive mode. The receive probe detects the weak rotating magnetic field generated by the precessing spins and converts it back to an electrical signal via Faraday induction. The signal is amplified and passed to the spectrometer which uses two quadrature phase sensitive detectors. An 8-channel SENSEitivity Encoding technique (SENSE) coil was used in all experiments at 3 T, while a NOVA transmit head coil with 16 independent SENSE receive channels was used in all 7 T experiments. At 7 T, an additional coil (T/R - transmit/receive) was used for testing purposes included in Section 5.1.

Chapter 4

Perfusion and Functional Imaging Techniques

4.1 Overview of Techniques to Measure Blood Flow and Volume

There are several different methods to measure biological haemodynamic processes such as blood flow and perfusion, or blood volume. Positron Emission Tomography (PET), Single-Photon Emission Computed Tomography (SPECT), and traditional angiography are invasive methods as they involve either exposure to radiation or intake of a radioactive contrast or tracer, so they can not be used repeatedly i.e. for pharmacological monitoring. However, only a hand-full of methods are considered non-invasive, and MRI (without contrast agent enhancement) takes the lead in these procedures. The following sections outline the most common techniques to monitor haemodynamic-related processes. The technique used in this thesis – Arterial Spin Labelling (ASL) is described in detail in Sections 4.2 – 4.4.

4.1.1 PET and SPECT

Positron Emission Tomography (PET) and Single-Photon Emission Computed Tomography (SPECT) are nuclear medicine diagnostic tools that can measure perfusion. PET detects pairs of 511 keV photons as a result of positron annihilation from β^+ decay of radioactive isotopes - most common are ^{11}C , ^{13}N , ^{18}F , ^{15}O , ^{82}Rb , ^{62}Cu and ^{68}Ga . SPECT detects single photon emission by gamma-emitting radionuclides such as $^{99\text{m}}\text{Tc}$, ^{67}Ga , ^{111}In and ^{123}I . Although there are fundamental differences in both techniques, they both require the intake of radiopharmaceuticals to achieve signal for detection. Radiopharmaceuticals are metabolically active substances that are marked by a chosen radionuclide, carefully selected to target an appropriate organ of interest. One of the major advantages of PET imaging is existence of many low atomic number elements with positron-emitting isotopes; this permits incorporation of those isotopes to image very specific physiological properties of an organ. In both PET and SPECT, after the injection (or intake), radiopharmaceuticals are transferred through the blood stream and perfuse the target tissue (high metabolic demand in cancer cells) together with their attached radioactive isotopes. That place (or a body organ) then becomes a source of radioactivity later detected by a ring of crystals (PET) or gamma cameras (SPECT). However, a disadvantage to both techniques is very low resolution and lack of detailed spatial placing of the source, the latter can be improved by simultaneously using another, high resolution, imaging technique such as CT [22, 23] or MR [23].

4.1.2 Angiography

Angiography, also called arteriography, is a medical imaging technique used to visualise blood flow inside veins and arteries. The traditional method for

this involves injection of a radio-opaque contrast agent into a blood vessel and then monitoring its flow using X-ray fluoroscopy. The injection typically occurs into the femoral artery to visualise the arterial system and the left side of the heart, or into the femoral vein to image the right side of the heart and venous system. For both systems, images are normally acquired using a Digital Subtraction Angiography (DSA) technique, where the static tissue (including bones and other organs) is digitally removed from images. Vessels in the brain are normally imaged with a low temporal resolution of 2 – 3 images per second, whereas heart images typically require high temporal resolution of 15 to 30 frames per second. This information can then be used to evaluate the flow of the blood through the vessels.

Computed Tomography Angiography (CTA) and Magnetic Resonance Angiography (MRA) are nowadays commonly used to produce flow-sensitive images. Computed Tomography Angiography is a fast imaging technique that combines the use of X-rays, which are emitted from a rotating device at many angles to obtain projections, which are then assembled by computer into a 3D picture. The intake of the contrast agent is far less invasive in this method usually by a simple injection into a peripheral vein in the form of a bolus.

Magnetic Resonance Angiography (MRA) combines various MRI techniques to image vessels; most typical methods are:

- **Contrast Enhanced (CE-MRA)** - this is one of the most common clinical methods of acquiring MRA. The injection of the MRI contrast agent is typically in the form of a bolus into a peripheral vein. Image acquisition is during the first pass through the arterial system, where it results in a very high quality image. A variation of this method is the usage of the “blood-pool” contrast agent that remains in the blood stream for up to an hour, allowing for a longer acquisition time. The main disadvantage is, however, that both arterial and venous systems are imaged.

Dynamic Susceptibility Contrast (DSC) MRI (a variation of the CE-MRA) can monitor physiological parameters related to Cerebral Blood Flow (CBF), Cerebral Blood Volume (CBV) and Mean Transit Time (MTT) of blood passing through tissue. This technique requires a fast imaging technique to capture the signal loss due to the injected bolus of paramagnetic contrast agent passing through the tissue [24, 25]. Signal loss is due to spin dephasing (decreased T_2 and T_2^* values) and susceptibility effects magnify the signal loss [24, 26]. Intuitively, the strongest contribution of the contrast agent to the image is during the first passage although recirculation of the contrast agent can also be recorded, as shown in Figure 4.1.

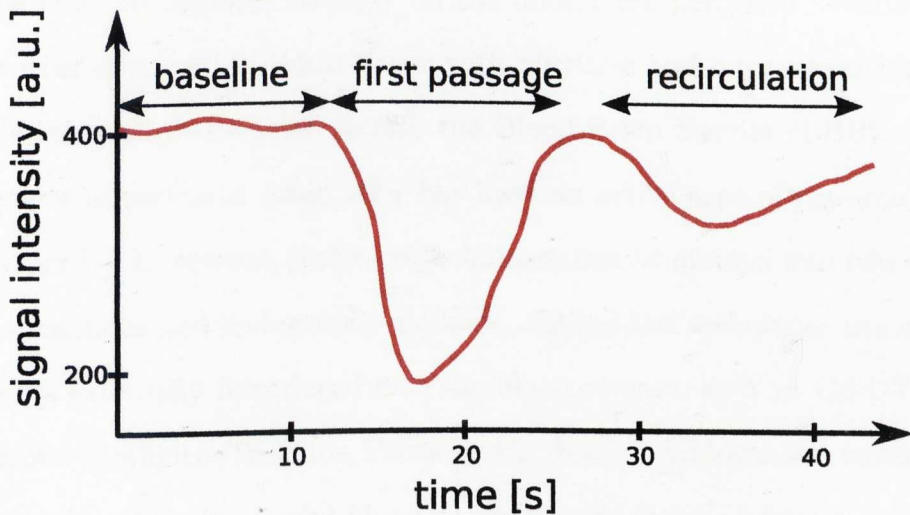


Figure 4.1: Schematic plot of signal reduction in DSC-MRI method; baseline, first passage and recirculation periods are marked. Schematic based on real data [25] for a Region Of Interest (ROI) containing the Middle Cerebral Artery (MCA).

- **Time-of-Flight (TOF) or Inflow Angiography** - this method, extremely popular in clinical applications, uses an imaging sequence with a short echo time (TE) and flow compensation, which saturates the static tissue signal making only the inflowing blood appear bright in images. The main disadvantage of this technique is its limited ability to detect

areas with slow flow, such as large aneurysms. This method is closely related to ASL.

- **Phase Contrast (PC-MRA)** - the phase of the magnetisation is modulated by gradients in such a way that it is directly proportional to the blood flow. This method can be used for both, blood flow visualisation and quantitative measurement.

4.2 Arterial Spin Labelling - What Does It Measure?

Tissue function depends strongly on the underlying perfusion. Perfusion is the process of supplying brain tissue with nutritive and oxygenated blood from arteries through exchange across the Blood-Brain Barrier (BBB). The measurement of perfusion using MRI has been an active area of research for over 15 years [1]. In general, perfusion techniques can be divided into two categories: exogenous and endogenous methods. Exogenous techniques use contrast agents externally introduced into the blood stream, such as Gd-DTPA (Gadolinium DiethyleneTriamine Penta-acetic Acid). Endogenous methods use the water protons in arterial blood as the tracer (natural contrast agent). The endogenous MR method is called Arterial Spin Labelling (ASL) or Arterial Spin Tagging. In ASL the magnetisation of water molecules of the inflowing arterial blood can be labelled by saturation [1] or inversion pulses [27, 28], altering the magnetisation of the arterial blood [1]. Labelled blood then progressively travels through the arteries and arterioles to the capillary bed where the magnetisation exchanges with that in the tissue, as water is a fast and freely diffusible tracer. ASL measures can be assessed either qualitatively or quantitatively. If two images are acquired, one with labelled blood and

a second non-labelled, then the difference image yields a qualitative map of perfusion (or Cerebral Blood Flow - CBF). Qualitative measurements result in Perfusion-Weighted (PW) images that are simply a percentage difference between labelled and non-labelled images. Quantitative measurements typically involve measuring the voxel signal intensity curve at a range of post-labelling delays and fitting to a complete perfusion or Arterial Cerebral Blood Volume (CBV_a) model [29, 30].

4.2.1 Cerebral Blood Flow (CBF) and Perfusion

Cerebral Blood Flow (CBF) and perfusion “ f ” are haemodynamic parameters, which are closely dependent on each other. Cerebral perfusion “ P ” is defined as:

$$P \equiv \frac{F}{W}, \quad (4.1)$$

where “ F ” is the cerebral blood flow rate $\left[\frac{\text{ml}}{\text{min}}\right]$ and “ W ” is the tissue mass [100 g]. Very often (especially in MRI of brain) more useful is perfusion rate “ f ” given by:

$$f \equiv \rho P, \quad (4.2)$$

where ρ is the tissue density in $\left[\frac{100 \text{ g}}{\text{ml}}\right]$. Perfusion rate in literature is expressed in $\left[\frac{\text{ml}}{\text{ml}\cdot\text{min}}\right]$ [31, 32] or often as $\left[\frac{\text{ml}}{100 \text{ g}\cdot\text{min}}\right]$. The typical perfusion value for grey matter is $\approx 90 \frac{\text{ml}}{100 \text{ g}\cdot\text{min}}$ [33], white matter $\approx 20 \frac{\text{ml}}{100 \text{ g}\cdot\text{min}}$ [33], and the whole brain $\approx 50 - 60 \frac{\text{ml}}{100 \text{ g}\cdot\text{min}}$ [32, 33].

4.2.2 Arterial Cerebral Blood Volume (CBV_a)

Blood volume V is defined as the fraction of blood volume that occupies a certain amount of tissue (typically defined in terms of $\frac{\text{ml}}{100 \text{ g}}$). Blood volume can also be chosen to be expressed as a dimensionless fraction “ q ” (in [%]) of

the blood volume within the voxel volume V_0 ,

$$q \equiv \frac{V}{V_0}. \quad (4.3)$$

In context of the brain, blood volume is referred to as Cerebral Blood Volume (CBV) [32]. Total CBV is often measured using contrast agents methods. However, recently, there has been a lot of interest in measuring Cerebral Arterial Blood Volume (CBV_a), as effectively, this is the driving input causing changes in CBF. It has been shown that fractional changes in CBV_a are linearly related to fractional changes in CBF and oxygen consumption [34, 35]. CBV_a is the volume of the blood in arteries and arterioles, which, on activation, expand in diameter causing increase in blood volume. It has been suggested that CBV_a changes exceed CBV_v [36].

4.3 ASL Methods

ASL techniques can be classified into: continuous (CASL) [37] and pulsed (PASL) [38] ASL methods. Continuous ASL uses a long labelling time, so the label reaches a steady state in the tissue of interest. The major advantage of this method is much higher SNR over the pulsed ASL, and also simpler quantitative perfusion models. In the PASL technique, a bolus of arterial blood is labelled and passes through the tissue carrying a transient change in signal. Shorter labelling time with a greater efficiency and smaller RF power deposition are the most important advantages of this method [32], due to which, CASL often requires additional hardware to be employed.

4.3.1 Continuous ASL (CASL)

Continuous ASL (CASL) is the original method for arterial spin labelling. Proposed in 1992 [1, 27, 31], this method originated from angiography [31, 39]. Early techniques employed multiple saturation pulses [1], which was then replaced by the magnetisation inversion approach [27]. CASL relies on continuous, flow-induced, adiabatic inversion with simultaneous application of magnetic field gradient in the flow direction [31] (Fig. 4.2). This adiabatic inversion pulse alone does not carry any amplitude or frequency modulation, therefore, stationary spins are not under the influence of the adiabatic inversion [32]. By implementing concurrently a magnetic field gradient G along the direction of motion, spins located at position $r_0 = \frac{\omega_{rf}}{\gamma G}$ will be inverted. The inversion is usually applied for 2 – 4 s to ensure the complete filing of vessels and exchange with inverted arterial spins to the imaging slices. The most common spatial placement of the inversion plane is in the vicinity of Circle Of Willis (COW) or common carotid. Spins are inverted with efficiency α , which must be considered in the quantification process; typical efficiency values range from 80 – 98% [27, 31, 40–44].

To estimate perfusion to produce a non-label image, the control plane has to be inverted twice, which results in double RF deposition - higher Specific Absorption Rate (SAR), especially problematic in high magnetic fields of 3 T and above. In addition, CASL, with its prolonged train of RF pulses, is particularly sensitive to Magnetisation Transfer (MT) effects resulting in saturation of the static tissue signal in imaging slices. To lower exposure to the excess of SAR, a second RF coil is needed to expand limited ROI, which is an additional, hardware-based disadvantage and difficulty in using this method.

More recently, a hybrid of CASL and PASL techniques, pseudo-continuous ASL (PCASL), has been developed [45]. This method uses rapidly repeated RF pulses in place of the continuous RF and therefore overcomes the problems of

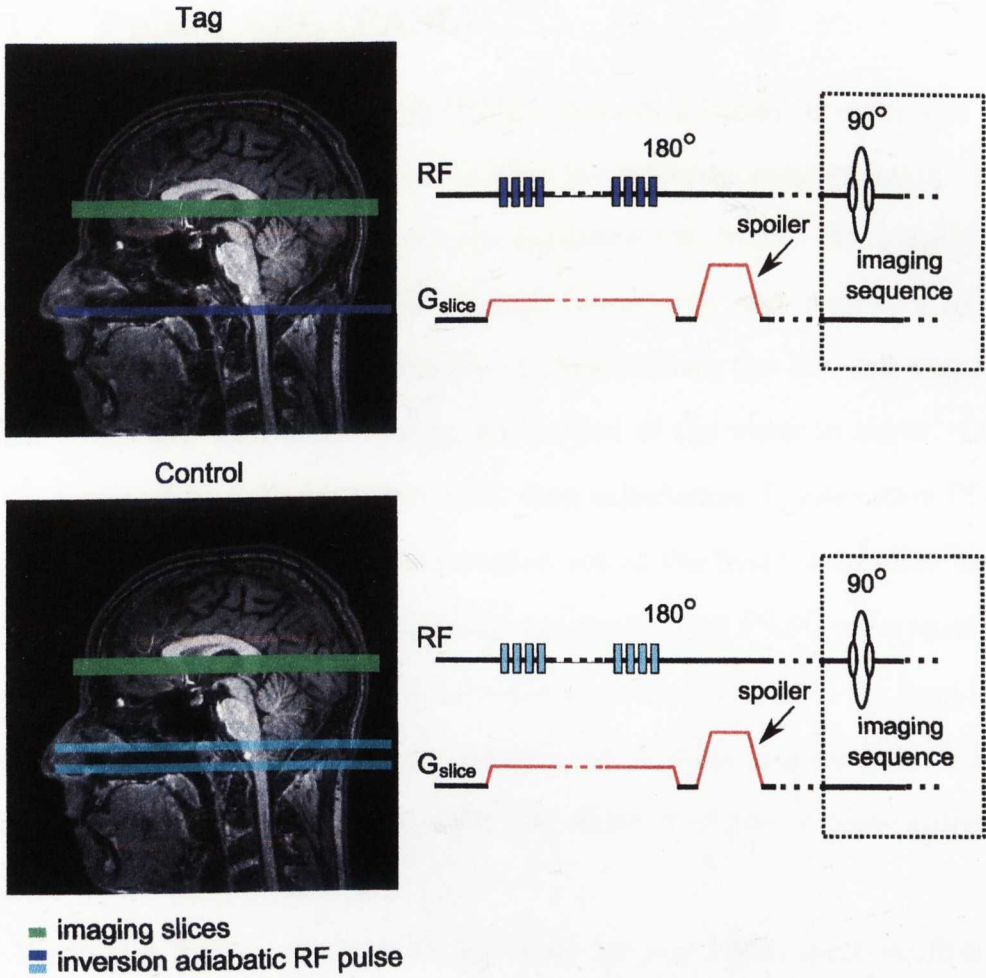


Figure 4.2: Schematic diagram of Continuous Arterial Spin Labelling technique. Tag (top) and control (bottom) images are shown with the spatial inversion of tag and control (blue) and imaging slices (green). Pulse sequence for tag and control shown on right.

needing two RF coils or exceeding a safe SAR, and is advantageous for scanning as it provides an optimised SNR. After repeated application of RF pulses the magnetisation reaches a steady state. The z-component of the magnetisation, M_z , in the steady state conditions is dependent on the flip angle of the RF pulse, θ , and the phase shift experienced during the time between pulses, ϕ (Eq. 4.4).

$$M_z = \frac{\pm M_0 \sin \theta \sin \frac{\phi}{2}}{\sqrt{(1 - \cos \theta)^2 + \sin^2 \theta \sin^2 \frac{\phi}{2}}} \quad (4.4)$$

4.3.2 Pulsed ASL (PASL)

Pulsed Arterial Spin Labelling (PASL) denotes a family of sequences and spatial techniques that use a bolus to label the inflowing magnetisation. This approach is far less demanding on the hardware and lowers the specific absorption rate. The bolus travels through the arteries and arterioles to the capillary bed (recovering with the T_1 of blood) where the labelled magnetisation exchanges with unlabelled magnetisation of the water in tissue. Once in the tissue, the labelled magnetisation then experiences T_1 relaxation (T_1 of tissue) and eventually recovers and washes out as the fresh, unlabelled blood arrives in the imaging slice. The most commonly used PASL techniques are discussed later in this section. These techniques are described in the form they were initially introduced. However today most of these sequences have been variously optimised for example with the addition of pre- | post-saturation pulses.

Figure 4.3 represents the basic sequence for any PASL method; first we label arterial blood then we perform a readout sequence of the desired slice, slices or volume. In-plane pre- and post-saturation pulses are optional but

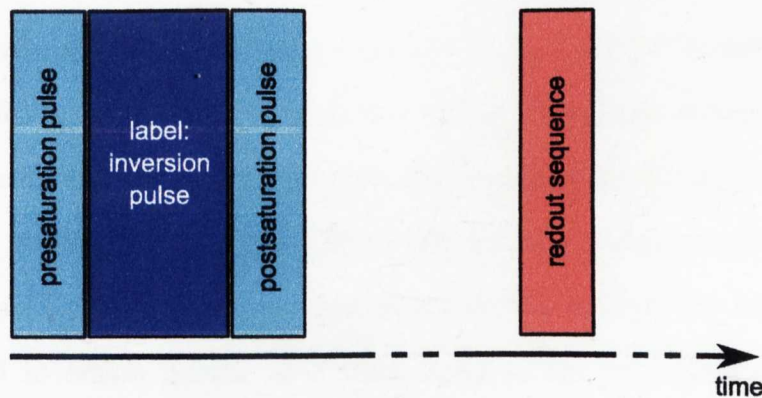


Figure 4.3: Schematic diagram of a general pulse sequence of the Arterial Spin labelling. Turquoise boxes represent pre- and post-saturation pulses played immediately before and after the label – blue box (180° inversion pulse). The red box represents the beginning of the readout sequence.

commonly used in most of the sequences because they limit the effect of poor labelling pulse profile (180° inversion). In-plane saturation becomes more of a requirement at higher fields, where the 180° pulses are even more susceptible to imperfections in their profile and efficiency across the volume. Typically the in-plane presaturation uses a WET scheme [46] and the postsaturation uses a single sinc pulse.

4.3.2.1 STAR

In the STAR (Signal Targeting with Alternating Radiofrequency) technique [28], the sequence begins with an in-plane (90°) saturation pulse to minimize possible perturbations in the imaging slice from the labelling inversion pulse. The RF pulse is typically followed by an additional spoiler to dephase the magnetisation. After the initial saturation, a spatially selective adiabatic inversion pulse is played (Fig. 4.4). The spatial placement (carrier frequency) of the 180° (typically adiabatic hyperbolic secant or FOCI inversion [47–49]) pulse differs between the tag and control images such that the tag is played below the imaging slice and the control is played above the imaging slice at an equal distance from the centre of the slice. This approach avoids discrepancies in static tissue signal between tag and control as a result of the magnetisation transfer effects. However this original approach would not accurately correct for MT effects away from the isocentre and in particular for multislice acquisitions. A multislice version of EPI STAR has since been developed, which applies two 180° pulses back-to-back to act as the control [50] Following the tag/control inversion pulses, at a time equal to the post-label delay (often referred to as TI period), a Spin Echo EPI (SE-EPI) or Gradient Echo EPI (GE-EPI) pulse sequence is typically employed to collect images.

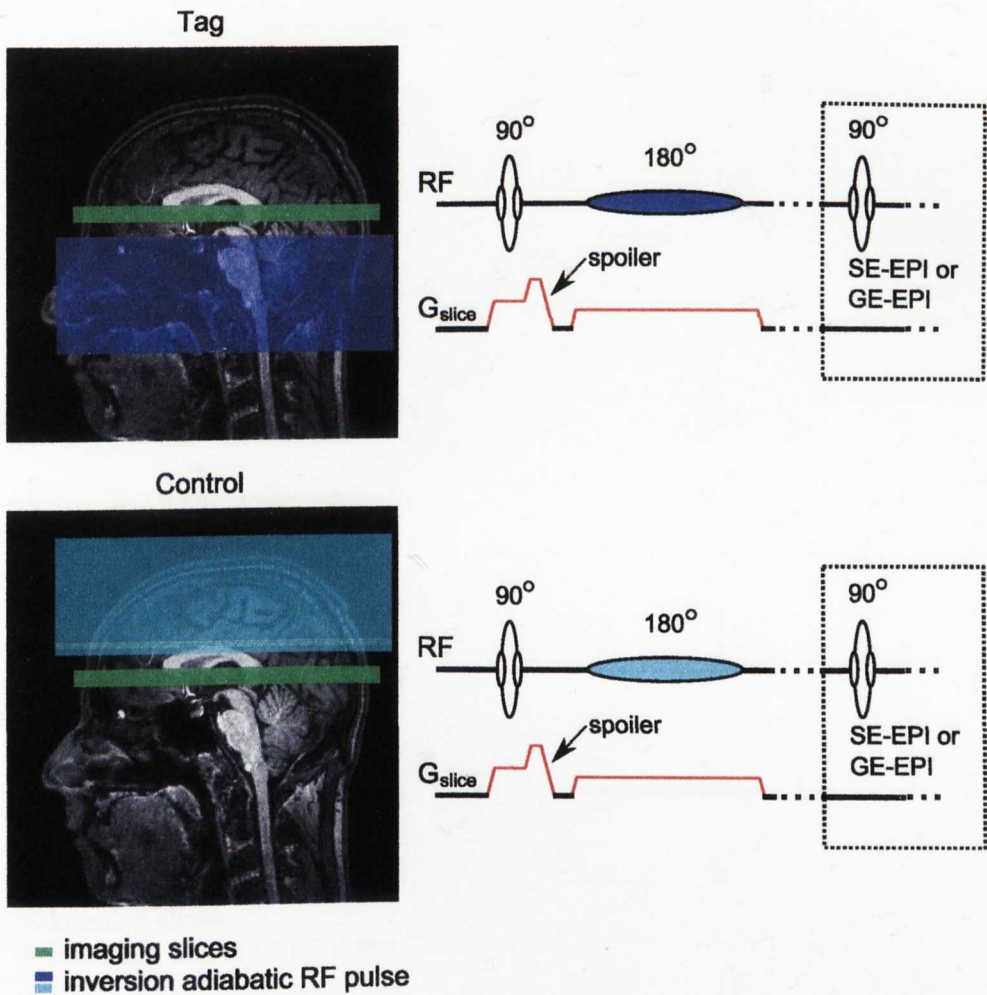


Figure 4.4: Schematic diagram of the traditional STAR labelling technique. Tag (top) and control (bottom) images are shown with the spatial inversion of both labels (blue and turquoise) and imaging slices (green). Schematics of the RF and slice-selective gradient of the sequence are shown. It can be seen that gradients are identical for tag and control resulting in equal eddy current effect. Here the frequency offset is alternated tag and control conditions (blue and turquoise).

4.3.2.2 PICORE

PICORE (Proximal Inversion with a Control for Off-Resonance Effects) [46] is a variation of the STAR technique. Figure 4.5 shows the spatial placement of inversion pulses and imaging slices accompanied by the schematic representation of the pulse sequence. The tagging is identical to that used in STAR, however for the control, the inversion (180°) is played out without the slice-

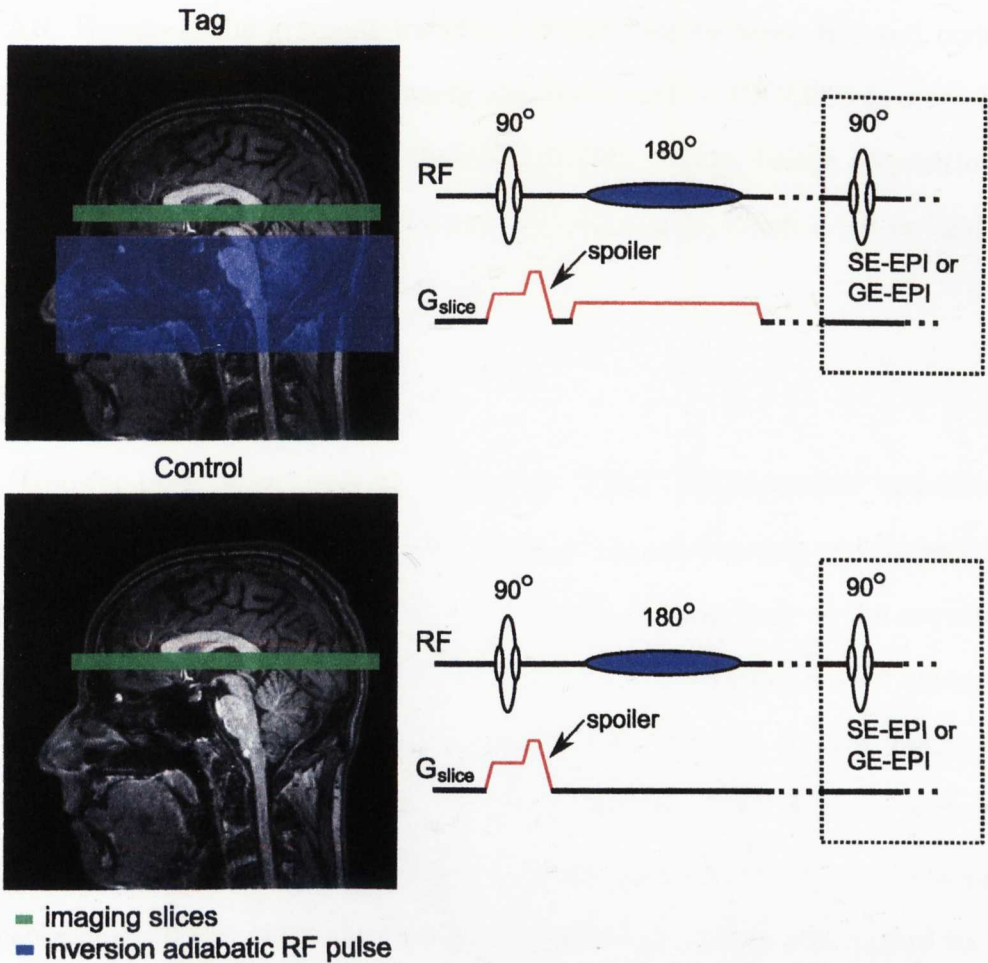


Figure 4.5: Schematic diagram of the PICORE labelling technique. Tag (top) and control (bottom) images are shown with the spatial inversion of both labels (blue and no inversion in the image for tag and control conditions, respectively) and imaging slices (green). Schematics of the RF and slice-selective gradient are shown. G_{slice} can be seen to be modified between tag and control, which can lead to eddy current effects.

selective gradient, therefore the control image does not experience any inversion (hence, in Fig. 4.5 the inversion is not marked in the control image). Because RF inversion pulses with identical frequency offset are played for both tag and control scheme, the magnetisation transfer effects are the same for both and subtract out. In addition, the asymmetry in magnetisation transfer effects, which occur in a multislice volume acquisition for traditional STAR, is also compensated in PICORE, which provides a slight advantage over EPI

STAR. However, the gradient waveform is different between tag and control (no slice-selective gradient in control sequence) and so PICORE is more susceptible to eddy-current effects than STAR [32]. Again, image acquisition is then performed after a post-label delay (TI) often using either a GE or SE-EPI sequence.

4.3.2.3 TILT

Transfer-Insensitive Labelling Technique (TILT) [51] is another variation of the PASL technique. In this method, the labelling scheme uses two consecutive 90° spatially selective pulses (Fig. 4.6). In the tagging part of the sequence, both 90° pulses have the same phase, effectively producing a 180° inversion at the selected location (blue box in Figure 4.6). For the control image, the 90° pulses are out of phase (the two pulses perform a 90° rotation and then -90° rotation) resulting in a 0° effective pulse width with the magnetisation experiencing no net nutation. Because the tag and control are applied in the same spectral location with reference to the imaging slice (and using identical power RF pulses), any magnetisation transfer effects are cancelled on image subtraction. TILT method is more resistant to the venous inflow than STAR and FAIR (discussed next). However, this method was developed at 1.5 T and when applied at 3 T, the effectiveness of the tag and control pulses is reduced, which can lead to poor labelling efficiency and the control not being 0° , which decreases signal in the perfusion weighted images.

4.3.2.4 FAIR

Flow-sensitive Alternating Inversion Recovery (FAIR) [52, 53] employs a frequency selective inversion pulse with and without an accompanying slice-selective gradient (or with a reduced one) to produce tag and control images, respectively. Similarly to STAR, the inversion is typically performed using

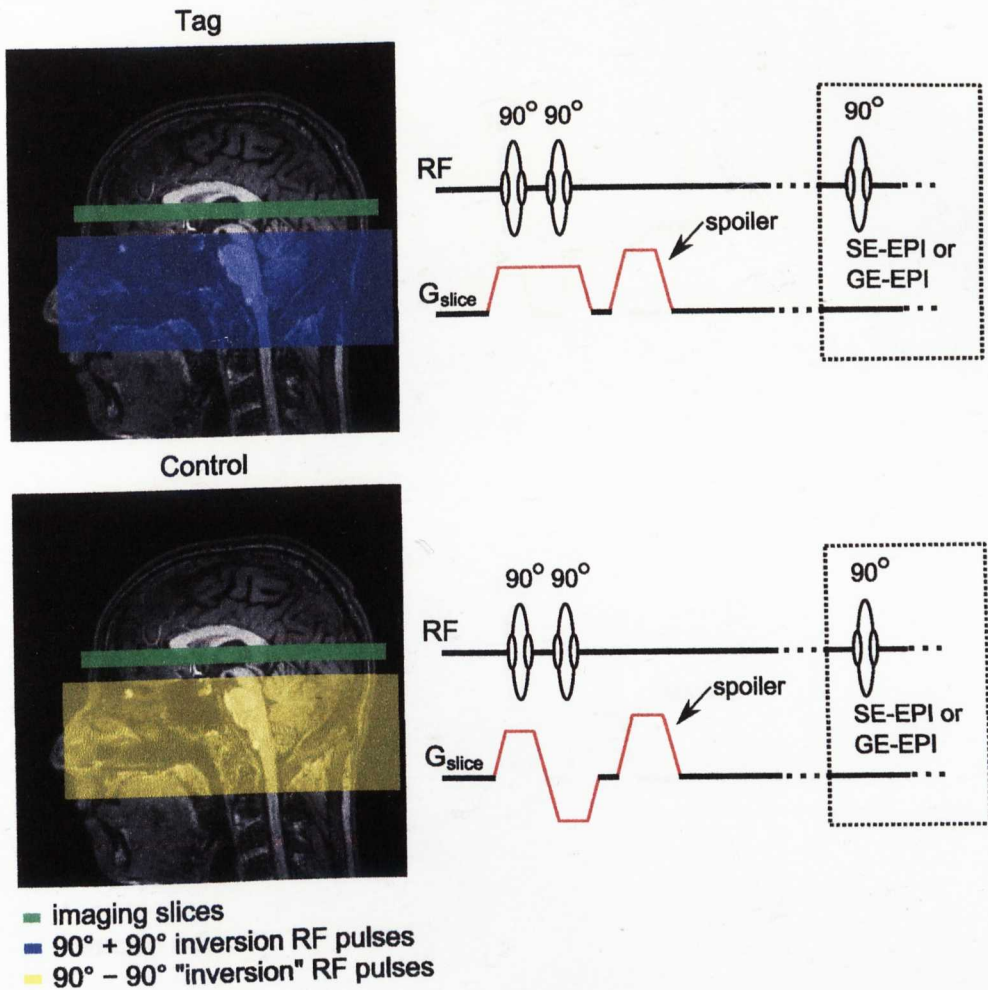


Figure 4.6: Schematic diagram of the TILT labelling technique. Tag (top) and control (bottom) images are shown with the spatial inversion of both labels (blue for $90^\circ + 90^\circ$ and yellow for $90^\circ - 90^\circ$ pulses) and imaging slices (green). Schematics of the RF and slice-selective gradient parts of the sequence are shown. The phase of the second 90° pulse is altered between tag and control.

a hyperbolic secant adiabatic pulse (bandwidth of 1 – 5 kHz); for optimal labelling FOCI pulses are used. The ideal FAIR scheme would employ a 180° slab over the imaging volume to produce the tag image, and over the entire coverage of the coil to produce the control image. Realistically, in the tagging part of the sequence the selective inversion must cover more than imaging volume due to imperfect pulse profile (side-lobes) and the inversion width in the control image is selected to assure arrival of the inverted blood to the imaging slice (Fig. 4.7). In addition, often a head only coil is used for the

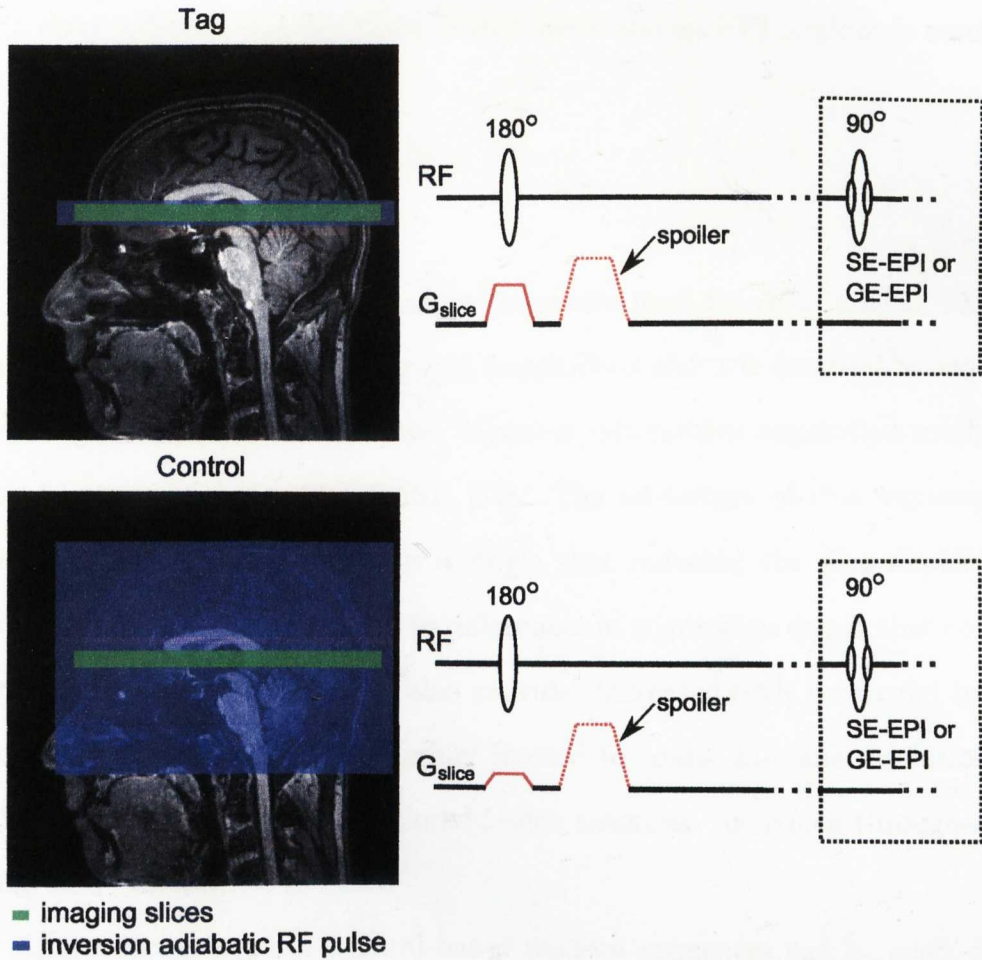


Figure 4.7: Schematic diagram of the FAIR labelling technique. Tag (top) and control (bottom) images are shown with the spatial inversion of both labels (blue) and imaging slices (green). Schematics of the RF and slice-selective gradient are shown. The gradient amplitude can be seen to alternate between tag and control conditions.

labelling (as used on the 7 T system described in Chapter 5). Under such circumstances, limiting the inversion pulse width in the control sequence is vital to avoid signal drop-off due to the coil efficiency and to assure arrival of the fresh, non-inverted blood at the beginning of the following tagging sequence. FAIR is resistant to magnetisation transfer effects with respect to the imaging slice if slices are centred at zero offset frequency. Again, the image acquisition is obtained following the post-label delay (TI) typically using one of the fast imaging sequences. FAIR is the labelling scheme, which was used for all the

ASL data collected and described in this thesis and an EPI readout is used for all acquisitions.

4.3.3 Image Readout

One of the most popular readout sequences used for ASL is EPI. This is since EPI provides a method of rapid acquisitions and it is essential to acquire the image before the label decays. However, alternative acquisition methods may be used, such as 3D-GRASE [54]. The advantage of this sequence is that it acquires a 3D volume in a single shot reducing the slice dependent variation in perfusion signal due to differences in acquisition delays that occurs with 2D multislice methods. It also provides increased SNR compared to 2D acquisitions. However, it is generally limited to coarse in-plane resolution to reduce off-resonance effects or limited slice thickness to reduce through-slice decay and blurring.

Alternatively, more structural-based readout sequences can be used, such as TurboFLASH [55] and TrueFISP [56, 57], which have been shown to be advantageous for body ASL applications.

4.4 ASL Applications: Functional and Pharmaceutical

Because the ASL signal is an absolute measure of CBF, this technique is more reproducible over time and between subjects [31] than for example Blood Oxygenation Level Dependent (BOLD) based methods. For this reason ASL is an excellent, non-invasive method to assess tissue metabolism and function. Cerebral blood flow increases as the brain performs a task and it is thought that functional perfusion maps are spatially more localised than BOLD, the

typical contrast used in fMRI (see Section 4.5) [34]. This and the fact that BOLD information can also be extracted from the ASL data [58,59] (co-adding tag and control images obtained by a T_2^* -sensitive sequence with a 90° readout pulse to receive the highest contrast to noise ratio), make this method a very flexible and powerful tool.

Pharmaceutical interest in using ASL arises from the non-invasive nature of the image acquisition. The perfusion-altering drugs can especially benefit from ASL as it allows frequent data collection and does not require the usage of any additional external tracers, where there is always a risk of unwanted interactions with the drug itself.

ASL can also be a useful tool in clinical applications such as in paediatric patients, to limit them to the radiation exposure during monitoring treatment progress. ASL can be an excellent supporting tool as well as the main method for diagnostic or monitoring purposes. Using the technique of territorial ASL [60–63] regional perfusion territories can be defined or multiphase ASL data (such as LLEPI acquisition, described in Chapter 6) can be used to assess transit time of labelled blood. These techniques are particularly useful in patients with cerebrovascular diseases, such as stroke, where they may have internal carotid artery occlusion or reduced cerebral haemodynamics, can also be monitored with their recovery process using ASL methods. Cancer cells change the perfusion providing the physicians not only with the accurate location but also with information regarding the aggressiveness of the disease.

ASL is not limited to brain imaging and can be applied to study perfusion in other organs such as kidneys in abdomen [64]. However, applications to other organs bring some challenges, particularly due to respiratory motion induced in the body, as the rest of the main internal organs are not as rigid as human brain.

4.5 Blood Oxygenation Level Dependent: Origin and Limitations

The most common technique for the functional study of brain activity is the Blood Oxygenation Level Dependent (BOLD) MRI contrast. However, BOLD is a qualitative measure and is still not well understood. On brain activation it is thought to be a disproportionate increase in cerebral blood flow (CBF and CBV_a) compared to oxygen consumption $CMRO_2$ (Cerebral Metabolic Rate of Oxygen uptake) [31], leading to a local increase in oxygenated blood, hence an increased MR signal. This increased blood oxygenation then creates an escalated oxygenation gradient to drive increased oxygen extraction.

The BOLD effect technique uses the natural contrast of the difference in magnetic susceptibility between oxygenated and deoxygenated haemoglobin contained in erythrocytes [17, 65–68]. Oxygenated blood is slightly diamagnetic (similar magnetic susceptibility to tissue), whereas deoxygenated blood is paramagnetic, causing dephasing of spins in the veins and perivenous tissue relative to surrounding tissue.

Figure 4.8 shows three different stages of the temporal BOLD haemodynamic response:

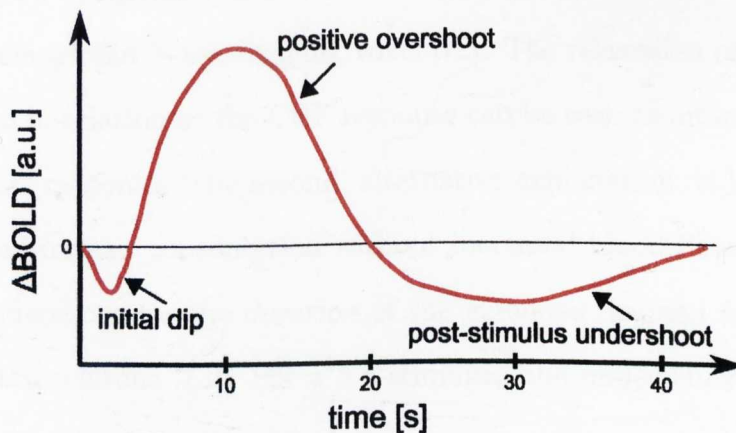


Figure 4.8: Schematic of typical BOLD response.

- **initial dip**; the short initial dip (2–3 second negative BOLD response) is thought to be due to the delayed CBF response to the oxidative demand in the stimulated area. This early response is particularly difficult to detect, as the fractional change in BOLD (ΔBOLD) is very small and requires high temporal resolution imaging technique and large Inter-Stimulus-Interval (ISI) in order to observe the initial dip. This feature is not often detected and its origin controversial [69–71]. This may be due to the initial dip being swamped by other underlying contributions to the image quality such as physiological or instrumental noise.
- **positive overshoot**; this is the main BOLD response and the length of it depends on the duration of the stimulus. Typically the peak of the BOLD response occurs at ≈ 6 s after stimulus onset. This prolonged response is due to relaxation of smooth arteriolar muscles continuing to supply the capillary bed with larger amounts of oxygenated blood after the ceased stimulus.
- **post-stimulus undershoot**; this final part of the BOLD response curve, unlike the initial dip, is well observed. The origin of this signal is still under debate. One of the hypotheses is that the venous compartment has a delayed compliance and results in the increased concentration of deoxyhaemoglobin in the imaging voxel [72]. The relaxation of this venous balloon in relation to the CBF response can be seen as an undershoot in ΔBOLD response. The second, alternative explanation, is based on the elevated oxygen consumption without increased blood flow resulting in the undershoot for the duration of the extended demand for oxygen in activated neurons [73]. For a 5 s stimulus, the undershoot can take as long as 1 minute to return to baseline.

The BOLD haemodynamic response can be assessed using fast GE imag-

ing sequences like gradient echo EPI, which are very sensitive to any inhomogeneities in magnetic susceptibility [32], therefore, a more direct method to isolate those components is needed in order to fully understand the Haemodynamic Response Functions (HRF). Arterial Cerebral Blood Volume (CBV_a) and Cerebral Blood Flow (CBF) are important haemodynamic inputs to any model of the BOLD effect [74–76] and measurement of these more direct components is needed in order to fully understand brain functions.

Chapter 5

Perfusion Imaging: Removing Noise Contributions from Static Tissue

5.1 The Roman Artefact

Magnetic resonance technology continuously expands and improves providing us with new tools for fast and accurate measuring methods. One of the most rapid MRI acquisitions is Echo Planar Imaging (EPI) [16]. This ultra fast acquisition speed comes with vulnerability to various image artefacts and distortions. Many system imperfections and physical phenomena result in commonly seen EPI artefacts such as: Nyquist ghosts [77], chemical shift, image distortion due to very low bandwidth in the phase-encoding direction, T_2^* -induced image blurring or intravoxel dephasing [32].

The Nyquist ghost appears as the result of misrepresentation of the k-space, signal amplitude modulation or phase inconsistencies, which can originate from a variety of sources [32]. There are also many ways to correct images for this artefact. The most popular method is to obtain a reference scan without phase

encoding the echoes (no gradient blip in the phase direction) to measure inconsistent phase errors between odd and even echoes [32,78–80]. Artefacts caused by chemical shift appear as a result of the difference in resonance frequency of protons in water and lipids (different proton environment). The chemical shift can be calculated for different B_0 fields and frequency matrices, therefore can be effectively suppressed [32]. These are only a few examples of commonly known artefacts and their remedies to show that there are methods to minimise their effect on image quality and reliability.

In research and development of medical imaging, there is always a possibility of discovering new artefacts such as a recently discovered banding artefact seen on 7 T Achieva Philips scanners, now commonly known to their users as the “Roman Artefact”. The Roman Artefact (RA) was first observed during a standard stability test of a new NOVA, 16 Channel, SENSE coil delivered to the system, in January 2007. This artefact is most apparent in EPI sequences (both gradient and spin echo) applied on 7 T Achieva Philips Scanners, and results in an incoherent banding effect on subtracted images (differences in signal intensity between dynamics).

5.1.1 3 T versus 7 T: Comparison

The RA manifests itself as a very significant difference in signal intensities between dynamics and can even reach 10 % or more in individual voxels of difference images at 7 T. To assess whether the artefact was specific to the 7 T hardware, data were also collected on a 3 T Achieva Philips System. Figure 5.1 shows a comparison of a four-compartment gel phantom ($T_1 = 1680, 1320, 960,$ and 600 ms) images obtained using the same EPI scanning protocol on 3 and 7 T scanners ($TR = 2000$ ms, $TE = 20$ ms, resolution: $3.75 \times 3.75 \times 5$ mm³, 1 slice per dynamic); original individual dynamics for 3 and 7 T, respectively (Fig. 5.1(a) and (c)) and below equivalent images representing subtracted dy-

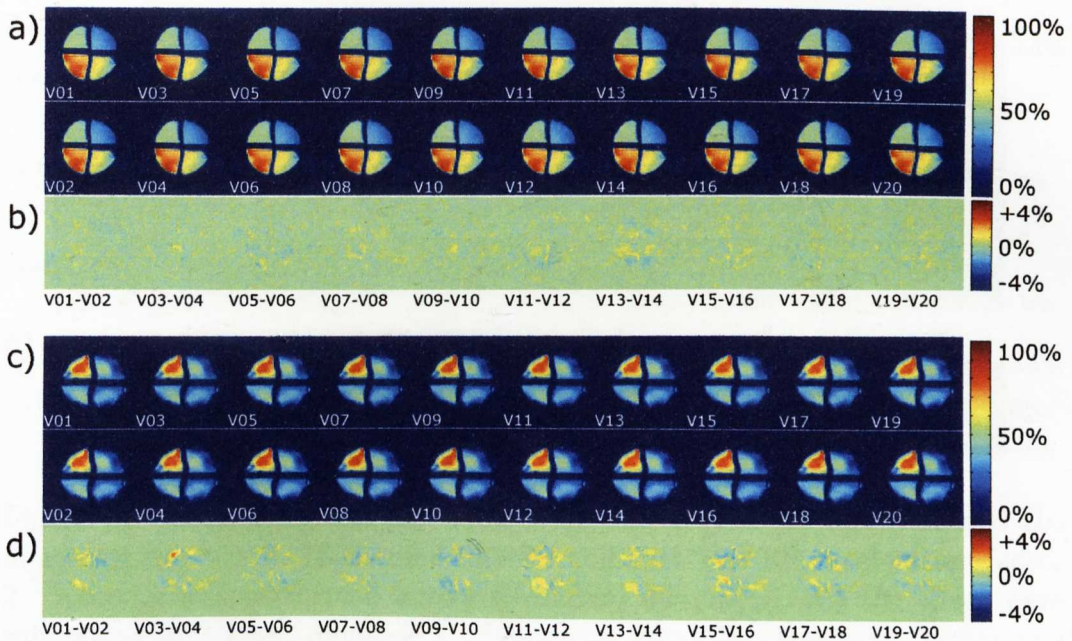


Figure 5.1: Individual dynamics of a four-compartment gel phantom ($T_1 = 1680, 1320, 960,$ and 600 ms) (a) and (c), and corresponding difference images (b) and (d) at 3 T and 7 T, respectively. All data collected using the same stability protocol provided by the scanner's manufacturer - Philips: ($TR = 2$ s, $TE = 20$ ms, res: $3.75 \times 3.75 \times 5$ mm³, 1 slice).

namics (Fig. 5.1(b) and (d)). In the images acquired on the 3 T scanner (Fig. 5.1(a)) we can see that when subtracting individual dynamics the difference images (Fig. 5.1(b)) show a noise level of no more than 1 %. However, in Fig. 5.1(c) and (d), a noticeable visible structure above the noise level is seen as an additional ripple effect throughout the imaging object. These variations in signal intensities are coherent, and so do not average out across the dynamics, as would be expected for random noise. In the averaged images the percentage variation was smaller, but the ripple effect was still very pronounced. Figure 5.2 shows the unaveraged difference images and the corresponding averaged images across all shown dynamics for the NOVA coil with SENSE acceleration factor 2, demonstrating that the Roman Artefact is coherent and fluctuations do not average out.

This instability in the images means the application of standard ASL meth-

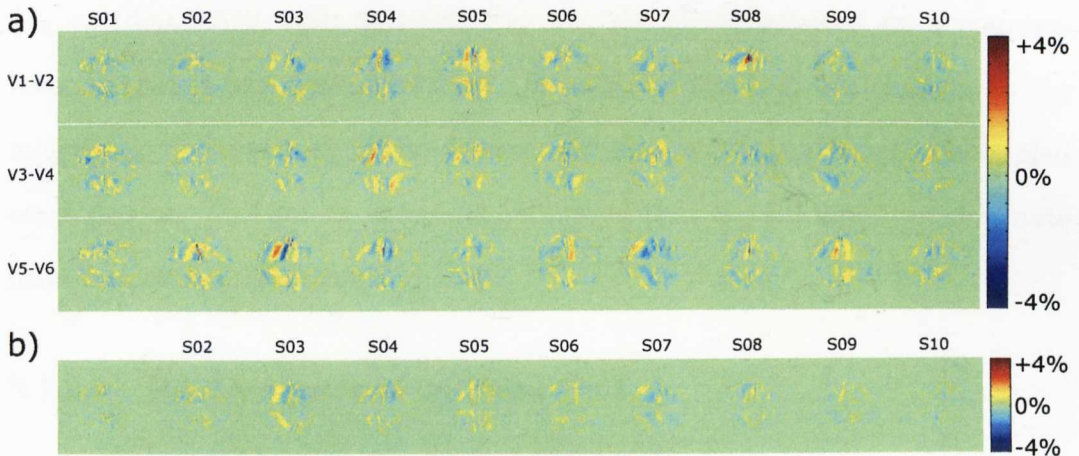


Figure 5.2: Comparison of the subtracted unaveraged (a) and averaged (b) images of the NOVA 16-channel SENSE coil with SENSE acceleration factor 2. Average was performed across 6 original dynamics. All the slices were subtracted as follows: dynamic 1 - dynamic 2 (V1-V2), dynamic 3 - dynamic 4 (V3-V4), dynamic 5 - dynamic 6 (V5-V6), etc.; TR = 2 s (default value of the stability protocol provided by Philips), TE = 20 ms, res: $3.75 \times 3.75 \times 5 \text{ mm}^3$, 10 slices.

ods (which rely on image subtraction) was impossible to perform with reliable results. The signal change between tag image and control image for PASL is at most 3 % of the original image intensity, and the Roman Artefact can easily be of this order or higher.

5.1.2 Effect of Scan Parameters on the Magnitude of the Roman Artefact

To investigate the origin of the Roman Artefact a series of experiments were performed at 7 T. This allowed us to narrow down the sources to then notify the manufacturer and obtain the remedy.

5.1.2.1 Mechanical Vibrations Effect

Prior to collecting data with varied scan parameters, vibration effects had to be eliminated as a source of the RA. A four-compartment gel phantom

($T_1 = 1680, 1320, 960,$ and 600 ms) was therefore balanced on a counter-lever so that it was decoupled from vibrations of the bed. No changes to the magnitude or behaviour of the Roman Artefact were seen for the decoupled environment. This set-up therefore confirmed that the RA does not originate from mechanical vibrations.

5.1.2.2 RA Dependence on Head Coil

Figure 5.3 shows variability of the Roman Artefact for various head coils. All of the examples clearly show significant RA on the acquired images. The difference images (pairwise subtraction as follows: dynamic 1 – dynamic 2, dynamic 3 – dynamic 4, etc.) display the behaviour of the artefact for the NOVA transmit coil with the 16 channel SENSE coil inside and SENSE 2 acceleration factor (Fig. 5.3(a)), NOVA coil with SENSE coil inside but no SENSE acceleration (Fig. 5.3(b)), NOVA coil acting as a T/R coil with the SENSE receive coil physically removed (Fig. 5.3(c)) and T/R coil Fig. 5.3(d). This suggests that the RA is not dependent on coil configuration as the signal intensity fluctuations are present in the same form and at the same level (approximately $\pm 5\%$) for all coils and SENSE settings.

5.1.2.3 RA Dependence on Phase-Encoding Direction and Slice Orientation

Phase-encoding direction was found to play a key role in the appearance of the Roman Artefact. Independent of the slice orientation, the RA banding effect always occurred in the phase encoding direction. Figure 5.4 shows images acquired at various slice geometries and phase-encoding directions. As shown, the RA banding direction changes with the direction of the phase-encoding gradient. However, the percentage value of the RA remains unchanged. This behaviour indicates some involvement of the phase gradients in the process of

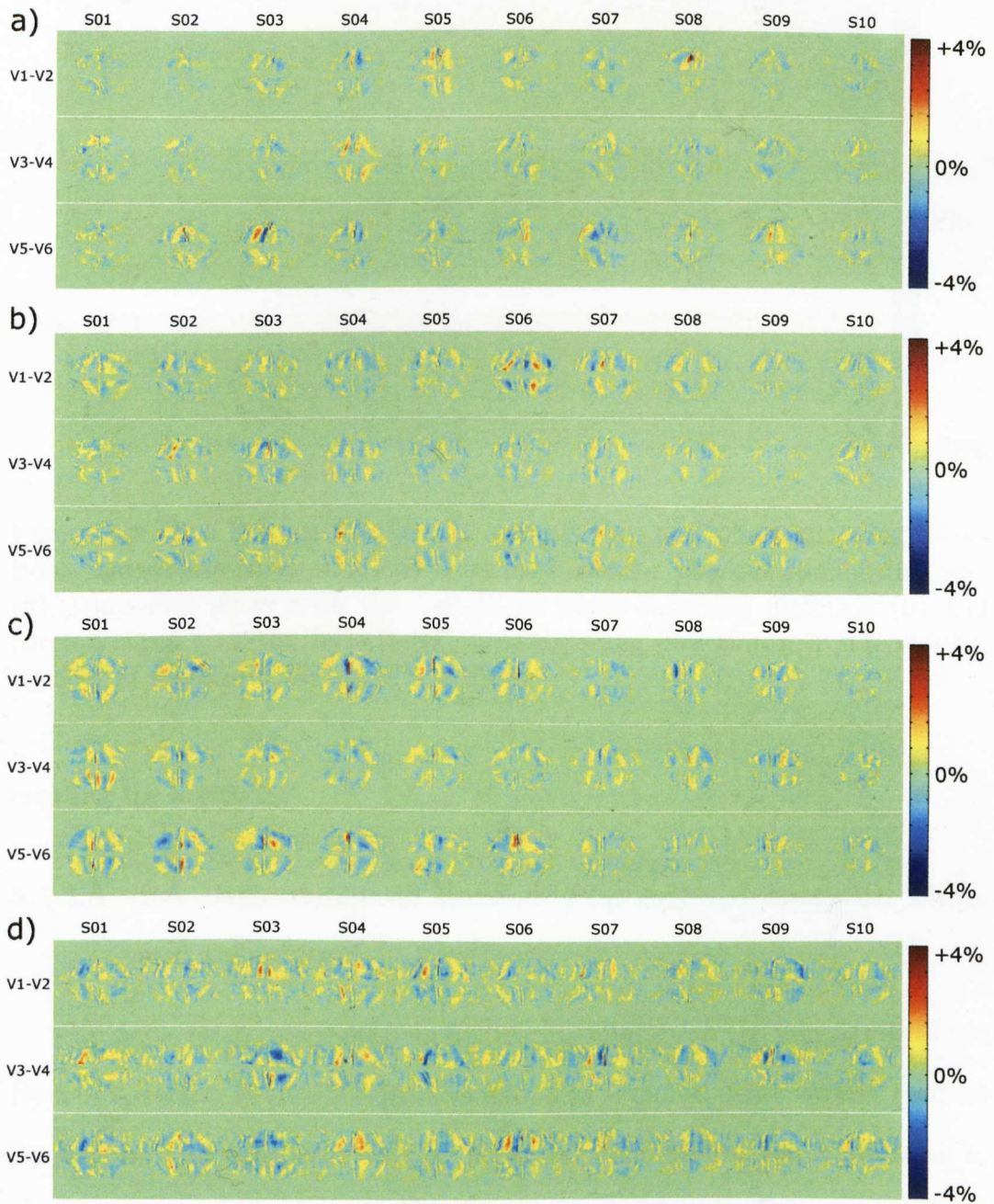


Figure 5.3: Comparison of difference images for the various coils and settings; (a) NOVA coil with 16-channel SENSE receive coil inside with SENSE acceleration factor 2, (b) NOVA coil with SENSE receive coil but no SENSE acceleration, (c) NOVA with SENSE coil physically removed, and (d) NOVA coil replaced by the T/R coil. All volumes are subtracted pairwise: dynamic 1 - dynamic 2 (V1-V2), dynamic 3 - dynamic 4 (V3-V4), dynamic 5 - dynamic 6 (V5-V6), etc.; TR = 2 s (default value of the stability protocol provided by Philips), TE = 20 ms, res: $3.75 \times 3.75 \times 5 \text{ mm}^3$, 10 slices.

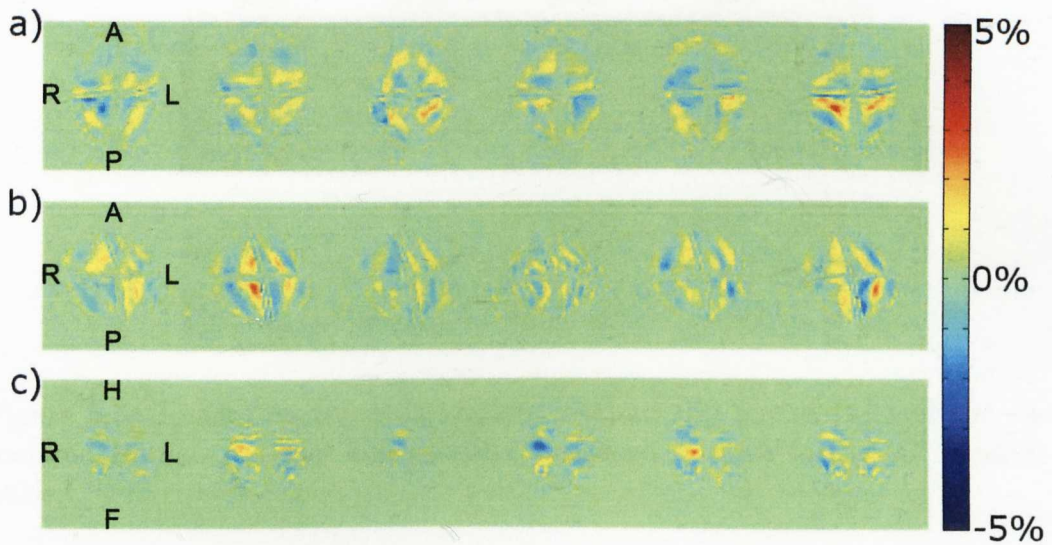


Figure 5.4: The Roman Artefact for various slice and phase-encoding directions: transverse slices with the Anterior-Posterior phase-encoding direction (a), transverse slices with the Left-Right phase-encoding direction (b) and coronal slices with the Foot-Head phase-encoding direction (c). TR = 10 s, number of slices $n = 10$, and TE = 20 ms.

creating the artefact.

5.1.2.4 RA Dependence on Readout Flip Angle, Repetition Time, and Echo Time

Flip angle analysis revealed an interesting relation to the magnitude of the Roman Artefact. Figure 5.5 displays data sets acquired using various readout flip angles. Analysing each data set separately, and scaling the modulation to the maximum pixel value of that same data set (absolute RA), it was found that the value of the RA remains virtually the same. However, when scaling all the images to the maximum pixel value of the image acquired with a 90° flip angle, the magnitude of the RA decreases as the readout flip angle is reduced (relative RA). This observation was very important as it led to the conclusion that the Roman Artefact is directly related to the signal intensity. Figure 5.6 shows the relative value of the RA as a function of the readout flip angle θ .

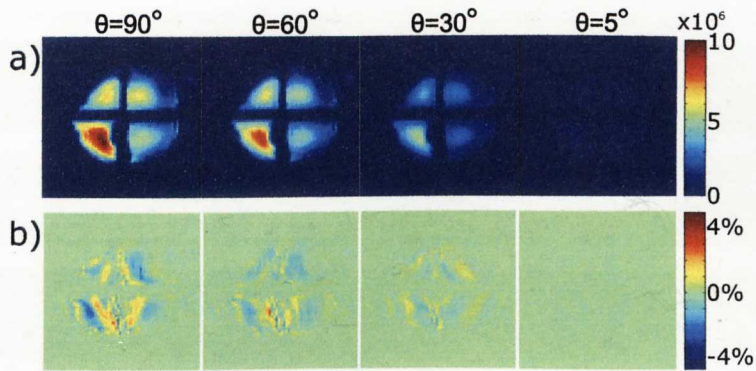


Figure 5.5: Images representing various readout flip angles (a) and the associated Roman Artefact contribution measured relative to the 90° readout pulse.

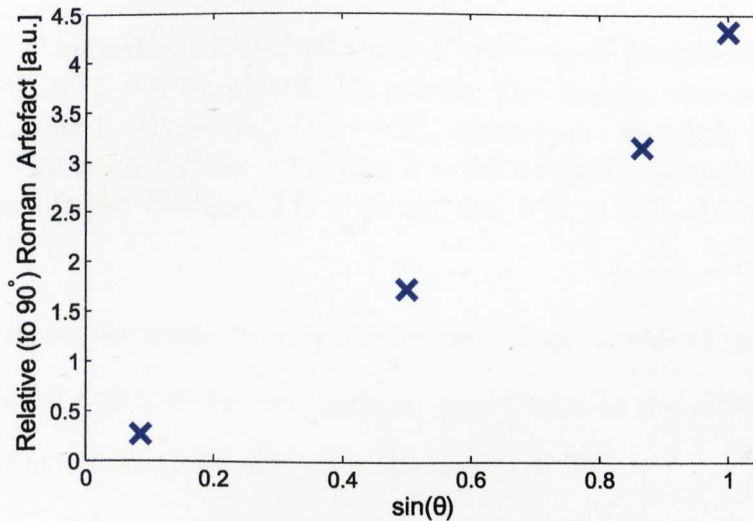


Figure 5.6: Relative (to the 90° readout pulse) Roman Artefact magnitude as a function of $\sin \theta$, θ being the flip angle applied.

To assess repetition time dependency, data sets were collected at a constant angle $\theta = 90^\circ$. No visible influence of $TR > 500$ ms on the magnitude of the RA (scaled to maximum pixel in its own data set), was found, calculated as a percentage value of each data set. Only when decreasing TR below 500 ms can we see the intensity fluctuations becoming more pronounced. This behaviour is expected as the system's stability has previously been shown to drop dramatically for short TRs. However, the absolute Roman Artefact is not affected by changes in TR, based on the same absolute RA level for $TR = 0.5$ to 10 s.

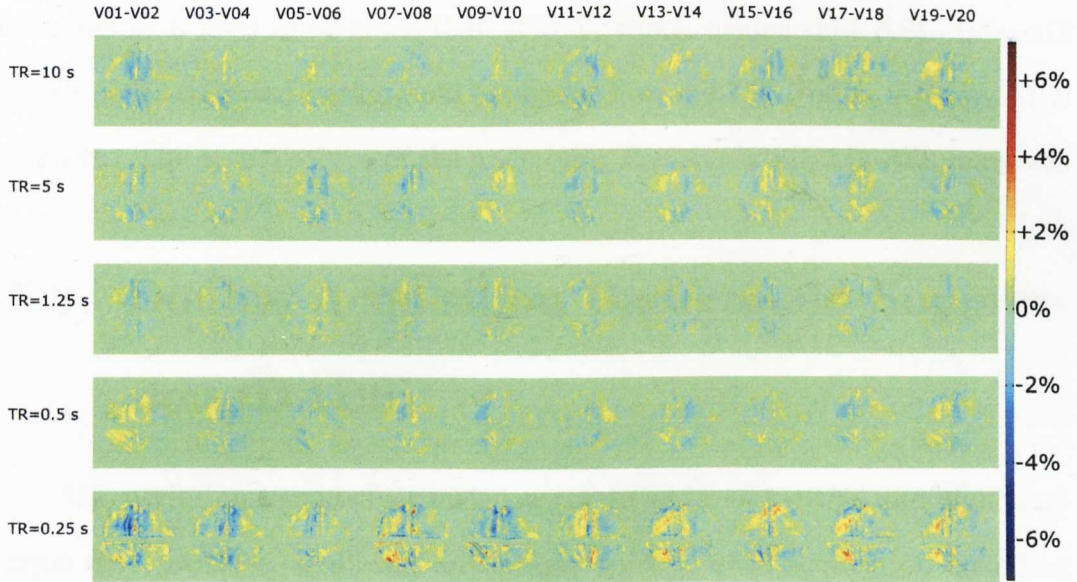


Figure 5.7: Comparison of the subtracted unaveraged images of the NOVA 16-channel SENSE coil for several TR values. The images were subtracted as follows: dynamic 1 – dynamic 2 (V1 – V2), dynamic 3 – dynamic 4 (V3 – V4), dynamic 5 – dynamic 6 (V5 – V6), etc.; $\theta = 90^\circ$ (default value of the stability protocol provided by Philips), TE = 20 ms, res: $3.75 \times 3.75 \times 5 \text{ mm}^3$, 1 slice.

Figure 5.7 shows the consecutively subtracted images acquired at various TR values, from 10 s to 250 ms. No changes were found in the absolute Roman Artefact behaviour directly related to the length of TE.

Due to the RA presence, it was not possible to perform a traditional acquisition method to obtain CBF or CBV_a images at 7 T. The size of the banding effect induced by the RA exceeded changes due to haemodynamic effects. However, given the finding that the RA was dependent on base image intensity, we implemented a Background Suppression (BS) method, where the static signal is suppressed and the ASL image is sensitive solely to inflow and perfusion-related effects (described in Section 5.2). This would thus suppress static signal fluctuation which could exceed perfusion-related signal changes.

Currently, the manufacturer provided the 7 T system with a new PTS board (with correctly calibrated spectrometer clock for the 7 T field) and the Roman Artefact has been now reduced in magnitude. However, the RA still

remains at a level of \approx twice that at 3 T, which means that ASL data still needs to be collected background suppressed on the 7 T Philips Achieva MRI scanner. The actual source of the underlying Roman Artefact is still unknown.

5.2 Double Acquisition Background Suppression (DABS)

ASL perfusion weighted signal is low (of the order of 1 – 3 %) and high magnetic field provides significant advantages to ASL data acquisition including increased image signal-to-noise ratio (SNR) and lengthened longitudinal relaxation times leading to increased contrast-to-noise ratio of ASL images [81]. These gains can be exploited to improve spatial resolution. However, ultra-high field also presents several challenges such as increased B_1 and B_0 inhomogeneity and increased physiological noise [82]. Physiological noise, arising from cardiac pulsation and respiratory motion from thoracic modulation of the magnetic field in the head, has been shown to add structured noise to perfusion and BOLD functional MRI data leading to a reduction in the SNR of perfusion measurements. Further, as demonstrated in the previous section, there is decreased stability due to the Roman Artefact at 7 T.

Image based correction methods of RETROICOR [83] and component based noise correction (CompCor) [84] techniques have been proposed to reduce the physiological noise. RETROICOR fits a low-order Fourier series to the image data based on the time of each image acquisition relative to the phase of the cardiac and respiratory cycles. CompCor uses principle components derived from a noise ROI as nuisance regressors in the General Linear Model (GLM) of the BOLD and perfusion time series.

An alternative method to reduce physiological noise in ASL sequences is to reduce the source of physiological noise – the static tissue signal. Background

Suppression (BS) techniques [85] have been proposed to reduce the effects of physiological noise by suppressing the static signal in ASL data prior to image acquisition. In a BS measurement the tag and control images are acquired close to their null point ($M_z = 0$), by applying a non-selective inversion recovery sequence prior to the ASL acquisition [85]. Figure 5.8 shows a schematic representation of a pulse sequence employing BS pulses. BS reduces noise from physiological sources, as well as the effects of head motion and other system instabilities, such as the Roman Artefact. However, the intrinsic suppression of static signal does prevent background suppressed ASL being used for the simultaneous measurement of BOLD and CBF. Simultaneous measurements of CBF and BOLD are important for many reasons for example the assessment of spatial localisation of CBF versus BOLD [86]. One particular use of combined CBF and BOLD is for a quantitative interpretation of BOLD, and to yield an estimate of the change in oxidative metabolism (oxygen consumption; Cerebral Metabolic Rate of Oxygen - $CMRO_2$) [87–89]. In addition, such methods may be particularly useful in studying and interpreting fMRI responses in which cerebrovascular changes can alter BOLD, such as in ageing-related diseases or due to pharmacological agents. Furthermore, the possibility of mo-

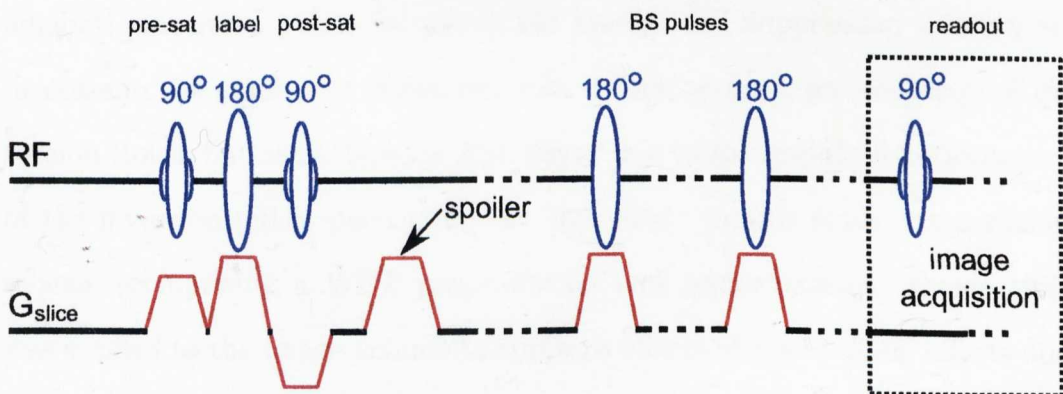


Figure 5.8: Schematic of a pulse sequence with two background suppressing adiabatic inversion pulses employed. For simplicity, only RF and slice selective gradient time lines are shown.

tion correcting background-suppressed ASL data is limited. Therefore here we implemented a technique called Double Acquisition Background Suppression (DABS) to address these issues obtaining a BOLD weighted ($TE \approx T_2^*$) second acquisition prior to the end of the ASL TR period.

The DABS approach is based on two acquisitions of the same volume in a single TR period. Following the labelling, the first volume is acquired at the delay (TI) time of interest, and the second at the end of the TR period, allowing simultaneous assessment of CBF (first acquisition) and BOLD (second acquisition). Here this method is applied to measure simultaneous CBF and BOLD changes in response to a finger tapping task at high field (3 and 7 T). For this method we assess physiological noise contributions and realignment issues to determine the benefits of background suppression techniques to study functional changes. The aim of this work is to determine how the ASL-fMRI signal is affected by the physiological noise sources and the gains that can be achieved by using DABS validated against the RETROICOR method.

5.2.1 Optimising Timing of BS Pulses

We first evaluated the optimal number and timing of the non-selective adiabatic inversion pulses for use in the background suppression scheme; an increase in the number of pulses provides nulling across a greater range of inversion times, but can attenuate ASL signal due to the non-ideal performance of the inversion pulse, particularly at high field. In this study a saturation scheme (comprising a WET presaturation and postsaturation scheme [46]) was applied to the image volume to suppress effects of static signal offsets due to differences in efficiency of the selective and non-selective slabs in the FAIR scheme. The theoretical static signal (normalised to $M_0 = 1$) following background suppression was simulated for each tissue type for normalised signal

change for 3 and 7 T using Eq. 5.1

$$S(t) = 1 - e^{-\frac{t - \sum TI_n}{T_{1,tissue}}} - S \left(\sum TI_n \right) e^{-\frac{t - \sum TI_n}{T_{1,tissue}}}, \quad (5.1)$$

where TI_n indicates the inversion time of the n^{th} background suppression pulse. Longitudinal relaxation times used for the simulations are given in Table 5.1. The optimal background suppression scheme for one, two and three background suppression pulses was then determined at each field strength for a post-labelling delay time of 1550 ms by iteratively varying TI and calculating a weighted Sum-of-Squares minimisation (using MATLAB) according to the following equation:

$$\text{SumSq} = \text{SumSq} + 4 (S_{GM}(TI))^2 + 2 (S_{WM}(TI))^2 + (S_{\text{blood}}(TI))^2 + (S_{CSF}(TI))^2, \quad (5.2)$$

where S_{GM} , S_{WM} , S_{blood} , and S_{CSF} represent normalised signal for grey matter, white matter, blood and cerebro-spinal fluid, respectively. In this way the data was more strongly weighted to suppress grey matter, with reduced weightings

Table 5.1: Assumed parameters used in the simulation of BS pulses [81].

Fixed Parameters	Assumed Values	
	3 T	7 T
Longitudinal Relaxation Time of White Matter ($T_{1,WM}$ [ms])	800	1200
Longitudinal Relaxation Time of Grey Matter ($T_{1,GM}$ [ms])	1300	1850
Longitudinal Relaxation Time of Blood ($T_{1,Blood}$ [ms])	1600	2100
Longitudinal Relaxation Time of Cerebro-Spinal Fluid ($T_{1,CSF}$ [ms])	3700	4500
Null Point (TI_0 [ms])	1450	1350

for white matter, blood and Cerebro-Spinal Fluid (CSF). To ensure that the images are acquired past the null point, it was chosen to optimise that the static signal was nulled at 1350 ms for 7 T and 1450 ms for 3 T for the acquisition to begin at 1550 ms. Acquiring data past the null point avoided the need for complex subtraction, which requires the need for good suppressing of static signal across the entire volume [90].

5.2.1.1 3 T Optimisation

The timing of the background suppression pulses is crucial in obtaining desirable reduction in overall image signal intensity. To assure that the magnetisation from all the considered brain tissue components passed the null point, allowing magnitude subtraction of the ASL data, it was aimed to null the static signal 100 ms earlier than the first acquisition ($T_{\text{null}} = 1450$ ms, $TI = 1550$ ms). The following sections present approaches for the BS pulses at 3 T.

(A) Double Acquisition FAIR, No Presaturation Module The simulated static tissue longitudinal magnetisation for Double Acquisition FAIR at 3 T are shown in Figure 5.9(a). In this simulation, a TR of 3 s was used according to experimental conditions, and so the signals are not equal to -1 at the $t = 0$ s (however the signals represent the stabilised magnetisation for short TRs). For one background suppression pulse, the weighted minimisation equation of the Sum-of-Squares (Eq. 5.2) leads to optimal nulling of grey and white matter. One non-selective inversion BS pulse at the optimal time of $TI_1 = 1008$ ms is shown in Figure 5.9(b) together with the second (BOLD) acquisition volume. Because the T_1 values of various brain tissues differ (Table 5.1), one background suppression pulse does not equally null across all tissue types, suggesting that a single background suppression pulse is insuffi-

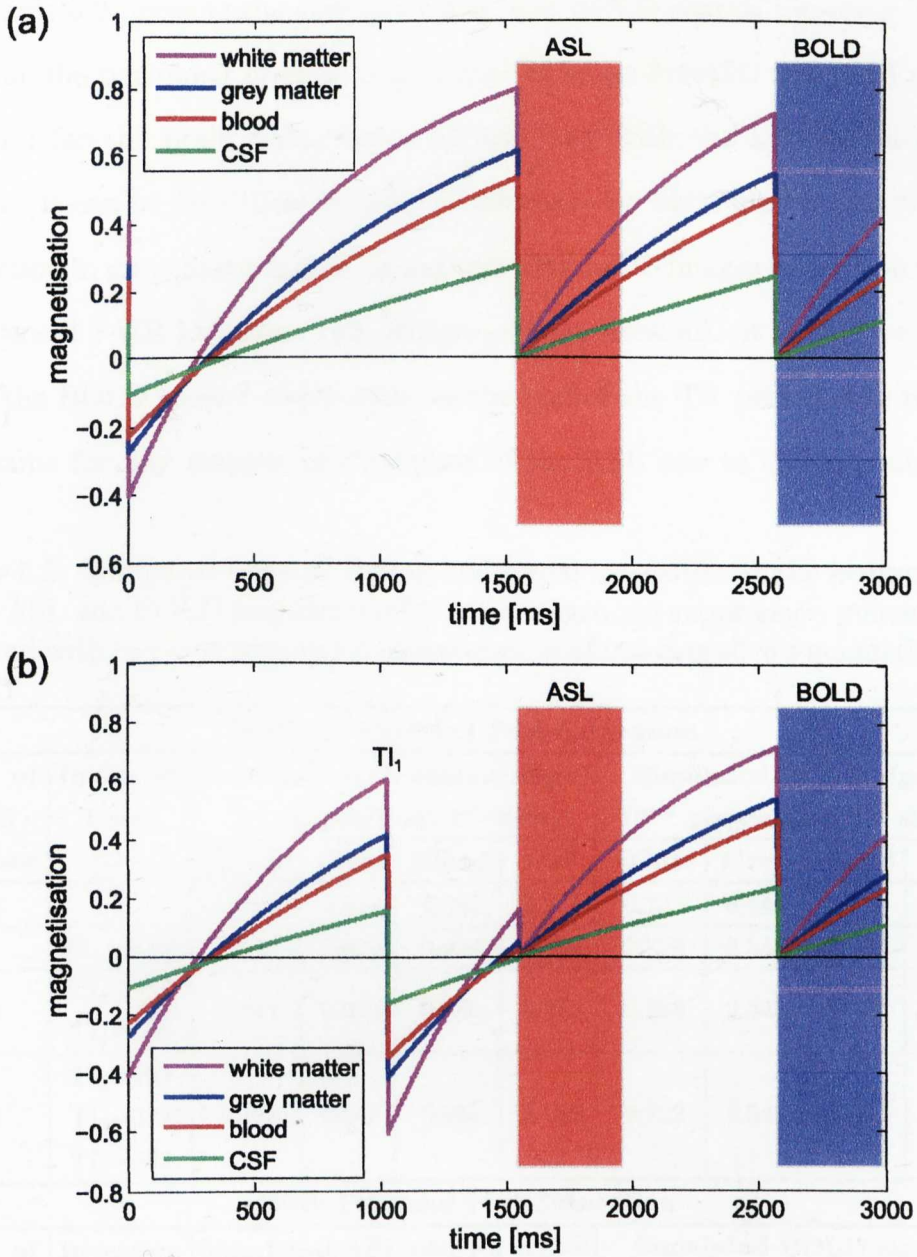


Figure 5.9: Simulated normalised inversion recovery signals of the longitudinal magnetisations for various brain tissues (white matter, grey matter, blood, and CSF) at 3 T without background suppression (a) and with one BS pulse applied at the optimal T_{I_1} time (1008 ms) (b). Red and blue blocks indicate 7-slice ASL and BOLD acquisitions, respectively. The initial value of the longitudinal magnetisation is presented for a TR of 3 s, as used experimentally for optimal SNR per unit time, whilst allowing good labelling. Hence, a time $t = 0$ the magnetisation is not equal to -1.

cient.

Table 5.2 presents the simulated ASL and BOLD signals (ignoring T_2^* decay) at the beginning of each acquisition (1550 ms for ASL and 2573 ms for BOLD) for the brain tissue types without and with the application of BS pulses. It can be seen there is $\approx 86\%$ reduction for white matter and $\approx 90\%$ reduction in grey matter signal, blood and CBF in BS images in relation to the traditional FAIR technique (no background suppression). It should be noted that the BOLD second acquisition, at the end of the TR period, will remain the same for any number of BS pulses of the ASL due to the saturation of

Table 5.2: Simulated optimal timing and signal intensities at the beginning of both ASL and BOLD acquisitions for 0–3 background suppression pulses without and with in-plane pre- and post-saturation of imaging slice's magnetisation at 3 T.

Without Pre- and Post-Saturation									
No. of BS Pulses	Inversion Times [ms]	Simulated ASL control signal (1 st acquisition, 1 st slice)				Simulated BOLD signal (2 nd acquisition, 1 st slice)			
		White	Grey	Blood	CSF	White	Grey	Blood	CSF
0	–	0.797	0.612	0.532	0.271	0.722	0.545	0.472	0.242
1	TI ₁ =1008	0.162	0.050	0.026	-0.007	0.722	0.545	0.472	0.242
2	TI ₁ =719 TI ₂ =508	0.117	0.074	0.060	0.024	0.722	0.545	0.472	0.242
3	TI ₁ =409 TI ₂ =323 TI ₃ =443	0.118	0.073	0.063	0.036	0.722	0.545	0.472	0.242
With Pre- and Post-Saturation									
No. of BS Pulses	Inversion Times [ms]	Simulated ASL control signal (1 st acquisition, 1 st slice)				Simulated BOLD signal (2 nd acquisition, 1 st slice)			
		White	Grey	Blood	CSF	White	Grey	Blood	CSF
0	–	0.856	0.696	0.620	0.342	0.722	0.545	0.472	0.242
1	TI ₁ =936	0.192	0.037	0.000	-0.045	0.722	0.545	0.472	0.242
2	TI ₁ =492 TI ₂ =664	0.118	0.073	0.063	0.035	0.722	0.545	0.472	0.242
3	TI ₁ =98 TI ₂ =504 TI ₃ =565	0.118	0.074	0.062	0.032	0.722	0.545	0.472	0.242

the longitudinal signal by the 90° readout pulse. To assess the BOLD signal of DABS compared to traditional FAIR, the longitudinal magnitude of the non-background suppressed ASL signal should be compared with the BOLD signal of the second acquisition, as normally BOLD information is extracted from the high CNR ASL data. This can be seen to be of comparable order. However, DABS has the added advantage that echoes can be obtained for each acquisition at times optimised to ASL (shortest TE) and BOLD ($TE \approx T_2^*$) sensitivity. This will significantly increase SNR for ASL data, for example a TE of 15 ms is achievable at 3 T but 35 ms is the optimal TE for BOLD. SNR will be increased by a factor of 2 for DABS, where we can acquire data with $TE = 15$ ms rather than 35 ms.

Figure 5.10 shows the longitudinal magnetisation for white and grey mat-

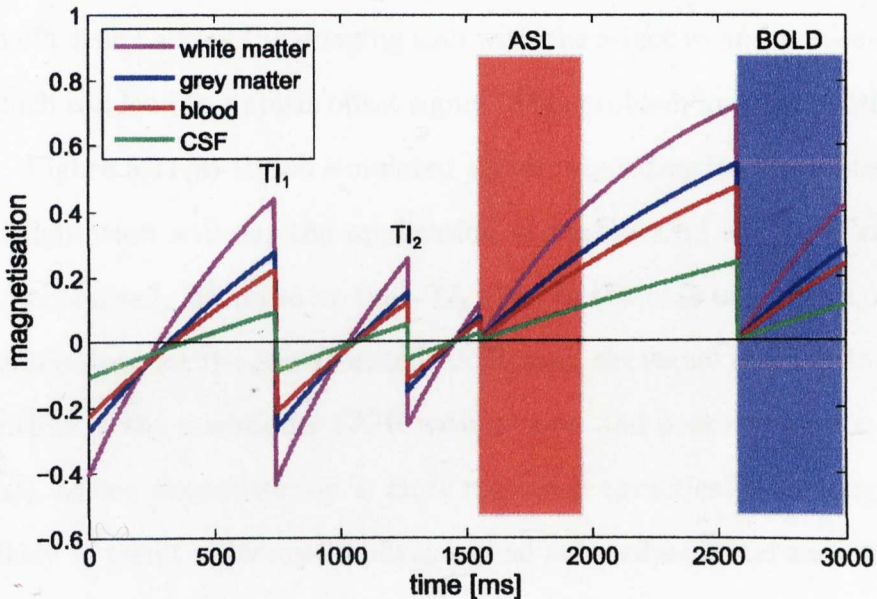


Figure 5.10: Simulated normalised inversion recovery signals of the longitudinal magnetisations for various brain tissues (white matter, grey matter, blood, and CSF) at 3 T with two BS pulses applied at times TI_1 and TI_2 times (719 and 508 ms, respectively). Red and blue blocks indicate a 7-slice ASL and BOLD acquisitions, respectively. The initial value of the longitudinal magnetisation is presented for a TR of 3 s as used experimentally for optimal SNR per unit time, whilst allowing good labelling.

ter, blood and CSF, with application of two background suppression pulses at the optimal timings. As shown, the addition of a second inversion pulse improves the nulling across all the brain tissue type signals. Table 5.2 provides the optimal timing for two and three background suppression pulses and the associated tissue signals. All simulations assume 100 % efficiency of inversion pulses with no loss or decay of signal. No gains in suppression were found for three pulses, and this configuration is likely to lead to reduction of the perfusion signal due to imperfections in inversion pulses profiles.

(B) Double Acquisition FAIR with Presaturation Pulses By introducing pre- and post-saturation pulses, the static signal for all tissue types is initially saturated, meaning, the longitudinal magnetisation is zero (for all brain tissues). This technique has the advantages of overcoming inaccuracies in inversion efficiency across the imaging slab with the selective and non-selective pulses which can lead to a static offset signal. This problem increases with field strength. Figure 5.11(a) shows simulated signal intensities for a presaturated FAIR configuration without the application of background suppression, and with one, optimised, BS pulse at time TI_1 (b). In the case of no background suppression pulses, for the presaturated FAIR case, the signal at $TI = 1550$ ms is higher than in the traditional FAIR without pre- and post -saturation (Figure 5.9(a)), as the magnetisation is more recovered (practically for long TR). This is likely to result in increased physiological noise effects (and an increased contribution from the Roman Artefact for 7 T data). Applying just one BS pulse (Fig. 5.11(b)) results in the signals across all brain tissues being scattered at the desired null point.

Figure 5.12 shows the evolution of simulated longitudinal magnetisation signals for white and grey matter, blood and CBF using in-plane pre- and post-saturated for two optimised background suppression pulses. The optimal

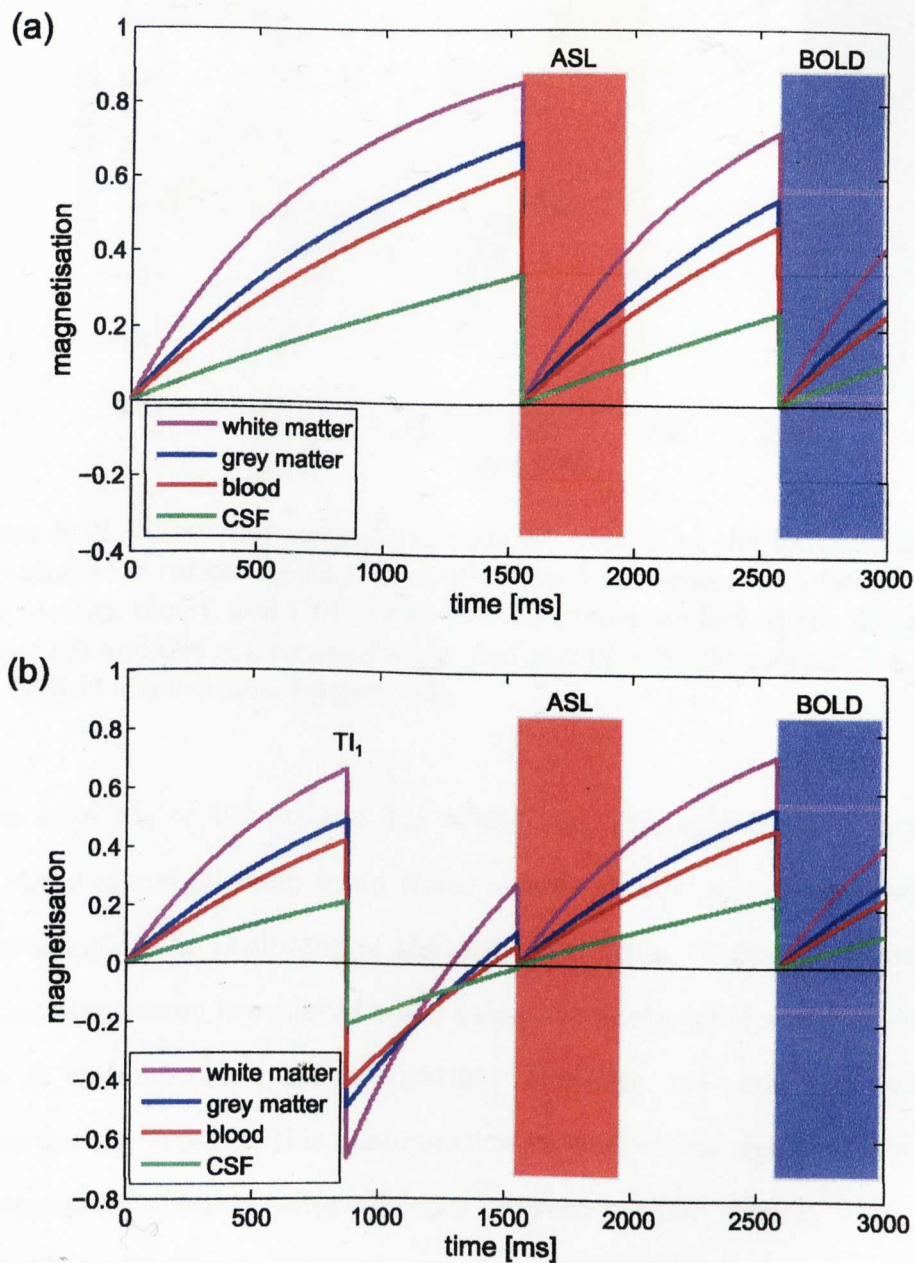


Figure 5.11: Simulated normalised recovery signals of the longitudinal magnetisation for pre- | post-saturated brain tissues (white matter, grey matter, blood, and CSF) at 3 T without background suppression (a) and with one BS pulse applied at the optimal time $T_{I_1} = 936$ ms (b). Red and blue blocks indicate 7-slice ASL and BOLD acquisitions, respectively.

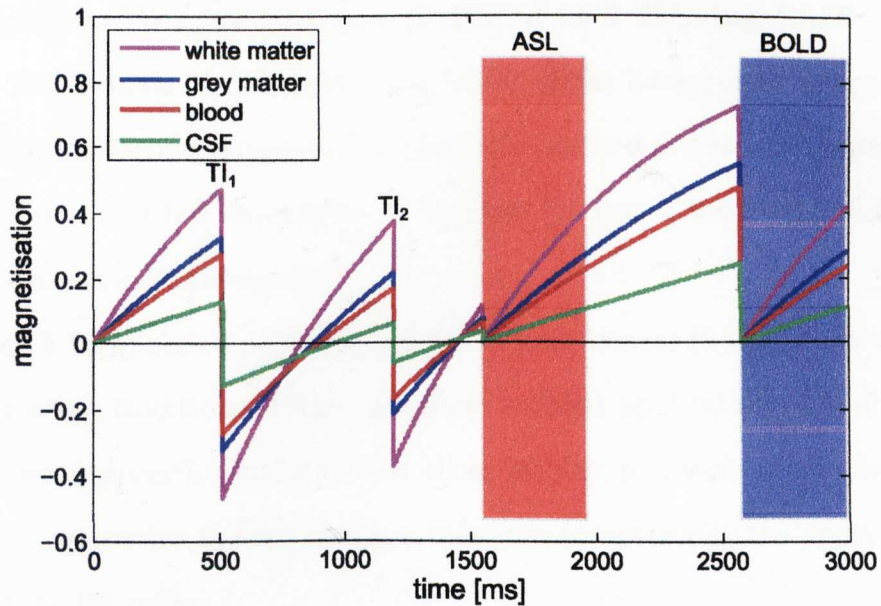


Figure 5.12: Simulated normalised recovery signals of the longitudinal magnetisations for various brain tissues with pre- | post-saturation (white matter, grey matter, blood, and CSF) with two BS pulses applied at the T_{I1} and T_{I2} times (492 and 664 ms, respectively). Red and blue blocks indicate 7-slice ASL and BOLD acquisitions, respectively.

times were $T_{I1} = 492$ ms and $T_{I2} = 664$ ms. This configuration suppresses the signal across all main brain tissue signals at 1450 ms, giving the desired suppression at the beginning of the ASL acquisition. Table 5.2 shows that a similar suppression is achieved when using two background suppression pulses with or without pre- | post-saturation. However, pre- and post-saturation pulses are preferred as this configuration reduces static signal offsets due to differences in inversion pulse efficiency between tag and control.

Again optimisation using three pulses shows very little improvement in introducing additional pulses in terms of static signal suppression, and because of imperfect profiles, increased number of pulses would only contribute to further discrepancies between the simulation and experimental ASL images. The signal in the second stack (BOLD acquisition) remains the same for all considered approaches.

(C) Perfusion-Weighted Images Acquired at 3 T Using FAIR Technique: BS Width Validation The width of the background suppression pulses is an important parameter in using this method due to flow dependent effects. Here are a few approaches to validate the use of the inversion pulses to suppress static tissue signal.

Figure 5.13(a) shows perfusion-weighted brain images (5 transverse slices) obtained using traditional FAIR technique without application of additional background suppression pulses. The slices display perfusion of the labelled blood to grey matter tissue. This is a reference to determine the appropriate width of the BS pulses.

Figure 5.13(b) displays perfusion-weighted brain images obtained using

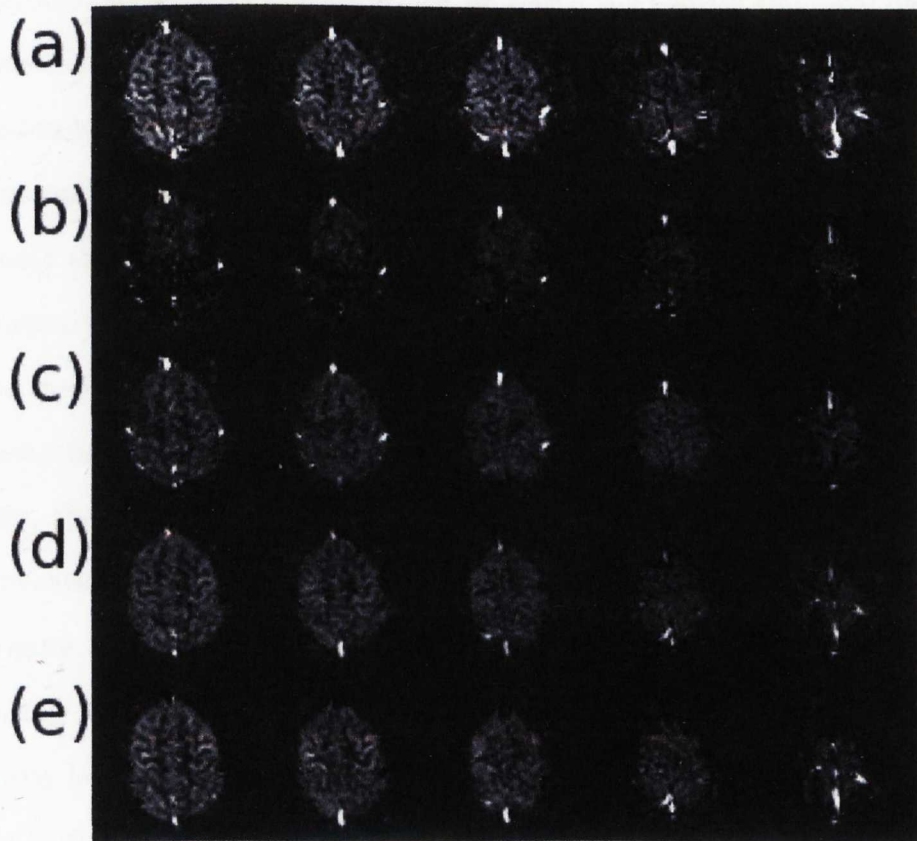


Figure 5.13: Perfusion-weighted images acquired at 3 T using traditional FAIR technique (a) and with application of two background suppression pulses ($TI_1 = 507$ ms and $TI_2 = 688$ ms) with various spatial widths: 35 mm (b), 60 mm (c), 100 mm (d), and 200 mm (e).

FAIR with additional application of two background suppression pulses. The width of the introduced BS pulses (at $TI_1 = 507$ ms and $TI_2 = 688$ ms) was set to match the width of the selective FAIR pulse – 35 mm. As shown in Figure 5.13(b), this significantly reduces perfusion signal in each of the acquired slices. A narrow second BS pulse applied to the imaging slab leads to both the selective and non-selective pulses being flow sensitive but ultimately, sensitivity to perfusion signal is suppressed. This is due to fast flowing blood appearing to have an opposite sign of signal change to slow moving blood.

Increasing the width of the background suppression pulses make the sequence more sensitive to perfusion, as shown in Figure 5.13(c) and (d), as more of the moving blood has the same sign of the changes. If we increase the background suppression pulses' width to match the control slab, 200 mm, the sequence is then most sensitive to qualitative perfusion. Figure 5.13(e) displays perfusion-weighted images of five transverse slices of human brain, using two background suppression pulses of 200 mm. Grey matter perfusion is clearly visible with the Contrast-to-Noise Ratio (CNR) comparable to traditional FAIR technique without suppressing the static tissue signal (Fig. 5.13(a)). Grey matter perfusion of the BS data yields approximately 15 % reduction in signal intensity across the whole head, compared to traditional FAIR acquisition. It is wise, though, to optimise the second background suppression pulse, as its minimisation ensures inflow of fresh blood in the next TR period.

Figure 5.14 shows the effect of the background suppression pulses on the inflowing blood for tag and control conditions. The difference in the signal intensity between the tag and control at the beginning of the ASL acquisition is the basis of the ASL methodology.

The background suppression method was shown to have no significant disadvantages on qualitative perfusion over the traditional FAIR acquisition technique.

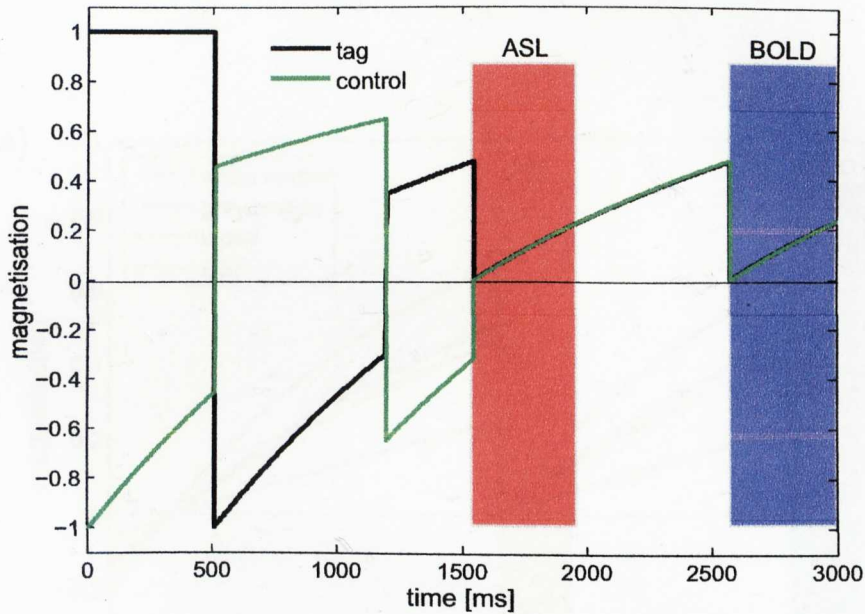


Figure 5.14: Simulation of magnetisation for DABS (with 2 BS pulses) acquisition for the inflowing blood in tag (black) and control (green) conditions at 3 T.

5.2.1.2 7 T Optimisation

The methods described in Section 5.2.1.1 were then repeated at 7 T. Because of the lengthened relaxation times, the potentially reduced inversion efficiency at 7 T, and the use of magnitude subtraction, the null point for the simulation was chosen to be 200 ms prior to the beginning of the first (ASL) acquisition block/stack ($T_{\text{null}} = 1350$ ms) for a label delay $TI = 1550$ ms. This ensured that the grey and white matter (dominant tissues of the imaging slice) were past the null point at the label delay TI . The equivalent simulations, described above for 3 T, were performed for BS optimisations using parameter values for 7 T provided in Table 5.1.

(A) Double Acquisition FAIR, No Presaturation Module Again, without additional pulses, longitudinal magnetisation signal values at the beginning of the first acquisition at $TI = 1500$ ms (Fig. 5.15(a)) are highly recovered. By introducing one additional inversion pulse (one BS) at an optimal time, shown

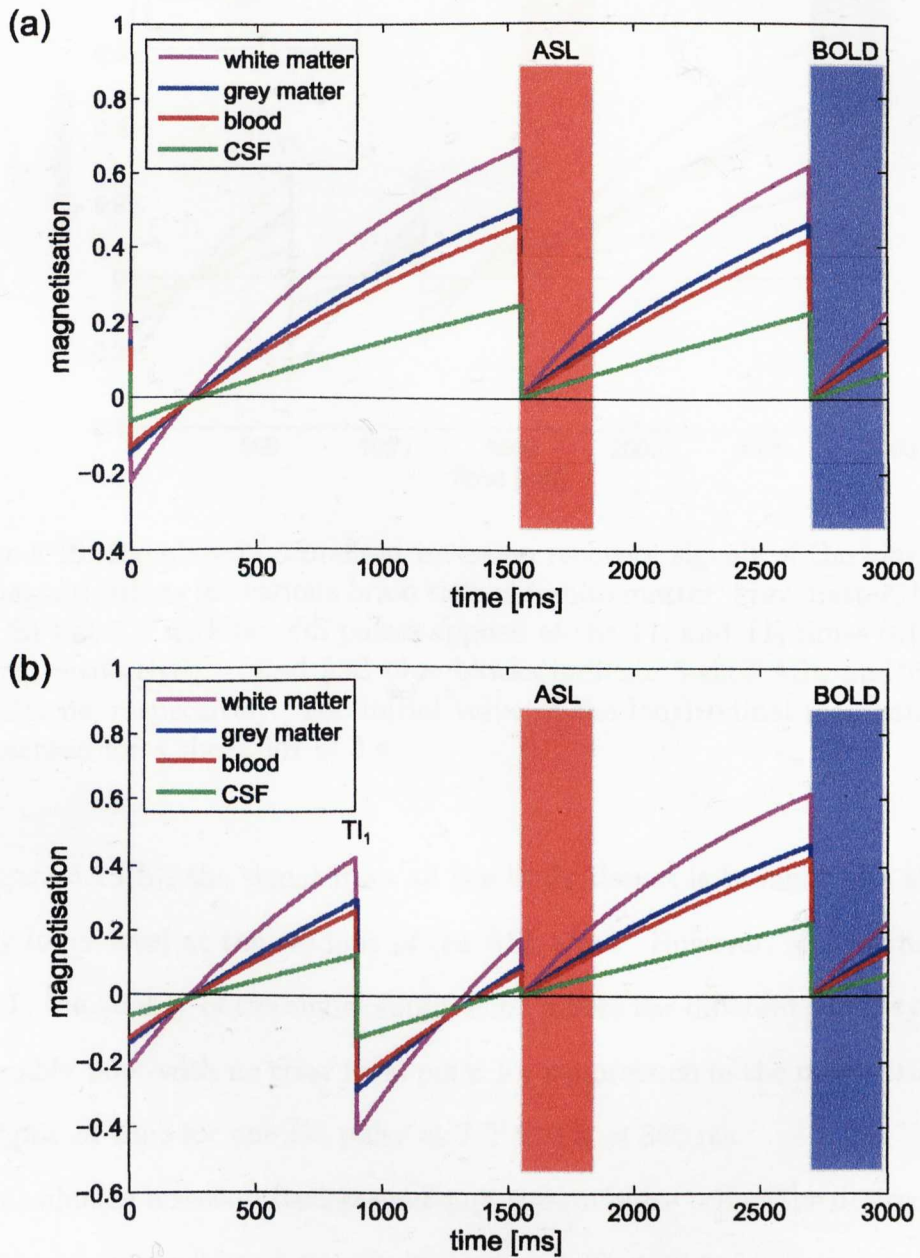


Figure 5.15: Simulated normalised inversion recovery signals of the longitudinal magnetisation for various brain tissues (white matter, grey matter, blood, and CSF) at 7 T without background suppression pulses (a) and with one BS pulse (b) applied at the T_{I1} time. Red and blue blocks indicate 5-slice ASL and BOLD acquisitions, respectively. The initial value of the longitudinal magnetisation is presented for a short TR of 3 s.

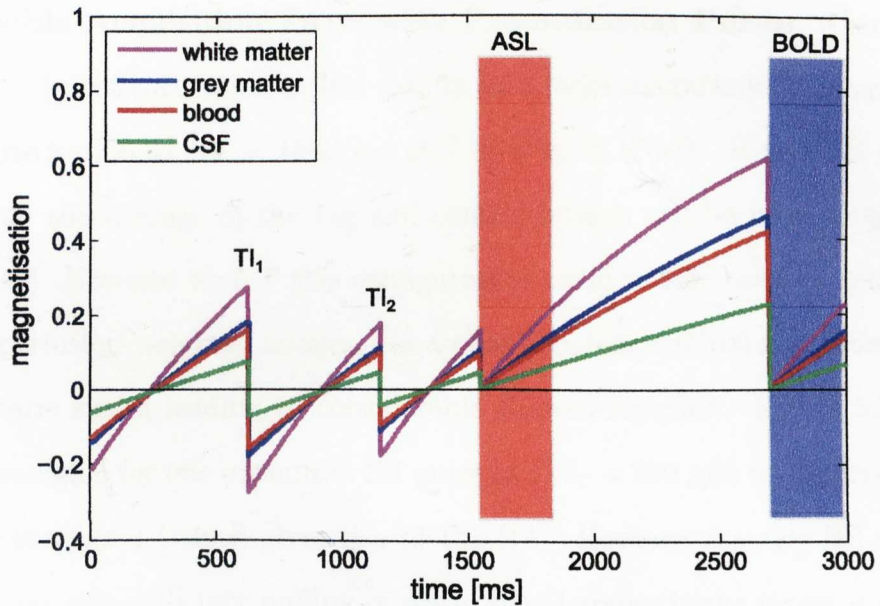


Figure 5.16: Simulated normalised inversion recovery signals of the longitudinal magnetisations for various brain tissues (white matter, grey matter, blood, and CSF) at 7 T with two BS pulses applied at the TI_1 and TI_2 times (611 and 505 ms, respectively). Red and blue blocks indicate 5-slice ASL and BOLD acquisitions, respectively. The initial value of the longitudinal magnetisation is presented for a short TR of 3 s.

in Figure 5.15(b), the signal from all the brain tissues is brought to a significantly lower level at the readout of the ASL stack. However, as was the case for 3 T, the quality of the signal suppression across the different tissue types is reasonably poor with no clear focal point for suppression of the magnetisation. The optimal time for one BS pulse at 7 T is $TI_1 = 880$ ms.

Introducing a second background suppression pulse brings the desired suppression of all considered signals of normal brain tissues, as found at lower magnetic field. Figure 5.16 shows the relaxation of the magnetisation signals for two optimised background suppression pulses: first at $TI_1 = 611$ ms and the second 505 ms later (TI_2). This simulation resulted in low, but positive signals at the ASL acquisition for white and grey matter, blood and CSF.

(B) Double Acquisition FAIR with Presaturation Pulses Using in-plane pre- | post-saturation pulses results in a large magnitude of longitudinal magnetisation at $TI = 1550$ ms at 7 T (Fig. 5.17(a)). If the $TE \sim T_2^*$ (≈ 25 ms) the average of the tag and control images can be used to obtain BOLD [46]. However at 7 T this configuration could not be used to generate reliable perfusion-weighted images, due to the high longitudinal magnetisation of the static signal leading to considerable Roman Artefact. Figure 5.17(b) shows the signal for one optimised BS pulse at ($TI_1 = 800$ ms) to suppress the static tissue signal (which gives rise to the RA). However a single BS pulse, does not provide sufficient nulling of static signal across tissue types, a result previously demonstrated for 3 T.

By applying in-plane pre- and post-saturation pulses and two additional background suppression pulses, the most desirable longitudinal magnetisation of the image slab is obtained. As shown in Figure 5.18, there is a clear nulling of all tissue types (Table 5.3) with two BS pulses at 403 (TI_1) and 638 ms (TI_2). Table 5.3 shows simulated normalised longitudinal signals for the DABS sequence with and without saturation at 7 T. At 7 T, it can be seen there is $\approx 80\%$ signal reduction for the ASL acquisition for all tissues using DABS in relation to traditional FAIR technique (no background suppression pulses). However, the use of pre- and post-saturation pulses is highly necessary at ultra high field [81], because profiles of the selective and non-selective inversion can be poor, and due to the RA in addition to the likelihood that static offset signal is large at 7 T.

The use of three BS pulses (Table 5.3) is presented to show very little improvement in introducing additional pulses, which in practice would be worse because of the imperfect inversion pulse profiles at 7 T.

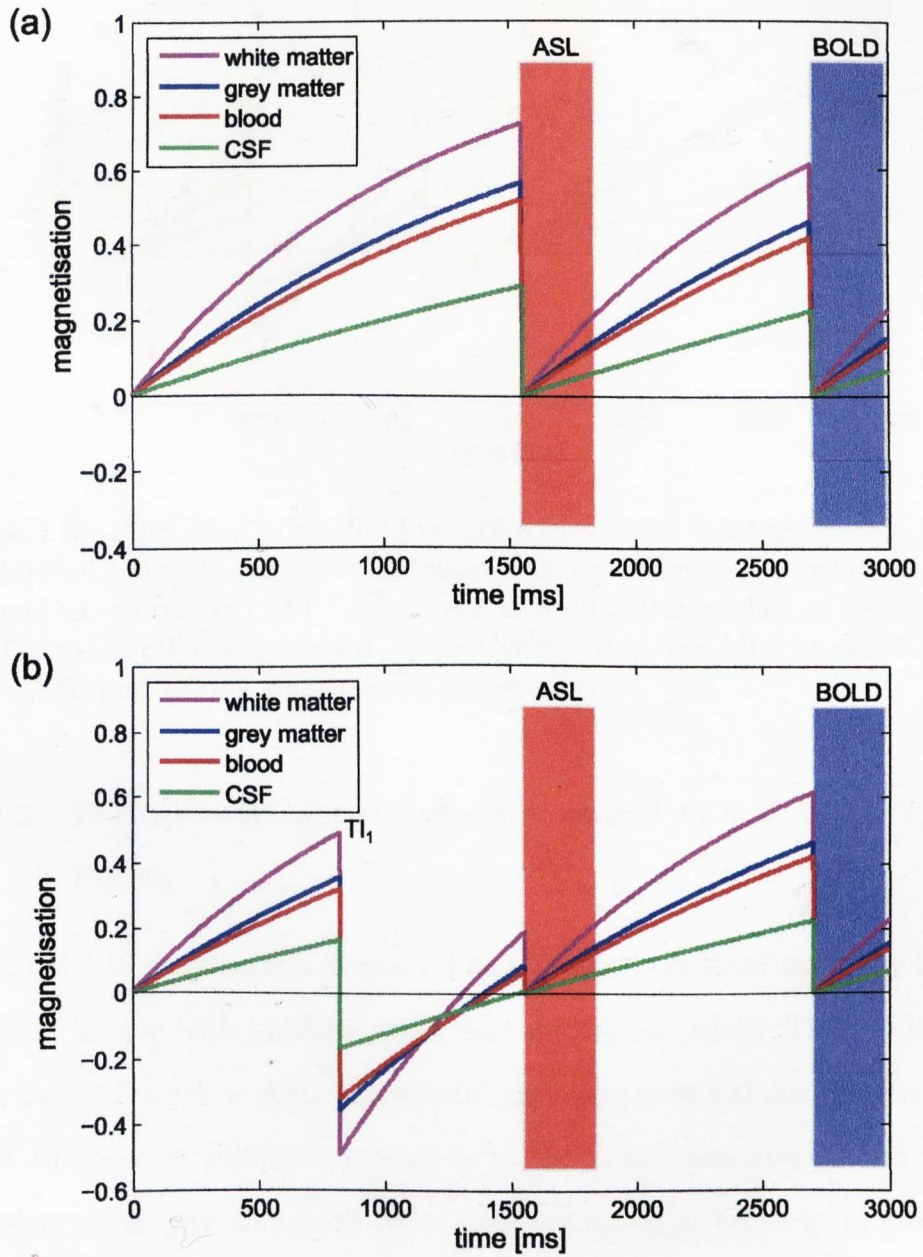


Figure 5.17: Simulated normalised saturated inversion recovery signals of the longitudinal magnetisation in the image slab for brain tissue (white matter, grey matter, blood, and CSF) at 7 T without background suppression pulses (a) and with one BS pulse applied at optimal time $T_{I1} = 800$ ms (b). Red and blue blocks indicate 5-slice ASL and BOLD acquisitions, respectively.

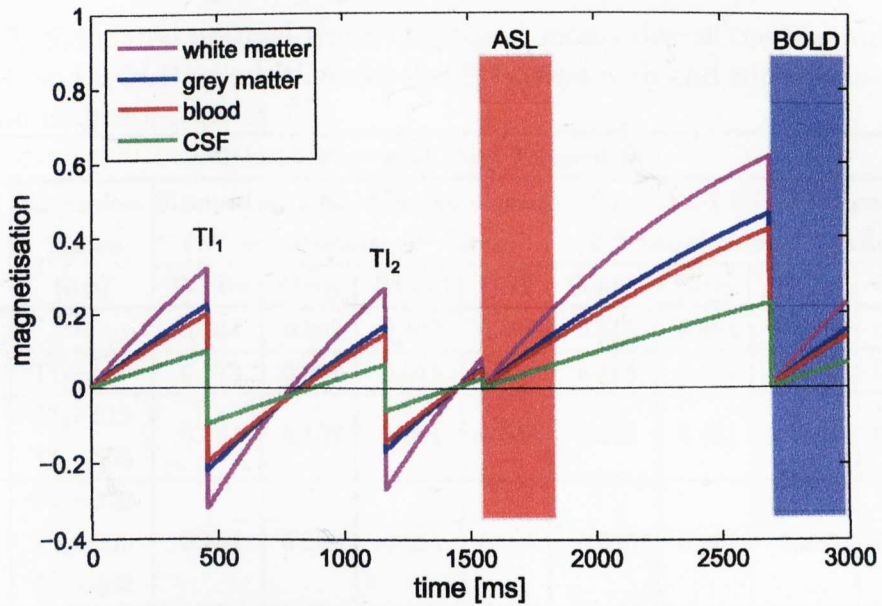


Figure 5.18: Simulated normalised saturated inversion recovery signals of the longitudinal magnetisation in the image slab for brain tissue (white matter, grey matter, blood, and CSF) at 7 T with two BS pulses applied at optimal T_{I1} and T_{I2} times (403 and 638 ms, respectively). Red and blue blocks indicate 5-slice ASL and BOLD acquisitions, respectively.

5.2.1.3 Perfusion-Weighted Images Acquired at 7 T Using FAIR-DABS

Figure 5.19 displays two 5-slice volumes (stacks) obtained using the FAIR-DABS technique with in-plane pre- | post-saturation pulses. The top images show the first stack – ASL acquisition with suppressed static tissue signal, whilst the bottom volume corresponds to the BOLD-sensitive second stack. For comparison with simulated data, the average signal intensity in grey and white matter measured from small regions of interest (ROI of 30 to 15 voxels for 1st to 5th slice, four separate regions across the transverse plane) was estimated as a ratio with base data of two-stack acquisition with no BS and long TR. The BS pulses reduce the signal intensity in comparison with a non-background suppressed FAIR acquisition and the reduction of the ASL data is about 78 % in the first slice and 60 % in the last slice for both grey and white matter,

Table 5.3: Simulated optimal times and signal intensities at the beginning of both ASL and BOLD acquisitions for 0–3 BS pulses with and without in-plane saturation magnetisation at 7 T.

Without Pre- and Post-Saturation									
No. of BS Pulses	Inversion Times [ms]	Simulated ASL control signal (1 st acquisition, 1 st slice)				Simulated BOLD signal (2 nd acquisition, 1 st slice)			
		White	Grey	Blood	CSF	White	Grey	Blood	CSF
0	–	0.664	0.502	0.457	0.245	0.615	0.461	0.420	0.225
1	TI ₁ =880	0.173	0.091	0.075	0.024	0.615	0.461	0.420	0.225
2	TI ₁ =611 TI ₂ =505	0.154	0.102	0.091	0.043	0.615	0.461	0.420	0.225
3	TI ₁ =372 TI ₂ =306 TI ₃ =402	0.154	0.102	0.091	0.046	0.615	0.461	0.420	0.225
With Pre- and Post-Saturation									
No. of BS Pulses	Inversion Times [ms]	Simulated ASL control signal (1 st acquisition, 1 st slice)				Simulated BOLD signal (2 nd acquisition, 1 st slice)			
		White	Grey	Blood	CSF	White	Grey	Blood	CSF
0	–	0.725	0.567	0.522	0.291	0.615	0.461	0.420	0.225
1	TI ₁ =800	0.187	0.085	0.066	0.008	0.615	0.461	0.420	0.225
2	TI ₁ =403 TI ₂ =638	0.154	0.102	0.091	0.046	0.615	0.461	0.420	0.225
3	TI ₁ =194 TI ₂ =476 TI ₃ =411	0.154	0.102	0.091	0.044	0.615	0.461	0.420	0.225

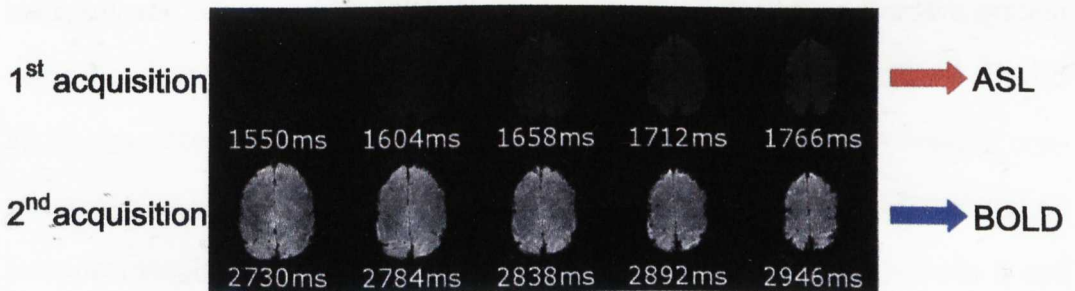


Figure 5.19: 5-slice DABS data obtained at 7 T; first stack corresponds to ASL data (static tissue signal is suppressed) and second to the recovered signals to maximise the BOLD effect. Images acquired at high resolution ($1.5 \times 1.5 \times 3 \text{ mm}^3$), $TE \sim T_2^*$ (26 ms).

whilst the BOLD data has only an 8 and 4 % reduction for the first and last slice, respectively. Theoretical reduction of the first slice yields about 80 % for ASL, which is very close to the experimental data, and the signal in the second stack should remain the same, as it follows the suppression of the 90° ASL readout pulses. The discrepancies in signal reduction between the theoretical and experimental data is generally due to the imperfect inversion pulses, showing clearly in the high-signal images, however, the non-ideal 90° pulses also contribute to the differences in BOLD-based data.

5.2.2 Assessing Advantages of DABS to fMRI Studies

The aim of this study was to assess the advantages of the DABS sequence, which incorporates background suppressed ASL and high-contrast BOLD data to a functional paradigm. The study was approved by the local ethics committee and four healthy adult subjects (average age 27.5 ± 1 year) were scanned; all volunteers gave informed, written consent.

5.2.2.1 Method

Experiments were performed on a 3 T Philips Achieva scanner using a body transmit and 8-channel SENSE receive coil, and a 7 T Philips Achieva system using head volume transmit and 16-channel SENSE receive coil. A DABS FAIR sequence (using in-plane pre- | post-saturation and spatially limited non-selective slab confined to 200 mm to allow a short TR acquisition [91] for good temporal resolution of the functional study) was implemented on both 3 and 7 T using two background suppression pulses, optimised as described above. At 3 T, data were also collected in the absence of background suppression pulses (DA-noBS). Due to the Roman Artefact, this data could not be collected at 7 T.

For each, in-plane saturation was provided by WET pre- and sinc post-

saturation pulses [46]. Images were acquired using SENSE factor 2, at two spatial resolutions:

- 3 T data:

- $3 \times 3 \times 5 \text{ mm}^3$ (3 T Lo-Res); ASL $TE_1 = 12 \text{ ms}$, BOLD $TE_2 = 35 \text{ ms}$
- 3 mm isotropic (3 T Hi-Res); ASL $TE_1 = 12 \text{ ms}$, BOLD $TE_2 = 35 \text{ ms}$

- 7 T data:

- 3 mm isotropic (7 T Lo-Res); ASL $TE_1 = 9 \text{ ms}$, BOLD $TE_2 = 26 \text{ ms}$
- $1.5 \times 1.5 \times 3 \text{ mm}^3$ (7 T Hi-Res); $TE = 26 \text{ ms}$.

7 and 5 contiguous slices at 3 and 7 T, respectively, were acquired per volume ($N = 90$ volumes, 15 cycles) in ascending order with minimal temporal spacing (total acquisition time of 427 ms and 270 ms at 3 and 7 T, respectively). The functional paradigm consisted of one handed, sequential finger tapping with 12 s duration (ON period) and 24 s resting state (OFF period).

Physiological data, respiration and cardiac pulsation, were monitored and recorded using a pulse oximeter and respiratory transducer with a temporal resolution of 500 Hz. Following the functional experiment, a non-prepared base M_0 reference EPI image was also collected along with a series of inversion recovery EPI (IR-EPI) measurements ($TI = 200 - 1400 \text{ ms}$ in 200 ms steps, and 1700, 2000, 3000 and 4000 ms; $TR = 15 \text{ s}$) to allow measurement of tissue T_1 maps.

5.2.2.2 Image Analysis

One aim was to assess the success of realignment of the background suppressed data. If the static tissue signal is very close to zero, the realignment process is challenging. However, use of the DABS technique can overcome this as the second stack (BOLD) contains images of high SNR (collected after

the ASL data). These BOLD images can be used for realignment and their transforms then applied to background suppressed ASL data. To assess this, the tag and control ASL image time series were realigned using a standard algorithm in SPM (with a 5 mm FWHM Gaussian smoothing kernel and 2nd Degree B-Spline interpolation) based on two methods:

- (I) realignment of the background-suppressed ASL acquisition, which had very low signal
- (II) realignment of the second BOLD acquisition and application of the transforms to the first background suppresses ASL acquisition.

A second aim was to assess the contribution of physiological noise to ASL and BOLD data. Therefore, the effect of correcting DABS ASL and BOLD data sets for physiological noise using RETROICOR [83], was assessed and compared to the (DA-noBS) data. RETROICOR uses recorded respiratory and cardiac waveforms to remove the physiological contribution of both sources from the images. Those voxels, which are modulated at the affected frequencies, are then corrected. Respiratory and cardiac contribution for each ASL and BOLD data sets can be obtained as physiological parameter maps.

To then assess the use of DABS for the functional study, ASL and BOLD activation maps were obtained using standard SPM algorithms with: $p < 0.005$ for CBF and $p < 0.001$ for BOLD with Family-Wise Error (FWE) correction for BOLD. t-scores and cluster sizes of activated areas were compared between methods.

5.2.2.3 Results

(A) Realignment Figure 5.20 shows realignment parameters plots of the ASL and corresponding BOLD data for a DABS acquisition at 3 and 7 T. The translation and rotation parameters for ASL (realignment) data (method

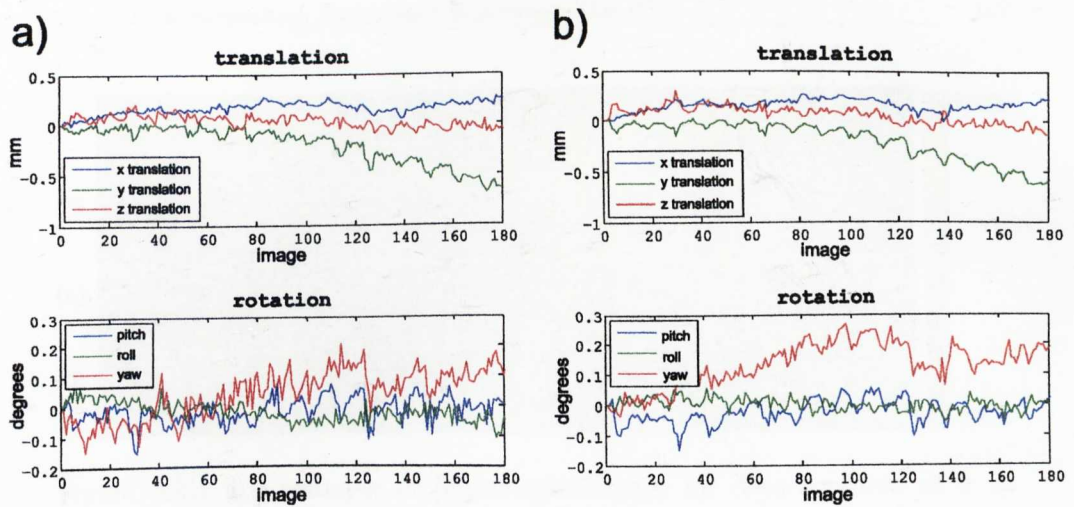


Figure 5.20: Realignment parameter plots for the first ASL stack (a) and the second BOLD stack (b) collected using DABS sequence.

(I), Fig. 5.20(a)) are significantly more erratic than the corresponding BOLD data. This is probably due to the low image intensity of the BS ASL data and also due to the fact that there is a significant difference in tag and control images of the ASL acquisition series. The BOLD data (Fig. 5.20(b)) shows motion parameters with fewer sharp transforms whilst maintaining a similar shape of translational and rotational curves. For subsequent analysis, method (II) of realigning the second stack BOLD acquisition and applying realignment parameters to the first ASL acquisition stack, was used.

(B) Physiological Noise: Background Suppression vs. RETROICOR
 ASL and BOLD data for DABS and Double Acquisition without Background Suppression (DA-noBS) were analysed. Using RETROICOR, cardiac and respiratory maps were formed for each. Figure 5.21 shows typical maps of cardiac and respiratory motion contribution to the image. The ASL data (a) and (c) can be seen to show reduced physiological noise contribution compared to more recovered BOLD acquisition (b) and (d).

The ASL and BOLD time-series were processed in SPM5 to identify acti-

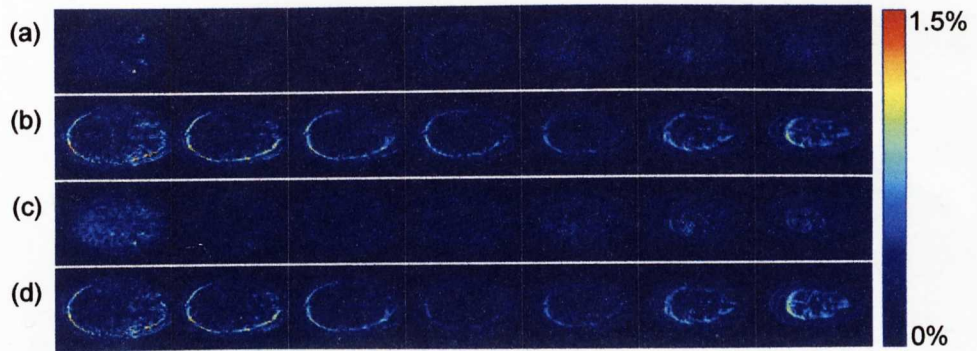


Figure 5.21: An example of physiological maps for data acquired at 3 T. Respiratory maps for DABS ASL (a) and BOLD stack (b) and cardiac maps for DABS ASL (c) and BOLD stack (d). Courtesy of Emma Hall.

vated areas for both data with and without RETRICOR correction. For all data sets a general linear model was formed and activated maps calculated at $p < 0.005$ for CBF and $p < 0.001$ with FWE (Family Wise Error) correction for BOLD.

For validation, standard FAIR with two data stacks (DA-noBS) was also acquired with both CBF and BOLD maps created from the first stack. 3 T data sets (FAIR-DABS and FAIR-DA-noBS) were analysed both with and without RETROICOR data correction. The number of activated voxels, time-courses of their mean and maximum t-values obtained for each set were estimated. Figure 5.22 displays a comparison of the functional analysis of the CBF data acquired using FAIR-DABS (a) and with RETROICOR applied to the data (b). The application of RETROICOR to BS ASL data reduces the size of the activated cluster by over 50 % with only a small reduction in t-score. The small difference in t-value can be explained by similar time-courses of the average intensity of the activated clusters (Fig. 5.22(c)) of both data sets. Therefore, RETROICOR introduces additional smoothing, which results in the loss of activation-sensitive voxels; RETROICOR reduces the functional response of the ASL data obtained using the background suppression method.

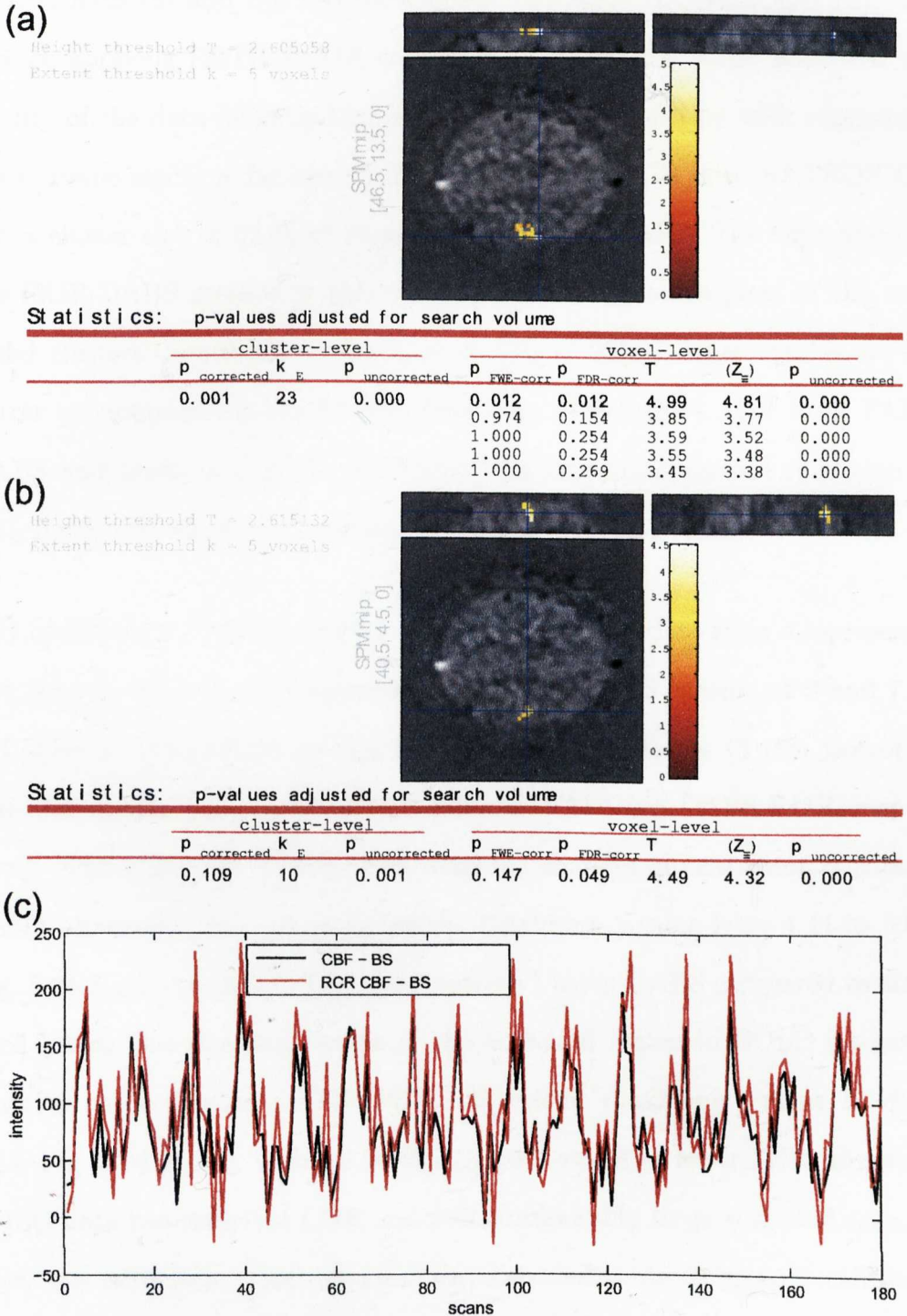


Figure 5.22: Comparison of the activation maps at 3 T obtained with suppressed static tissue signal (a), with applied RETROICOR correction of physiological noise (b), and corresponding time courses (c).

Figure 5.23 displays the functional analysis of the CBF data acquired using FAIR-DABS (a) and the FAIR-DA-noBS data after RETROICOR (b). Although applying RETROICOR correction to traditional FAIR improved the quality of the data (slightly higher t-score), data acquisition with suppressed static tissue signal is far more efficient. Standard FAIR with RETROICOR has a cluster size of 52 % of that found for FAIR-DABS. The supremacy of the FAIR-DABS method is also shown in the time course plots of the activated clusters' intensities for both cases (Fig. 5.23(c)), where cycles are far better pronounced for the FAIR-DABS data (black line). For both FAIR-DABS and traditional FAIR, RETROICOR correction showed reduction in ASL functional response compared to realigned FAIR-DABS.

(C) Statistical Results, fMRI Figure 5.24 shows data from a representative subject showing the implementation of the DABS scheme at 3 and 7 T. 3 T data in Figure 5.24(A) and 5.24(B) compares Hi-Res (3 mm isotropic) activation for data acquired using traditional FAIR and DABS FAIR, respectively. The sensitivity to perfusion weighted changes on activation is considerably increased (from 14 to 42 voxels, maximum t-value from 4.44 to 5.80, Fig. 5.24 A_{ASL} versus 5.24 B_{ASL}, respectively) using DABS compared to standard FAIR. The size and t-score of the activated region in BOLD images is however reduced using DABS (192 to 43 voxels, maximum t-value 13.16 to 8.84, Fig. 5.24 A_{BOLD} versus 5.24 B_{BOLD}) as a result of lower SNR. However, BOLD data has sufficient CNR and still considerably large activated area, to allow this reduction. This reduction can also contribute to better localisation of BOLD contrast, by limiting naturally to voxels with only highest significance. Figure 5.24(C) and 5.24(D) shows 7 T DABS data collected at Lo-Res (3mm isotropic) and Hi-Res (1.5 mm in-plane) resolution. Since 7 T offers increased SNR and lengthened relaxation times, ASL CNR is increased. At

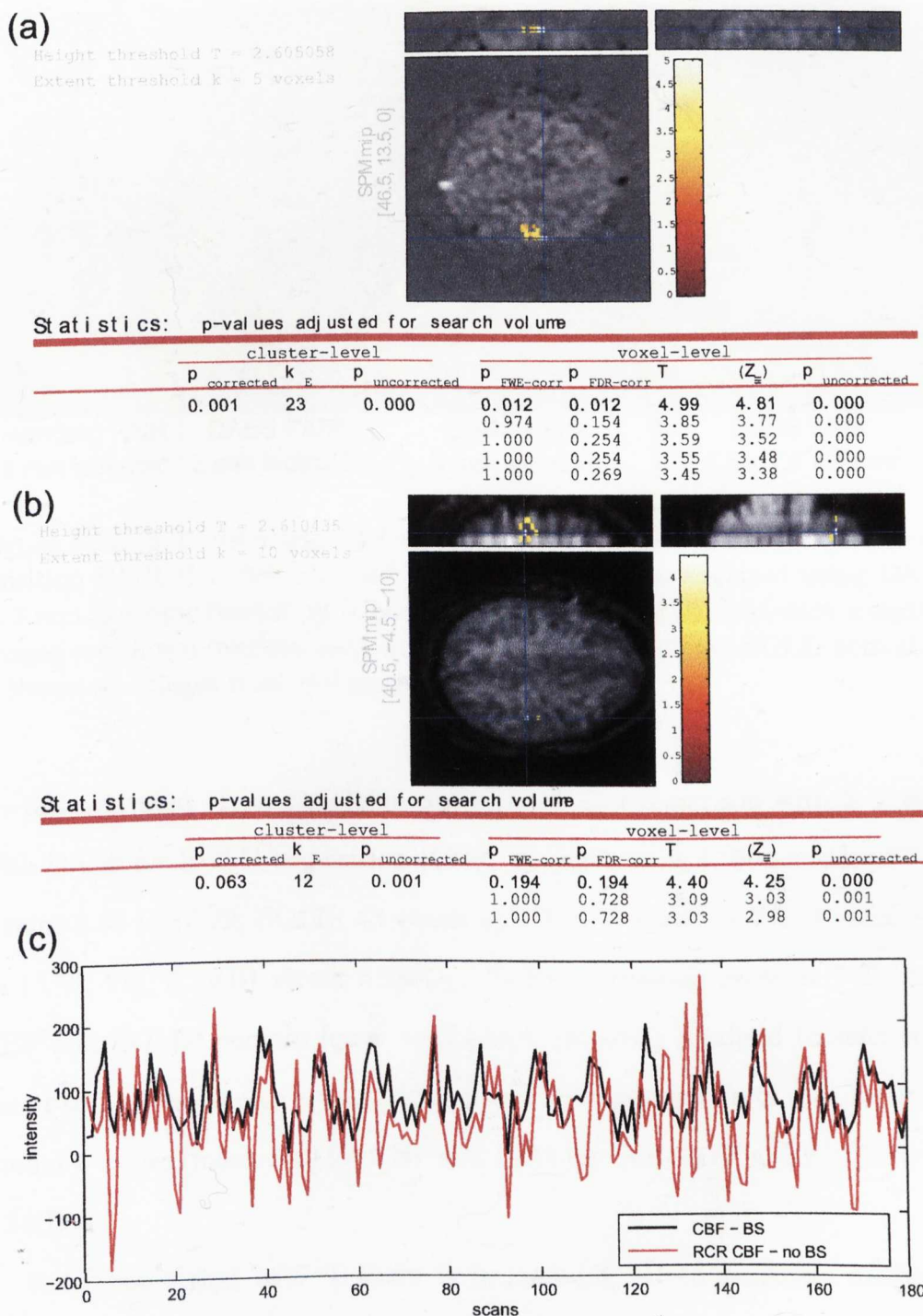


Figure 5.23: Comparison of the activation maps at 3 T obtained with suppressed static tissue signal (a), without background suppression and applied RETROICOR (b), and corresponding time courses (c).

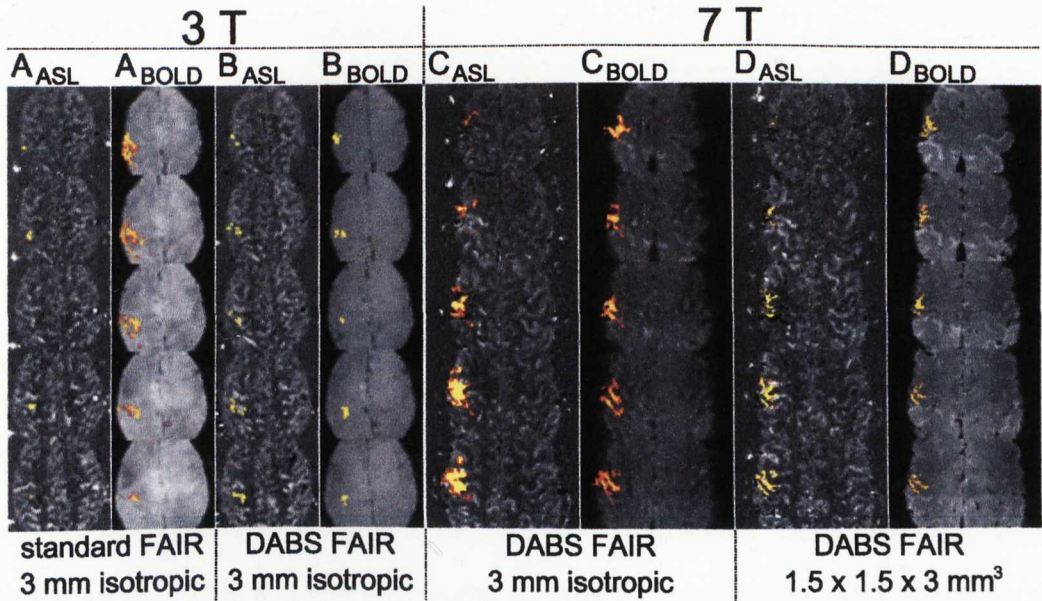


Figure 5.24: 3 T: data acquired at 3 mm isotropic resolution for double acquisition FAIR (No BS) (A) and DABS (B); 7T: data acquired using DABS at 3 mm isotropic resolution (C) and $1.5 \times 1.5 \times 3 \text{ mm}^3$ (D). Perfusion weighted images are shown overlaid with activated perfusion regions, BOLD activation is shown on images from the second acquisition.

Lo-Res activated areas are significantly larger in comparison with 3 T even with DABS for BOLD acquisition (CBF: 42 voxels at 3 T, 592 voxels at 7 T; t -value 5.80 to 10.29; BOLD: 43 voxels at 3 T, 534 voxels at 7 T, t -value 8.84 to 14.32, Fig. 5.24(B) versus 5.24(C)). Hi-Res activation areas at 7 T (both CBF and BOLD) contain fewer voxels but are better localised to sulci compared to Lo-Res, due to a reduction of partial voluming effects, but maintain similar t -values (mean 8.49 for CBF and 12.11 for BOLD) (Fig. 5.24(C) versus 5.24(D)).

It is shown that at 7 T there is increased CNR to perfusion measures allowing higher resolution studies with reduced partial volume effects. The FAIR DABS sequence provides a double acquisition method for simultaneous acquisition of BOLD and background suppressed CBF data. At 3 T BS is shown to improve detection of CBF changes whilst the second acquisition maintains sensitivity to BOLD. High resolution CBF and BOLD data can be

collected at 7 T using DABS .

5.3 Discussion

Moving to ultra-high field brings several advantages such as significant increase in SNR and CNR due to the longer relaxation times. However, there are known challenges of a larger contribution of the physiological noise to the data and, as were found, additional hardware issues involving the Roman Artefact at 7 T. The DABS sequence can overcome these problems by eliminating static tissue signal. This sequence provides improved temporal stability resulting in higher statistical significance of the ASL data at a cost of small decrease in the BOLD signal. However, due to the increased BOLD response with field strength, this reduction has a minimal effect. DABS proved to not only be a very efficient tool in overcoming the RA but also to provide a better source-based physiological noise correction method than RETROICOR [83].

This method can be an excellent tool for the simultaneous ASL and BOLD measurement at ultra-high field. It can be applied to any data that are particularly susceptible to the high contribution from cardiac and respiratory motion as well as any artefacts originating from the signal intensity, such as the Roman Artefact. Thus its application could appeal for the study of hypercapnia, where it can be used for calibrated BOLD studies. A further application is to the study of pharmaceutical modulations, where temporal stability must be maximised.

Chapter 6

Simple model of measuring Arterial Cerebral Blood Volume (CBV_a) from LL-FAIR

Arterial Cerebral Blood Volume (CBV_a), the volume of blood in the parenchymal arterial vessels, is an important parameter in assessing vascular control. Previously, it has been assumed that blood volume changes in response to activation originate from ballooning of the elastic venous vessel wall [74]. However, recent studies have shown that CBV_a increases on brain activation and that venous blood volume changes may, in fact, be small [35, 92, 93]. CBV_a may therefore provide a more direct, quantitative, MRI measure of brain activation than BOLD or CBF and aid modelling of the BOLD response to improve identification of the origin of neurovascular responses. Pulsed Arterial Spin Labelling (PASL) techniques measure cerebral blood flow, but these techniques are also sensitive to signal in the arterial blood compartment, seen as bright foci in ASL images at short post-labelling delay times (TI). Vascular crushing (generally using flow-sensitive bipolar gradients) is often used to remove this signal [94], but this signal provides valuable information, which can be used

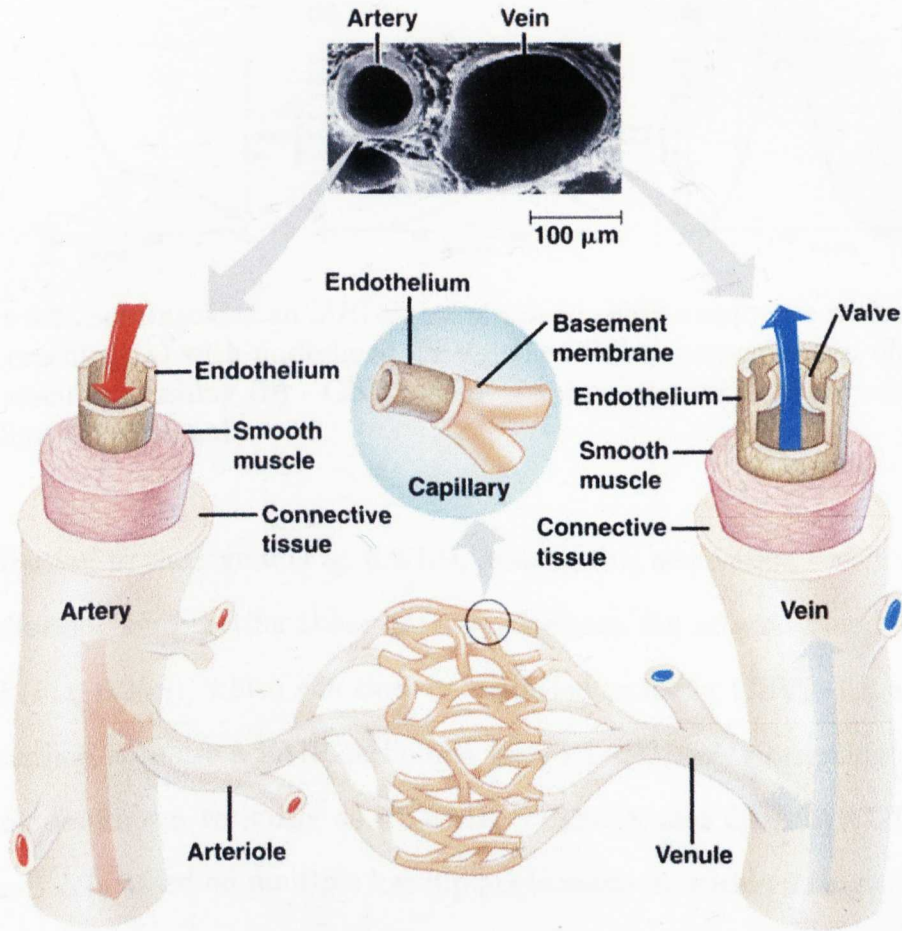


Figure 6.1: Image of an artery and a vessel (top) with a schematic representation and anatomical details of an artery, arteriole, capillary bed, venule, and vein (bottom) [95].

to measure CBV_a . Figure 6.1 shows a schematic representation of the arterial and venous systems, and capillary bed.

The use of standard PASL techniques (such as FAIR) to measure CBV_a is very time consuming (~ 30 minutes) as several data sets must be acquired at a range of inversion delays (TIs), each with and without vascular crushing. The data acquired without the vascular crushing is sensitive to both arterial blood volume signal and perfusion, resulting in a co-added signal from both (Fig. 6.2(a)). Using vascular crushing (in this thesis, if used, a diffusion-weighted gradient was applied with 5 ms duration of both lobes and an amplitude of $15 \frac{mT}{m}$ at 3 T and $8.7 \frac{mT}{m}$ at 7 T) eliminates the vascular

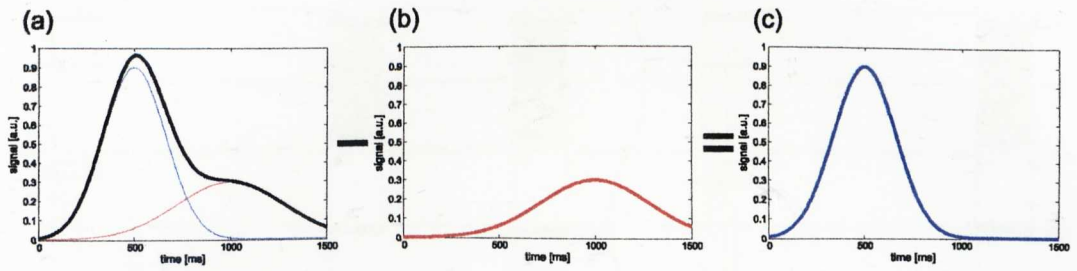


Figure 6.2: Schematic of an MRI signal obtained using a sequence with no vascular crushing (a) with underlined CBV_a and CBF responses; signal obtained with vascular crushing (b) - CBF sensitive; subtraction of both responses (c) revealing CBV_a signal.

contribution to the signal (Fig. 6.2(b)), making this acquisition sensitive only to perfusion. Subtracting these data sets isolates the arterial blood volume signal (Fig. 6.2(c)), which can then be modelled to fit for CBV_a . An alternative method is to use a FAIR technique with a Look-Locker sampling scheme (techniques known variously as LL-FAIR, ITSFAIR and QUASAR). LL-EPI acquisition is based on multiple low flip angle readouts within a single TR. As shown in Figure 6.3, this scheme compares alternating non-selective and selective Look-Locker inversion recovery signals acquired at a range of TI values in a single shot. If an optimised combination of flip angle and timing of the readout pulses is used [96], this sequence is only sensitive to CBV_a signals and requires no vascular crushing; it has been shown that the optimised sensitivity to CBV_a causes suppression of the CBF signal. The Look-Locker sampling has to be performed at the intervals shorter than the tissue transit time with a readout pulse flip angle of about 50° . CBV_a and the transit times can then be measured noninvasively from ~ 5 minutes data acquisition [96]. In the past a Step-wise Compartmental Model (SCM) [97], which iteratively estimates the signal based on repeated application of the Bloch equations, or a model-free method [98], has been used to fit the data. The model-free method uses a series of correction factors for the difference images, however, this method still requires image acquisition with and without vascular crushing. Both Perfusion-

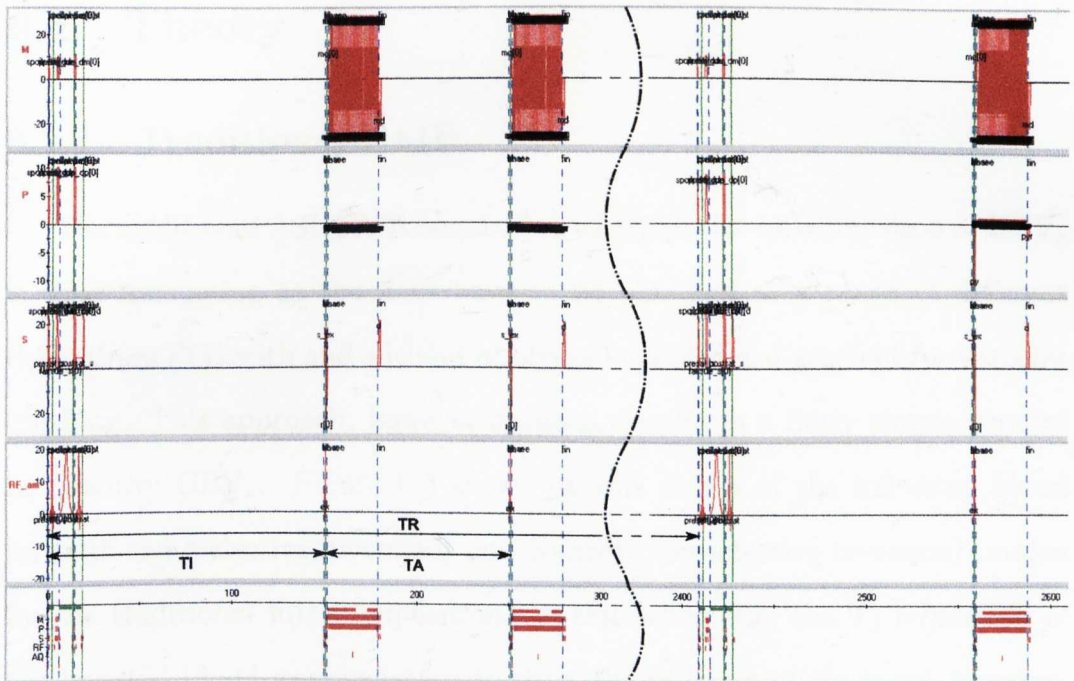


Figure 6.3: LL-FAIR sequence simulated with the Philips AcqSim. Measurement (M), phase (P), and slice selection (S) directions of the gradients and RF—am pulse profile are shown as a function of time [ms]. Left panel shows the selective (tag) inversion pulse followed by the series (only two shown) of read out pulses. Right panel presents the non-selective (control) inversion pulse followed by the readout pulses.

Weighted (PW) images (ΔM) are then subtracted and corrected for the T_1 blood relaxation. The area under the received time-dependent curve is then calculated and corrected for M_0 of blood, the duration of the label, “W”, and the inversion efficiency (α).

This chapter describes the simplified method for quantitatively measuring CBV_a from LL-FAIR data, validation of this new model against the SCM, and application to measure CBV_a and changes on activation.

6.1 Theory

6.1.1 Traditional FAIR

The traditional ASL FAIR acquisition technique for quantification of CBV_a is time consuming as the data have to be obtained at a range of different delay times (TI) with and without applying an additional gradient for vascular crushing. This approach, however arduous, results in a fairly simple process to quantify CBV_a . Figure 6.4 shows various stages of the inflowing blood for both tag (selective inversion) and control (non-selective inversion) images for the traditional FAIR acquisition. In this schematic, the T_1 relaxation of the inverted blood was neglected to show the progress of the input function. First, the blood is inverted by applying inversion slabs for tag and control. A saturation slab of a width sufficient to cover the imaging slices is then applied (Fig. 6.4(a)). In Figure 6.4(b), the images represent the situation after time Δ , the “arterial transit time” (defined by the width of the selective inversion), when the leading edge of the recovered blood in the tag and the inverted blood in the control acquisition (labelled blood) reach the imaging slice. The labelled blood then starts filling the network of arteries and arterioles within the imaging slice (Fig. 6.4(c)) and after a time δ , the “arteriolar transit time” (the time blood remains in the arterial blood compartment of a voxel), the labelled blood fills the entire arteriolar space in the imaging slice (Fig. 6.4(d)). Only when the label arrives at the extravascular space of the capillary bed, after a time $\sim \Delta + \delta$, the exchange occurs giving rise to a PW ASL signal. Thus at short TIs the difference signal between tag and control images is dominated by signal from the arterial blood. The Full Width Half Maximum (FWHM) of the input response is then dependent on the temporal duration of the label through the vasculature, “W” (“temporal label width” of the non-selective inversion), which will depend on the non-selective label width, the size of the

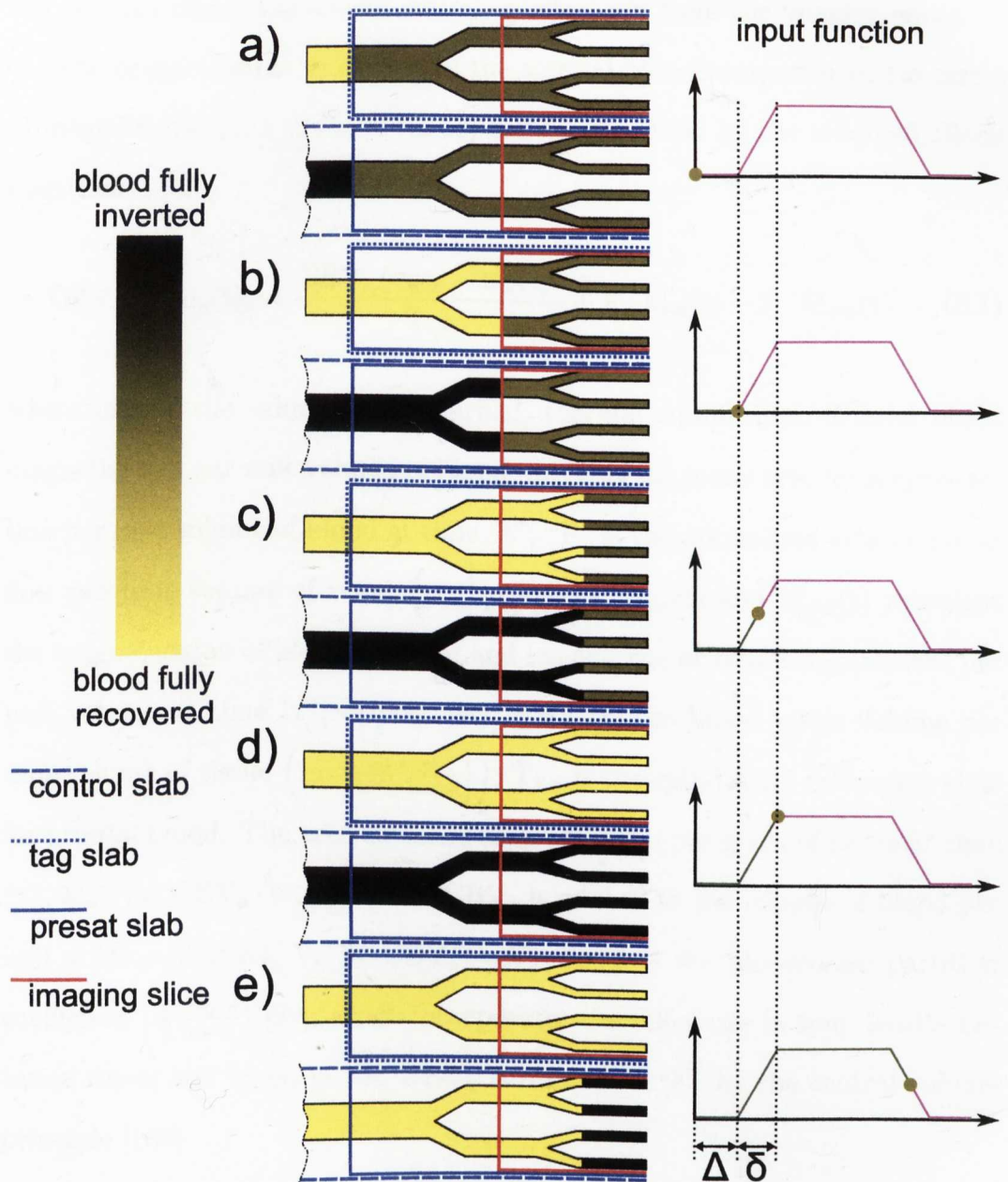


Figure 6.4: Schematic representation of FAIR tag and control acquisitions at various stages: (a) immediately following inversion and saturation pulses; (b) following arterial transit time Δ where the labelled blood (black) reaches the imaging slice; (c) the labelled blood has filled half of the imaging slice (arterioles); (d) after the time δ where the labelled blood reaches the capillary bed within the imaging slice (perfusion); (e) the labelled blood has almost entirely washed out from the imaging slice. T_1 relaxation is not included in the schematic.

vessel, and blood flowing through it. Figure 6.4(e) shows the situation when the labelled blood was almost entirely washed out from the imaging slices.

The magnetisation in a voxel of the arterial blood compartment (in terms of magnetisation per gram of tissue) can be described by the modified Bloch equation:

$$CBV_a \frac{d}{dt} (m_a(t)) = \frac{CBV_a (m_{0,a} - m_a(t))}{T_{1,b}} + F \cdot M_{in}(t) - F \cdot M_{out}(t), \quad (6.1)$$

where $m_{0,a}$ is the value of unperturbed, thermal equilibrium, arterial blood magnetisation per unit volume of blood; $m_a(t)$ is the mean arterial magnetisation per unit volume of blood at time “t”; “F” is the normalised arterial blood flow per unit volume of voxel (in $\left[\frac{\text{ml}}{100\text{g min}}\right]$); $M_{in}(t)$ and $M_{out}(t)$ represent the magnetisation of blood entering and leaving the arterial compartment per unit volume at time “t”, respectively; CBV_a is the blood water volume per unit volume of tissue (in $\left[\frac{\text{ml water}}{100\text{g tissue}}\right]$); $T_{1,b}$ is the spin-lattice relaxation time for arterial blood. The arterial blood magnetisation per gram of tissue at time “t”, $M_a(t) = CBV_a \cdot m_a(t)$, where CBV_a is related to the volume of blood per unit volume of voxel, V_a by $CBV_a = V_a \cdot \lambda$. λ is the blood:brain partition coefficient $\left[\frac{\text{ml blood}}{\text{g tissue}}\right]$ [99], which incorporates the difference in spin density between tissue and blood pools. CBV_a is related to “F” by the central volume principle [100]:

$$CBV_a = \delta F. \quad (6.2)$$

The difference in arterial blood magnetisation, $\Delta M_a(t)$, depends on the difference in $M_{in}(t)$ and $M_{out}(t)$ between the label and non-label conditions (Eq. 6.1). Referring to Figure 6.4, following the arterial transit delay, Δ , labelled blood enters the imaging voxel and remains in the intravoxel arterial blood compartment for the average “arteriolar transit time” δ , it then either flows out of the imaging volume to a neighbouring voxel or enters the capillary

section of the imaging voxel where exchange occurs. If the label slab has a finite spatial width and hence temporal label width, “W”, then after a time $W + \Delta + \delta$ fresh non-labelled blood will fill the arterial compartment and the arterial blood magnetisation difference signal returns to zero. For plug flow, ideal inversion of the labelled blood, complete refreshment of blood in the TR period, and “W” greater than δ (true for ASL experiments using standard label widths) $\Delta M_a(t)$ can be described in terms of five discrete time intervals (indicated in Figure 6.5(i)):

1. $t < \Delta$:

$$\Delta M_a(t) = 0; \quad (6.3)$$

2. $\Delta \leq t \leq \Delta + \delta$, during inflow of the tag to the arterial blood compartment:

$$\Delta M_a(t) = 2m_{0,a}F(t - \Delta)e^{-\frac{t}{T_{1,b}}}; \quad (6.4)$$

3. $\Delta + \delta \leq t \leq \Delta + W$, when the arterial blood compartment is completely filled with labelled blood:

$$\Delta M_a(t) = 2m_{0,a}F\delta e^{-\frac{t}{T_{1,b}}} = 2m_{0,a}CBV_a e^{-\frac{t}{T_{1,b}}}, \quad (6.5)$$

During this time interval, $\Delta M_a(t)$ is proportional to CBV_a and a $T_{1,b}$ exponential decay function;

4. $\Delta + W \leq t \leq \Delta + W + \delta$, during outflow of the label from the arterial blood compartment:

$$\Delta M_a(t) = 2m_{0,a}F(\Delta + W - t)e^{-\frac{t}{T_{1,b}}}; \quad (6.6)$$

5. $t > \Delta + W + \delta$:

$$\Delta M_a(t) = 0. \quad (6.7)$$

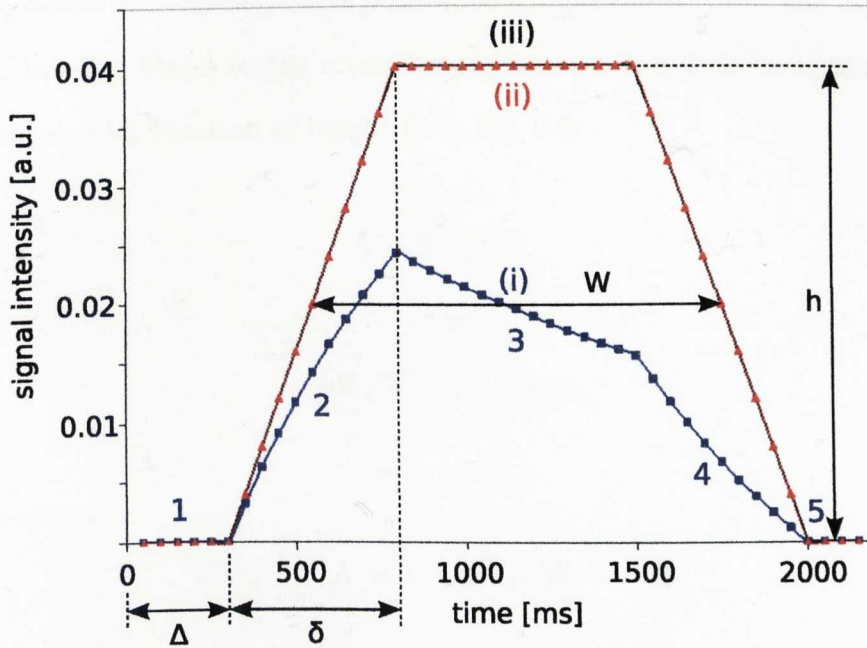


Figure 6.5: Simulated FAIR signal (i); corrected for T_1 of blood (ii) with fitted trapezoidal input function (iii). Numbers 1 – 5 indicate discrete time intervals for FAIR data.

Considering a trapezoidal input function, quantification of CBV_a , using the traditional FAIR data acquisition, is thus simple; ΔM (difference between tag and control) images are first normalised to the equilibrium blood magnetisation, $m_{0,a}$. Next, the arterial signal of a single voxel is recorded for each time point of the different TI values¹ (averaged over multiple dynamics or cycles in the case of fMRI acquisition) to form a signal intensity curve (Fig. 6.5(i)). Additionally, the original signal intensity curve has to be corrected for the relaxation time of blood ($T_{1,b}$) – multiplication by $e^{\frac{t}{T_{1,b}}}$ to normalise to the equilibrium of blood magnetisation (Fig. 6.5(ii)). The corrected signal then reflects the input function (Fig. 6.5(iii)), therefore the arterial cerebral blood volume can be quantified using one of the approximations. CBV_a value is then represented by the percentage content of the blood within a voxel.

¹In the past, it was suggested that an acquisition of a single TI value can be used to quantify CBV_a [93], however this approach seems to be limited as the acquisition must be performed at the peak, which changes with Δ that also changes on activation.

If considering a non-selective pulse with a finite width, “W”, the input function of labelled blood to the arterial compartment can then be approximated as a trapezoidal function of height from Eq. 6.5:

$$h = 2 \cdot \text{CBV}_a, \quad (6.8)$$

$$\text{or} \quad (6.9)$$

$$\frac{\Delta M}{m_{0,a}} e^{\frac{\delta}{T_{1,b}}} = 2 \cdot \text{CBV}_a, \quad (6.10)$$

or the area:

$$A = 2 \cdot \text{CBV}_a \cdot W, \quad (6.11)$$

where “W” is full width at half height, δ (arteriolar transit time) slope length starting at time Δ (arterial transit time).

6.1.2 Look-Locker FAIR

The Look-Locker sampling method combined with FAIR ASL technique introduces additional complications in comparison with traditional FAIR technique. Figure 6.6 shows the affect of LL-FAIR acquisition on FAIR technique at various stages omitting longitudinal relaxation. After the initial inversion and saturation (Fig. 6.6(a)) and prior to the transit time Δ (Fig. 6.6(b)), fast acquisition with low flip angle has no affect on the longitudinal magnetisation, as it was previously saturated (nulled), therefore it is similar to the traditional FAIR acquisition. However, once the labelled blood flows into the imaging slice (Fig.6.6(c)), each LL-EPI readout will suppress the magnetisation within the imaging slice slab; inverted blood is progressively tipped closer to the null point with every readout pulse and fully recovered blood is suppressed with each readout. Figure 6.6(d) shows the scenario after additional time δ when the labelled blood has filled in the entire arteriolar space (including capillary

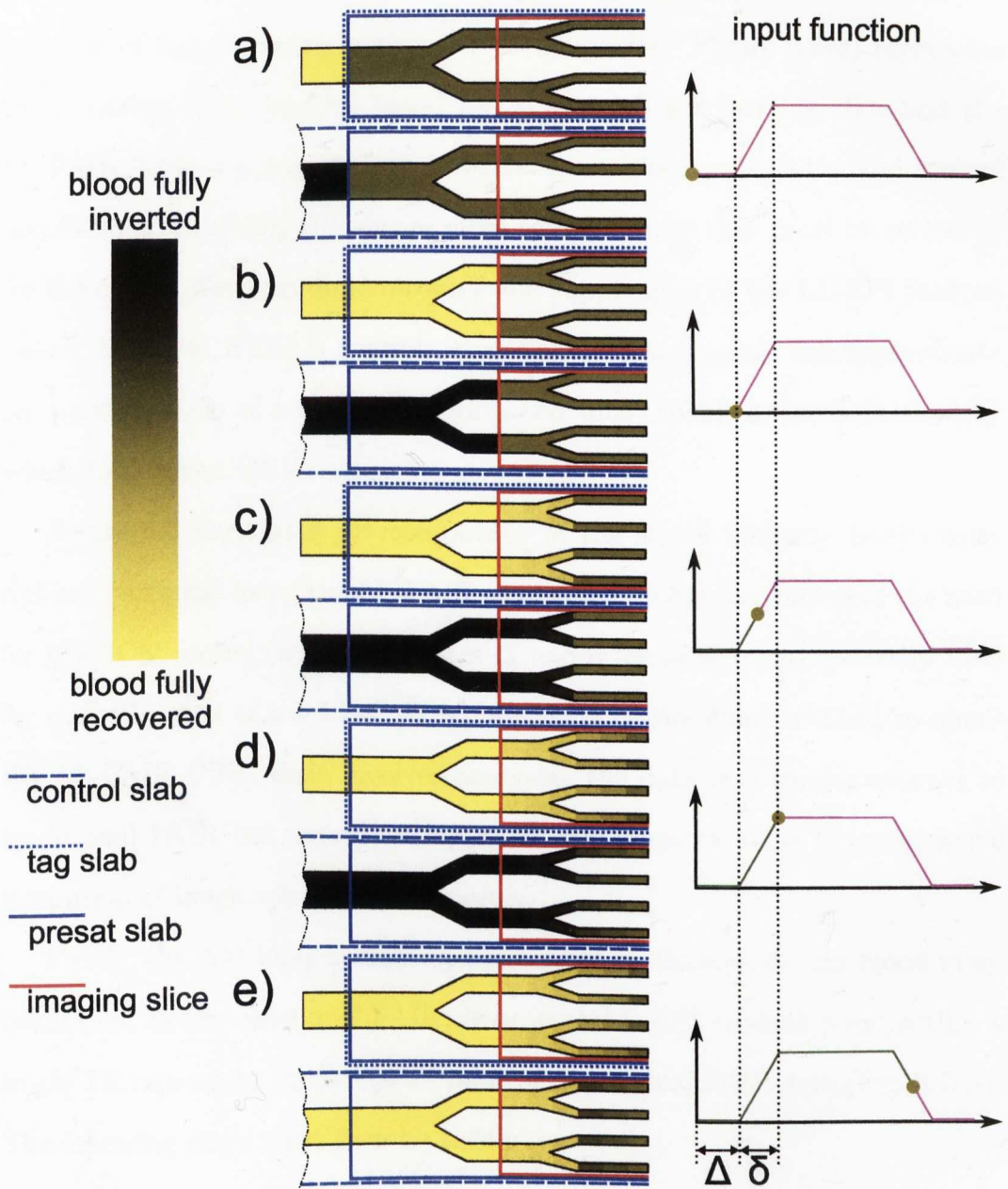


Figure 6.6: Schematic representation of Look-Locker EPI sampling method for FAIR tag and control acquisitions: (a) immediately following inversion and saturation pulses; (b) following arterial transit time Δ where the labelled blood (black) reaches the imaging slice; (c) the labelled blood has filled half of the imaging slice (arterioles), each readout suppresses the magnetisation according to the applied flip angle of readout pulses; (d) after the time δ where the labelled blood reaches the capillary bed within the imaging slice (perfusion), here the LL-FAIR contribution to the imaging slices is most pronounced; (e) the labelled blood has almost entirely washed out from the imaging slice. T_1 relaxation is not included in the schematic.

bed) of the imaging slice and the LL-FAIR readout pulses have established stability of magnetisation within the imaging slice. Figure 6.6(e) represents the situation when labelled blood has almost left the imaging slice and the LL-FAIR readout pulses start to have the same affect on both tag and control acquisitions. LL-FAIR signals are more complex since they must be corrected for the effects of longitudinal recovery and suppression by the LL-EPI readout pulses. However, if this is possible, then the corrected signals will approximate an input function of a trapezoidal form and thus provide a simple method by which to measure CBV_a .

Figure 6.6 illustrates the complexity of the signal intensity in the arterial compartment using the LL-FAIR acquisition technique, therefore the need for the SCM model (which estimates Δ and δ for each voxel) generally used for quantification of the LL-FAIR approach. The simplified method to quantify LL-FAIR CBV_a data involves analysing the data in a similar manner to traditional FAIR but incorporating additional steps to allow for progressive saturation of longitudinal magnetisation.

Firstly, the ΔM images must be normalised to the equilibrium blood magnetisation, as for traditional FAIR. Now, each LL-EPI readout point within a single TR represents a different TI value of the original FAIR data (Fig. 6.7(i)). The following steps must then be taken:

1. correction for longitudinal recovery of the inversion (multiplication by $e^{\frac{\delta}{T_{1,b}}}$ (Fig. 6.7(ii));
2. from the T_1 -corrected data δ must be estimated – crucial for correct estimation of the CBV_a value (Fig. 6.7(iii));
3. the correction for the suppression of blood, by the “n” Look-Locker readouts, as it travels through the voxel, must then be performed by multi-

plication by:

$$\frac{(1 - \cos(\theta)) \cdot n}{[1 - (\cos(\theta))^n] \cdot \sin(\theta)}, \quad (6.12)$$

where $n = \frac{\delta}{TA}$ and TA is the LL-EPI readout pulse spacing (Fig. 6.7(iv)). The correction is only accurate for times $> \Delta + \delta$, and the discrepancies are shown in Figure 6.7(iv) and (v). This deviation is a result of “n” being only accurate for a steady state as within time $< \Delta + \delta$, small portions of blood experience intermediate amount of LL-EPI readouts.

The arterial blood within a voxel can then be estimated using either $T_{1,b}$ -corrected data (Fig. 6.7(iv)) or fitting the data to a trapezoidal input function (Fig. 6.7(v)), the best approach is assessed later. Each method requires initial estimation of δ before the LLEPI correction can be applied. This is crucial in providing an accurate correction factor for LLEPI suppression and can be determined by a cross point between the linear approximation of the slope’s

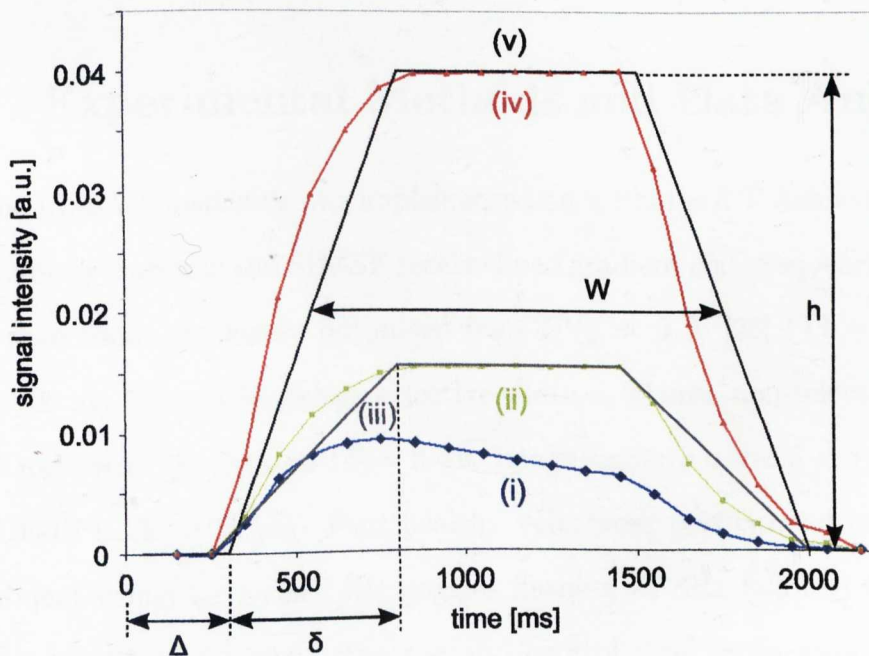


Figure 6.7: Simulated LL-FAIR signal (i) with applied correction for T_1 blood recovery (ii); estimation of δ using a trapezoidal fit (iii); correction for Look-Locker EPI acquisition (iv) with a trapezoidal fit for input function (v).

leading edge and plateau of the T_1 blood corrected data. 1000 repeat fits were performed for each simulated data set and the errors in the measurement of CBV_a for the different values of Δ , δ , and CBV_a were assessed.

For preliminary validation, Monte Carlo modelling was used to compare this simplified approach against simulated data generated and fitted using SCM. Data sets were simulated with the SCM for parameters' values ($\Delta = 100 - 300$ ms, $\delta = 500 - 700$ ms, $CBV_a = 2 - 3$ %, $W = 1500$ ms) and Gaussian noise added (mean = 0, standard deviation = 0.01). CBV_a was then estimated from the simulated data using four methods:

- (I) peak amplitude of the simulated signal (Eq. 6.10);
- (II) area under curve of simulated signal (Eq. 6.11);
- (III) height (h) of the fitted trapezoid (Fig. 6.7);
- (IV) area of fitted trapezoid.

6.2 Experimental Methods and Data Analysis

The LL-FAIR sequence was implemented on a Philips 3 T Achieva scanner using a body transmit and SENSE receive head gradient coil. Sequence timings used were those previously optimised for CBV_a at 3 T [96] ($TI = 150$ ms, $TA = 100$ ms, 19 readout pulses, selective width = 30 mm, non-selective width = 200 mm) with the jittered $TR = 2.4$ s. Image resolution was $3 \times 3 \times 5$ mm³ and GE-EPI $TE = 16$ ms. Four healthy volunteers participated in a visual experiment using 4.8 s red LED goggles flashing at 8Hz followed by 26.4 s rest repeated for 14 cycles. The tag and control time series were realigned separately using a standard algorithm in SPM (with a 5 mm FWHM Gaussian smoothing kernel and 2nd Degree B-Spline interpolation), both registered to the same base EPI image for the same spatial placement. The LL-FAIR difference

signals ΔM (tag – control) were extracted and normalised to the equilibrium blood magnetisation $m_{0,a}$ (estimated from sagittal sinus). This normalised data was then fitted using methods (I-IV) and the SCM and estimates of CBV_a were compared.

6.3 Results

Figure 6.8 shows the difference images ($\Delta M = \text{tag} - \text{control}$) of each LL-FAIR readout corresponding to different TI values (noted on each image). Brightening parts of the image are a clear indication of the inflowing blood to the imaging slice and represent the amount of labelled blood in the arteries and arteriolar compartment. Timing of readout pulses (TI and TA) were optimised to only be sensitive to CBV_a while the perfused signal is suppressed and the static tissue signal is being removed by subtraction of ΔM images.

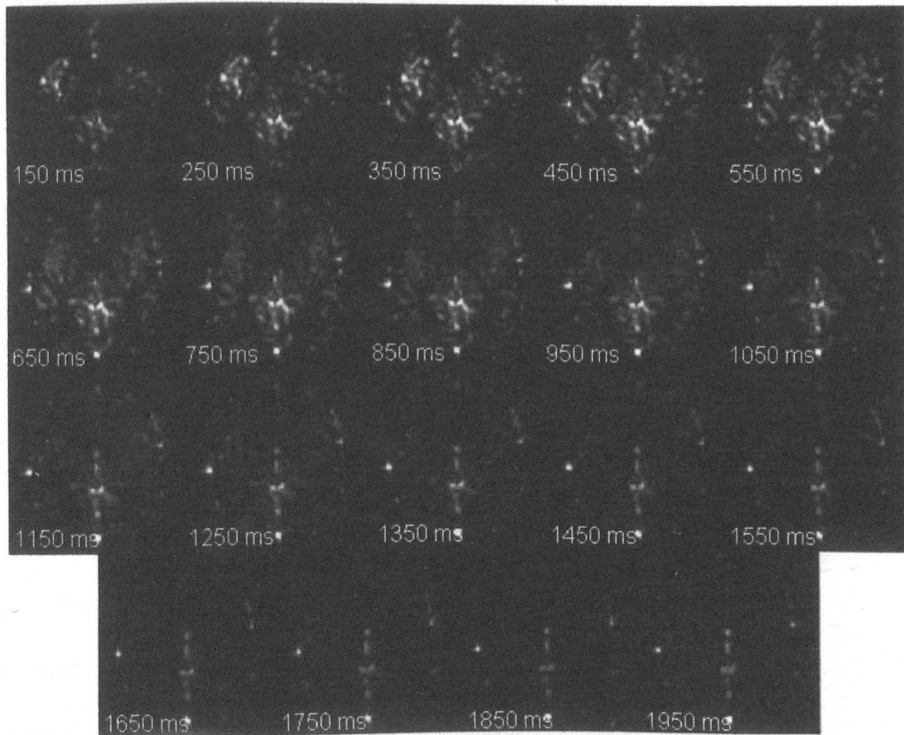


Figure 6.8: Difference images (ΔM) representing 19 LL-FAIR readout points of a single TR. Each readout is equivalent to a different delay time (TI), noted.

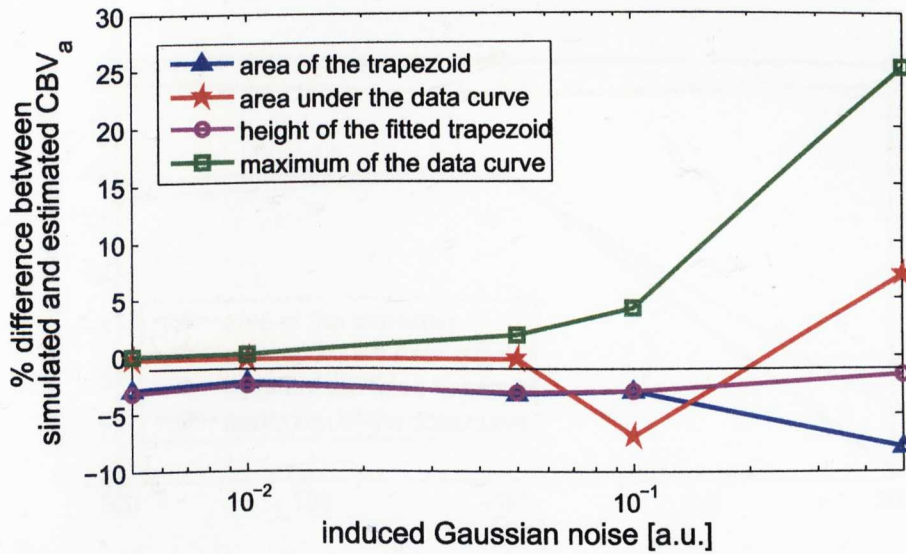


Figure 6.9: Percentage difference between simulated and estimated CBV_a data as a function of induced Gaussian noise for four different methods: (I) – maximum signal of the simulated data curve (green); (II) – area under the simulated data curve (red); (III) – height of the fitted trapezoid (purple); (IV) – area under the fitted trapezoid (blue). Values estimated for this simulation: $\Delta = 100$ ms, $\delta = 500$ ms, $W = 1500$ ms.

Figure 6.9 shows the relative difference [%] between simulated and fitted values of CBV_a for the four fitting methods. The simulations were performed with a contribution of a Gaussian noise of different magnitude. Monte Carlo simulations showed that the measured peak signal, method (I), provided the most reliable estimate of CBV_a for Gaussian noise < 0.01 ; for higher noise levels, the height of the trapezoidal fit, method (III), delivered closest estimation. As Δ increased the accuracy of estimated CBV_a was reduced (Fig. 6.10), especially for both methods involving trapezoidal fit (method (III) and (IV)). This was due to the increased noise in the data as a result of the longer period available for T_1 recovery of blood. As δ increased, the accuracy of CBV_a estimation was also reduced (Fig. 6.11), particularly for those methods (III) and (IV) that are based on trapezoidal fit since the onset/offset slopes, which are of length δ , are not well matched to a trapezoid function (Fig. 6.7). In estimating CBV_a , Method (II) was also inaccurate for high values of δ , which is

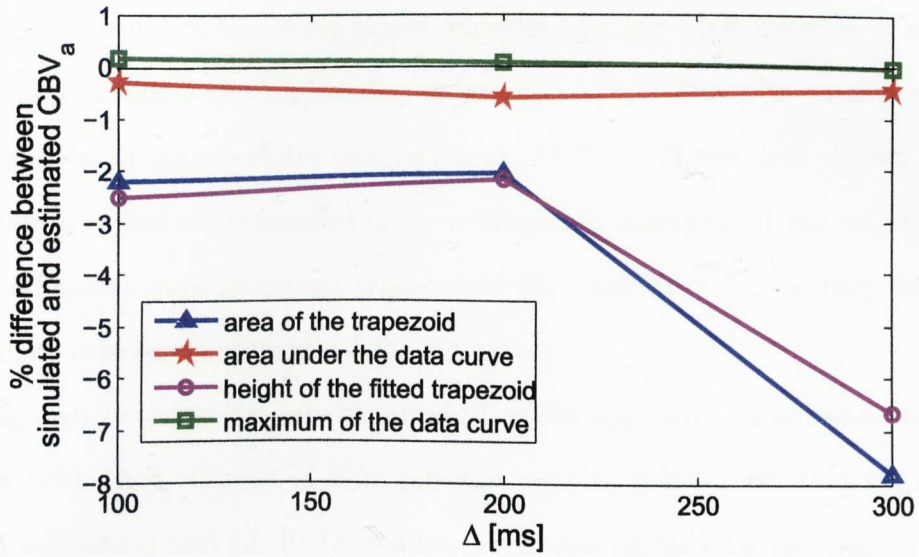


Figure 6.10: Percentage difference between simulated and estimated CBV_a data as a function of arteriolar transit time δ for four different methods: (I) – maximum signal of the simulated data curve (green); (II) – area under the simulated data curve (red); (III) – height of the fitted trapezoid (purple); (IV) – area under the fitted trapezoid (blue). Values estimated for this simulation: $\delta = 500$ ms, $CBV_a = 3\%$, $W = 1500$ ms.

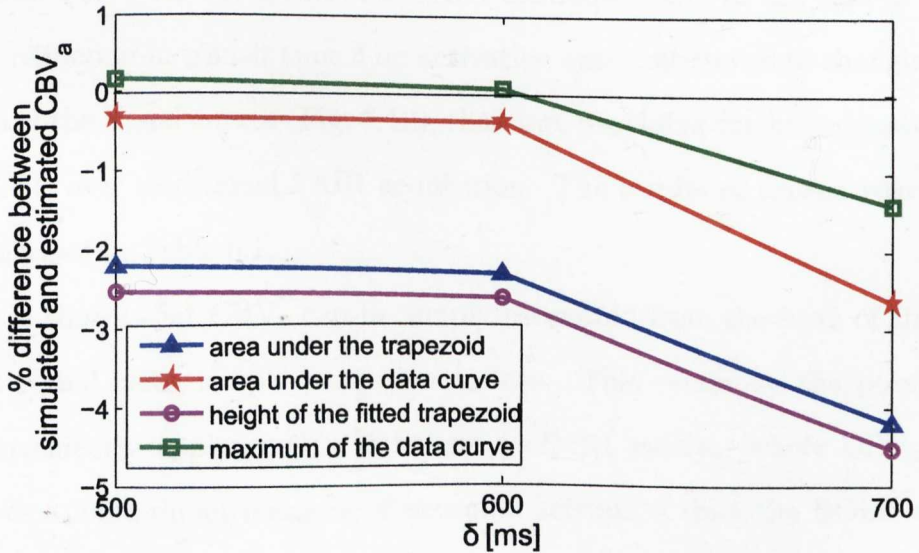


Figure 6.11: Percentage difference between simulated and estimated CBV_a data as a function of arteriolar transit time δ for four different methods: (I) – maximum signal of the simulated data curve (green); (II) – area under the simulated data curve (red); (III) – height of the fitted trapezoid (purple); (IV) – area under the fitted trapezoid (blue). Values estimated for this simulation: $\Delta = 100$ ms, $CBV_a = 3\%$, $W = 1500$ ms.

due to the nature of the offset slope: experiencing less SNR because of the T_1 relaxation of blood and higher dispersion of the input function caused by the tortuousness of the arteriolar compartment. Method (I) was then chosen in the estimation of the experimental data to eliminate inclusion of the offset slope and additional steps involving trapezoidal fit; application of ancillary fits can introduce misrepresentations of the estimates.

Figure 6.12 shows the experimental LL-FAIR data with a marked activation region with time courses of four selected voxels. Both correction steps (T_1 blood relaxation and LL-FAIR readout) are also plotted for the resting state and visual activation. Voxels were selected to emphasise a variety of shapes of the signal curves, which mostly depend on the tortuousness of the vascular system; blood then reaches and remains within a voxel for a different amount of time. This highlights the necessity for acquisition at a range of TI values to estimate CBV_a for the traditional FAIR technique [93]. In the case of fMRI data, reduction in transit time δ on activation also contributes to changing the shape of the signal curves (Fig. 6.12), therefore providing further advantage to LL-FAIR over traditional FAIR acquisition. The results of chosen voxels are summarised in Table 6.1.

It is shown that CBV_a can be simply estimated from the peak of the LL-FAIR signal using simple correction factors. This opens up the possibility of conveniently applying this technique to fMRI studies, where CBV_a may provide a more direct measure of neuronal activation than the BOLD effect. The model described here assumes that the input function is trapezoidal, but in practice variation of vessel sizes within an ROI and dispersion of the label will lead to deviations from a trapezoid (Fig. 6.12). LL-FAIR voxel-by-voxel analysis of the data can be used to form CBV_a maps. The use of LL-FAIR will also provide an opportunity to study the exact form of the arterial input function of the label to the voxel.

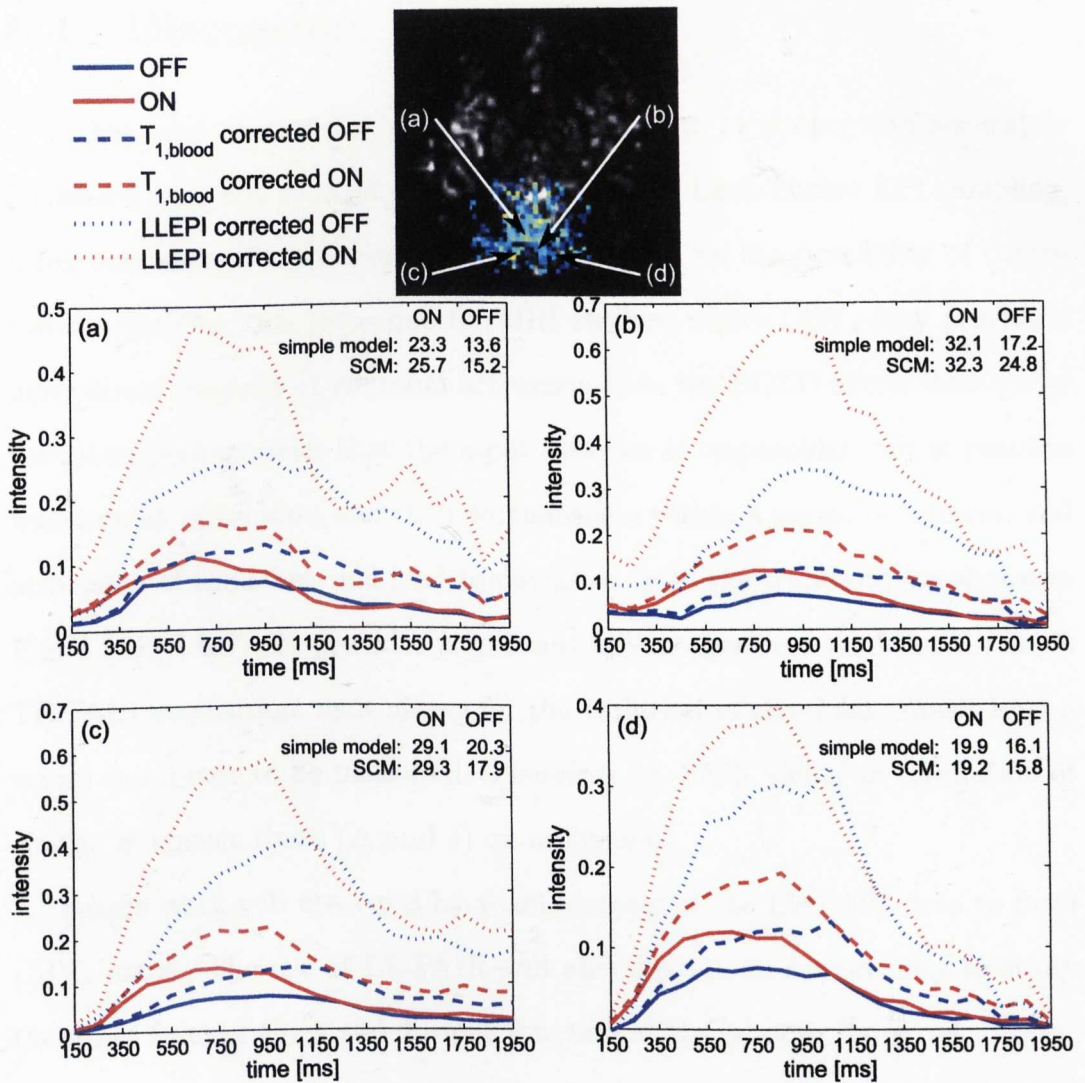


Figure 6.12: Averaged LL-FAIR image with marked activated area to the visual stimulus. Four voxels were chosen and time courses extracted with correction steps shown in order to quantitatively estimate CBV_a for resting state (OFF) and on activation (ON) using simplified method. CBV_a values were then verified against the Step-wise Compartmental Model for each voxel.

Table 6.1: Estimated values for Δ , δ , and CBV_a using the simplified model.

voxel	resting state			on activation		
	Δ [ms]	δ [ms]	CBV_a [%]	Δ [ms]	δ [ms]	CBV_a [%]
(a)	270	370	13.6	150	300	23.3
(b)	450	400	17.2	300	350	32.1
(c)	250	609	20.3	220	513	29.1
(d)	200	450	16.1	150	350	19.9

6.4 Discussion

It has been shown that quantitative CBV_a can be simply and accurately estimated from the peak of the FAIR signal with Look-Locker EPI sampling, using only several correction factors. This opens up the possibility of conveniently applying this technique to fMRI studies, where CBV_a may provide a more direct measure of neuronal activation than the BOLD effect. The model described here assumes that the input function is trapezoidal, but in practice variation of vessel sizes and their tortuousness within a region of interest, and dispersion of the label, will lead to deviation from the trapezoid (as shown in Fig. 6.12). LL-FAIR provides significant advantages over traditional (single TI) FAIR acquisition, as it allows for the variation in arteriolar transit time δ across the cortex to be measured. Therefore LL-FAIR yields an estimation of change in transit times (Δ and δ) on activation.

Future work will use voxel-by-voxel analysis of the LL-FAIR data to form CBV_a maps. The use of LL-FAIR will also provide an opportunity to study the exact form of the arterial input function of the label to the voxel.

Chapter 7

Applications

This chapter outlines the application of Look-Locker (LL) based qualitative (perfusion weighted) and quantitative ASL methods for measuring Cerebral Blood Flow (CBF) and Cerebral Blood Volume (CBV_a), highlighting their advantages. The Look-Locker technique provides a method of ASL acquisition which can result in significantly increased signal-to-noise ratio and reduced acquisition time compared to standard methods. Qualitative CBF-weighted and CBV_a -weighted images are of interest to clinicians where fast assessment of blood flow and arterial blood volume related changes can be critical, but quantitative assessment is not essential. However, there may not be a simple relationship between a qualitative measure and quantitative value due to transit time changes also occurring. In this Chapter LL-based ASL sequences are used to monitor relative and absolute changes in CBV_a and CBF in response to visual activation with high temporal resolution. A second study uses quantitative ASL measures to determine the relationship between CBF, CBV_a and total CBV, in order to assess the Grubb power-law [101] which is widely used in calibrated BOLD [87] and BOLD modelling [88] studies. Total CBV is measured using contrast agent techniques and compared to CBF and CBV_a haemodynamic responses on both an inter-subject and intra-subject ba-

sis. Few studies have directly compared the responses of these haemodynamic parameters, and this is the first *in vivo* study to assess the relationship between CBF, CBV_a and total CBV .

7.1 Assessing the Temporal Responses of CBF and CBV_a Measures

BOLD provides a qualitative measure of brain activity and depends on changes in blood flow, blood volume (until recently assumed to be dominated by venous volume changes) and oxygen consumption resulting from neural activation. To understand neural activity it is better to measure directly these changes in CBF, CBV and CMRO₂ quantitatively (for example for CBF in units of $\left[\frac{\text{ml}}{100\text{g}\cdot\text{min}}\right]$ or CBV in $\left[\frac{\text{ml}}{100\text{g}}\right]$). Sometimes a qualitative approach (in the form of CBF-weighted or CBV_a-weighted images) is acceptable to assess brain function, particularly if interest lies in determining the time course and spatial location of relative changes in haemodynamic responses on activation.

As outlined in Chapter 6 and 4.1 ASL provides a non-invasive method to measure CBF and CBV_a. The sensitivity to detect these changes is improved by following the ASL labelling scheme with a Look-Locker EPI readout. LL-EPI sampling uses multiple low flip angle pulses, which when combined with ASL, sample the inflowing blood signal as it exchanges with the tissue forming a sequence which is sensitive to CBF. Alternatively, if high flip angle pulses are applied more rapidly, then the signal from the exchanging water is suppressed, and the sequence is then sensitive solely to CBV_a [96]. As previously shown [96,97] and discussed in Chapter 6 the timing between read-out pulses as well as their flip angle have to be chosen very carefully.

LL-FAIR has been shown to provide a method to determine activation-based relative changes in CBV_a and CBF from the ΔM images ($\Delta M = \text{tag} -$

control). Using this method the associated changes (reduction) in arterial and tissue transit times (Δ and δ , respectively), can also be measured [96,97]. However, ASL based perfusion-weighted images arise from a signal change (between a selective and non-selective conditions) which is of only a few percent. Therefore to detect changes induced by neuronal activity it is crucial for this technique to be very sensitive and the underlying MR signal must be very stable. This has previously limited activation studies to long duration stimuli or long paradigms with a large number of a cycles. The LL-FAIR technique can provide a method of increasing the perfusion weighted SNR of an ASL data acquisition by summing over the signal change of each readout pulse in the LL-EPI train to overcome these limitations.

Knowledge of the temporal dynamics of CBV_a and CBF responses to neural activation is important for BOLD modelling [102]. The aim of this section is to use LL-FAIR to compare the temporal dynamics of arterial blood volume and blood flow weighted responses to visual stimuli of 4.8 and 9.6 s duration.

7.1.1 Experimental Methods and Data Analysis

The LL-FAIR sequence was implemented on a Philips 3 T Achieva scanner using an eight-channel SENSE head RF coil. The following sequence timings were used in this experiment:

- **CBF:** TI = 600 ms, TA = 360 ms, $\theta = 40^\circ$, 5 readout pulses;
- **CBV_a :** TI = 150 ms, TA = 100 ms, $\theta = 50^\circ$, 21 readout pulses;

where, TI is the time between the inversion pulse and the first readout pulse, and TA is the time between evenly spaced readout pulses, and θ is the flip angle of each readout pulse. The thickness of the imaging slice was 5 mm and the width of the FAIR labelling (inversion) slab alternated between 30 and 200 mm for the selective and non-selective conditions, respectively. The TR

between inversion pulses was 2.4 s (4.8 s per tag – control pair). A short TR is acceptable due to the spatially confined (200 mm) non-selective slab. The EPI echo time was 16 ms (shortest achievable) and the image resolution was $3 \times 3 \times 5 \text{ mm}^3$. The flip angle θ of the final LL-EPI readout pulse for both the CBF and CBV_a sequences was set to 90° to maximize signal-to-noise ratio and to provide suppression of the imaging slice prior to subsequent readout, hence aiding to reduce any offset signals due to imperfections between selective and non-selective pulses. This also led to simplification of the quantitative fitting, as the final 90° readout caused each Look-Locker data set to be independent, removing the requirement for an iterative fit across dynamics. Further an additional sinc pre- and post-saturation RF pulse was applied to the imaging slices immediately before and after the inversion pulse (Fig. 7.1)¹ to further suppress the effect of any inversion pulse imperfections. Also additional spoilers were employed following the inversion pulses and after each read out pulse along all three axes (frequency, phase and slice selection) to suppress any remaining transverse magnetisation.

Four healthy volunteers gave informed consent and participated in a visual activation experiment on two separate days. The visual stimulus was an 8 Hz bright red LED light which was shone at the eyes through light pipes for 4.8 s separated by 26.4 s of rest and repeated 31 times (Experiment 1) or 9.6 s separated by 50.4 s of rest and repeated 16 times (Experiment 2). Initially 3 LL-FAIR dummy volumes were acquired in order to allow for T_1 saturation effects. An odd number of LL-FAIR acquisitions were made per stimulus cycle, resulting in the experiment being jittered to give an achievable effective temporal resolution of 2.4 s.

¹This study was conducted prior to WET pulses being coded on the 3 T Achieva Philips scanner

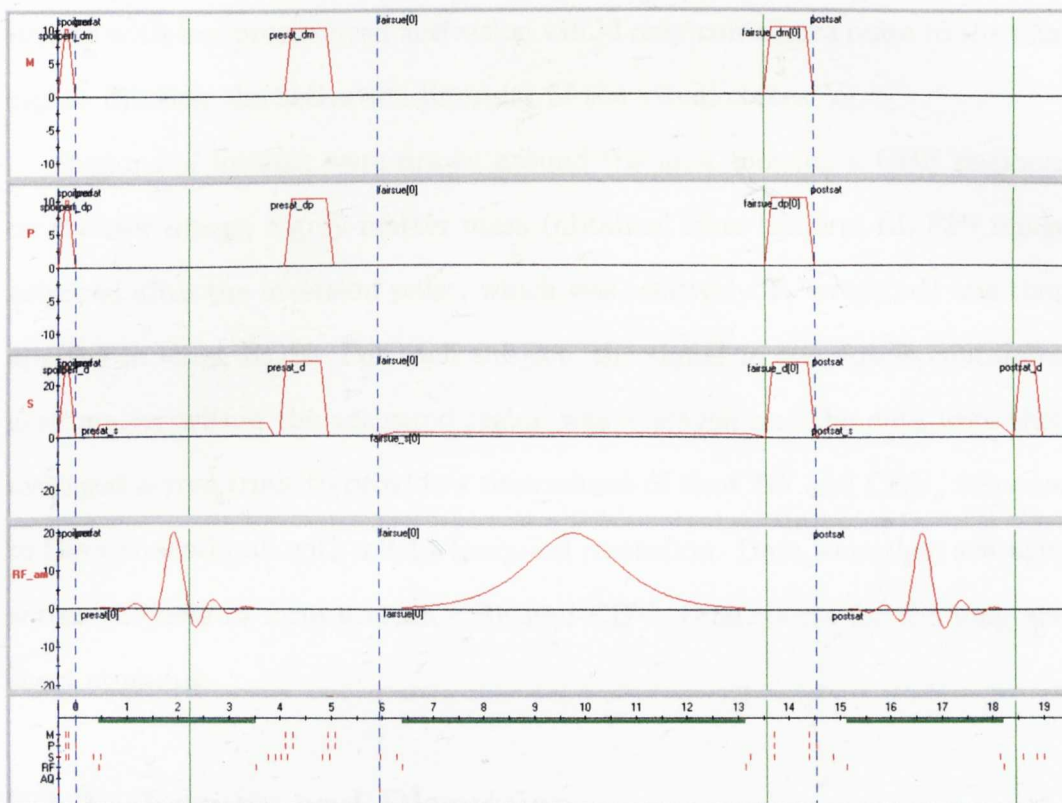


Figure 7.1: FAIR labelling scheme used in this study, simulated with the Philips AcqSim: selective inversion pulse with pre- and post-saturation sinc pulse. Measurement (M), phase (P), and slice selection (S) directions of the gradients and RF pulse profile are shown as a function of time [ms]. For the pulse sequence diagram of the LL-readout scheme see Chapter 6

Although LL-FAIR data can be fitted for CBF or CBV_a , the aim of the Experiments 1 and 2 was to form high SNR CBF and CBV_a weighted data by co-adding the signal from the different LL-EPI readout pulses in a single train following each inversion pulse. These co-added images could then be examined over the time course of the visual stimulation. Difference images (from the subtraction of consecutive selective and non-selective pairs) were then calculated to give a time series of CBF and CBV_a weighted images. For the CBF data the images from all five readout pulses were co-added, as all five TIs clearly contributed to the difference signal. For the CBV_a data, only four images (TI between 150 and 850 ms depending on subject) showing the greatest signal change in the unaveraged difference images were co-added. Using more

images with less pronounced activation would only contribute noise to the final signal, diluting the activation intensity of the visual cortex V_1 .

Regions of interest were drawn around the area showing a CBF response on the raw image, a grey matter mask (obtained from the first LL-EPI image acquired after the inversion pulse, which was relatively T_1 weighted) was then applied to these ROIs. For each subject, the signal in the voxels containing grey matter within the activated region was averaged and the data were then averaged across trials to provide a time course of the CBF and CBV_a response to the visual stimuli with a 2.4 s temporal resolution. Data were then averaged across subjects to form a mean CBF and CBV_a time course for the long and short stimulus.

7.1.2 Results and Discussion

7.1.2.1 CBF

Figure 7.2 shows the CBF weighted images for a single trial image data set of the short (4.8 s ON and 26.4 s OFF) stimulus – no averaging of images across dynamics performed. In Figure 7.2 activation in the visual cortex (V_1)

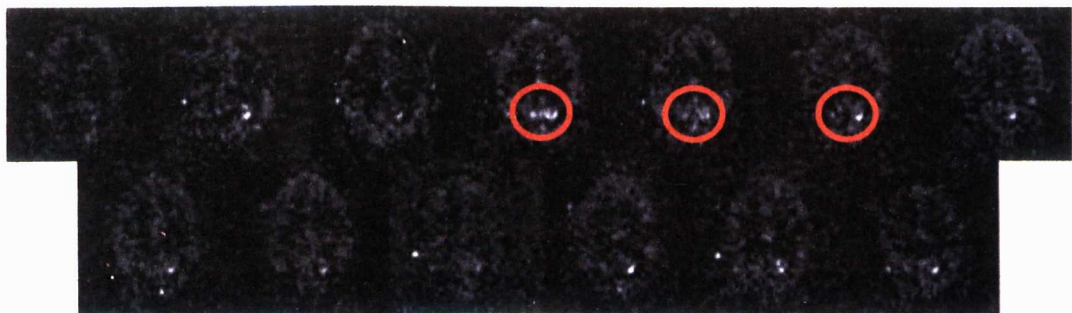


Figure 7.2: Single trial perfusion weighted images acquired on the Philips 3 T Acheiva scanner. Each image represents a 2.4 s time interval time during a single 31.2 s cycle. Stimulus duration was 4.8 s followed by the 26.4 s of rest. Significant activation in the region of interest (marked with red circles) within the visual cortex (V_1) is present in images 4 – 6.

of the grey matter (images 4 – 7) is clearly seen in a single trial (no averaging across dynamics), as marked by the red circles. This data set shows that the signal to noise ratio achieved by using a simple summation of the data from the different LL-FAIR readout pulses allows visual activation to be detected from just a single trial. The reduction of the experimental time that the summation of the LL-EPI readout pulses provides, has potential advantages in allowing us to perform more complex functional studies, for example to study multiple contrast levels.

As expected, averaging over a greater number of cycles will result in a better signal-to-noise ratio. Figure 7.3 displays perfusion weighted images averaged over all 16 cycles (in case of the short stimulus, averaging over all 31 cycles was performed). Images 3 – 7 clearly show the activation of the visual cortex, V_1 , to the stimulus. In general it was found that adequate SNR could be obtained by averaging only 10 CBF weighted data sets.

Further statistical analysis focused on the grey matter of V_1 of the visual cortex, masking out the remaining part of the brain. Figure 7.4 shows the CBF normalised percentage intensity change averaged within the region of interest for the short (a) and long (b) stimulus. For ease of comparison both graphs are shown on the same time scale. Normalisation was performed relative to a baseline period from the last four data points in the cycle (resting state). The four coloured curves correspond to the signal intensity of individual subjects, the black curve in each panel shows the average response over all subjects. For both stimuli, there is one subject (Subject 2 in Fig. 7.4(a) and Subject 3 in Fig. 7.4(b)) that deviates from the response characteristic. There can be a number of reasons for such a difference which will be discussed later (see Section 7.1.3).

The increase in signal in CBF response to the visual stimulus can be seen to commence between 4.8 and 7.2 s after initiation of the stimulus. Maximum

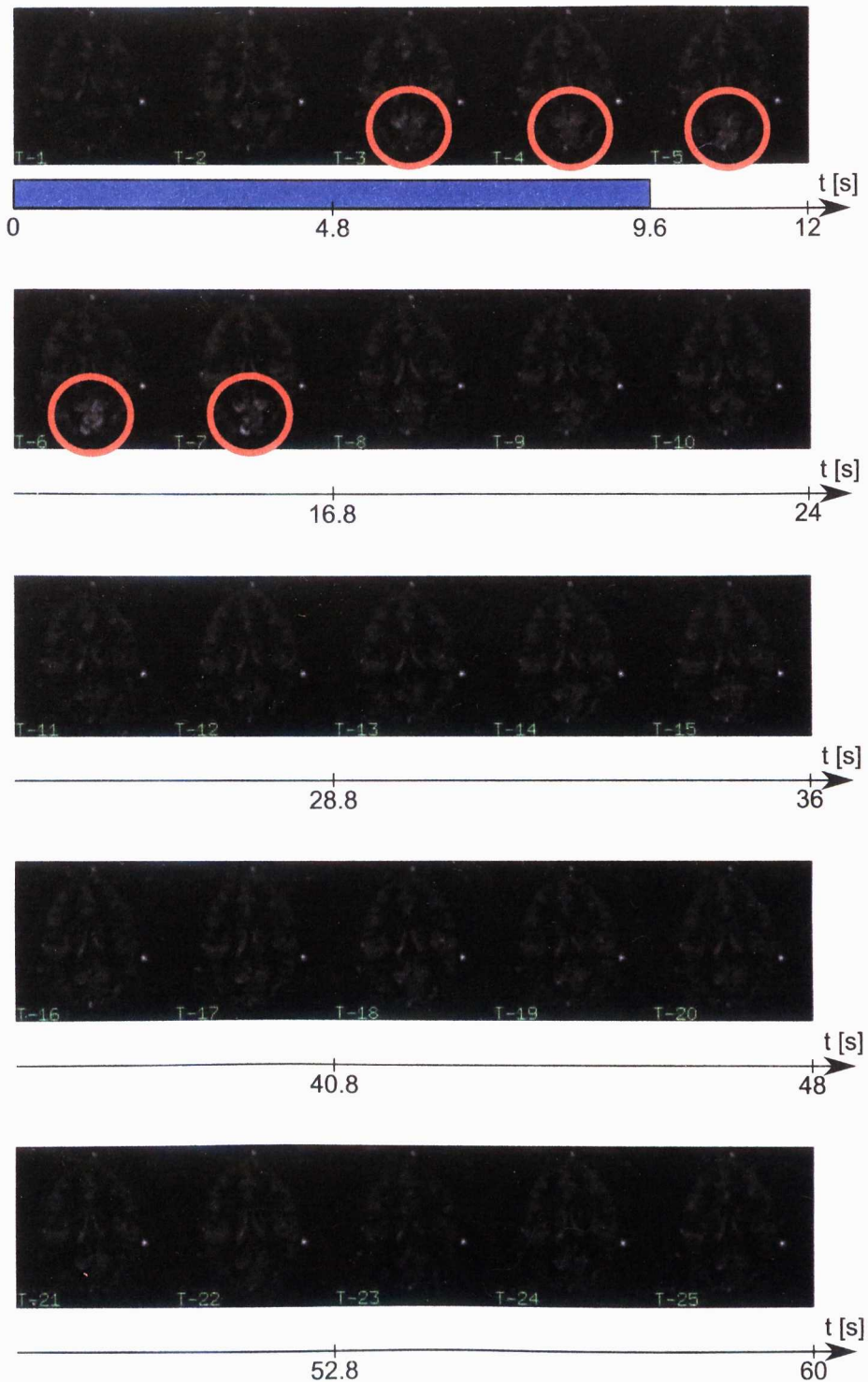


Figure 7.3: Subtracted and averaged *in vivo* images of a visual cortex V_1 acquired on the Philips 3 T Achieva scanner. Each image represents 2.4 s interval time in the functional cycle. Stimulus duration was 9.6 s (marked with the blue box on the time axis) followed by the 50.4 s of rest. Area containing grey matter with the highest activation is marked with the red circles.

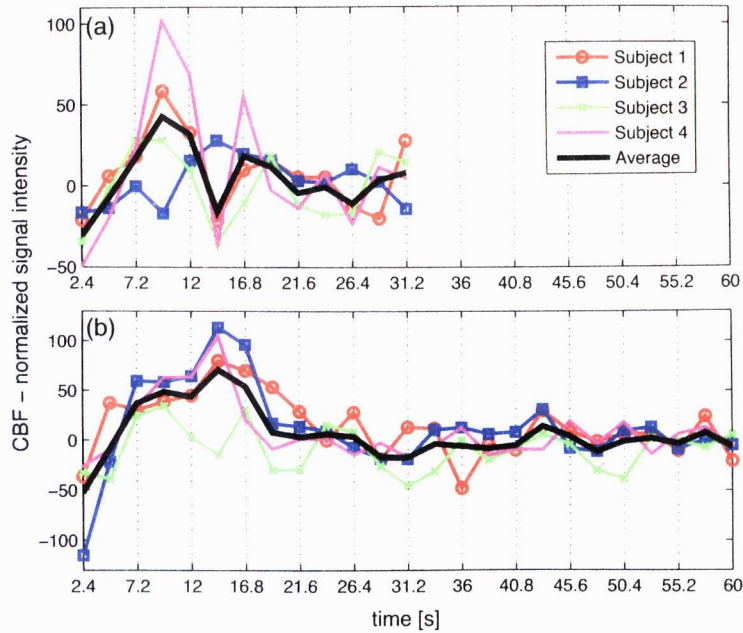


Figure 7.4: Percentage CBF response of the visual cortex V_1 to the short – 4.8 s (a) and long – 9.6 s (b) stimulus for all the subjects (coloured lines). The response was measured based on the averaged pixels’ intensity of the region of interest. The ROI was masked to consider only grey matter voxels. The black line in each panel represents the average response over all subjects.

intensity for the short stimulus is reached in the vicinity of 9.6 s (Fig. 7.4(a)). For the long stimulus there seem to be two maxima, the first at approximately 9.6 s as in the short stimulus case, and the second, dominating peak, at approximately 14.4 s. The existence of the first maximum, even though well pronounced, is still a subject to further investigations. The CBF percentage changes observed are consistent with those in the literature [75] and show a similar degree of variability for these stimuli. Miller found that whilst the sensorimotor cortex showed a nearly linear flow response with increased stimulus duration, a strong nonlinear flow response was observed in the visual cortex.

Figure 7.5 combines the average CBF response over all subjects for both short and long visual stimulus.

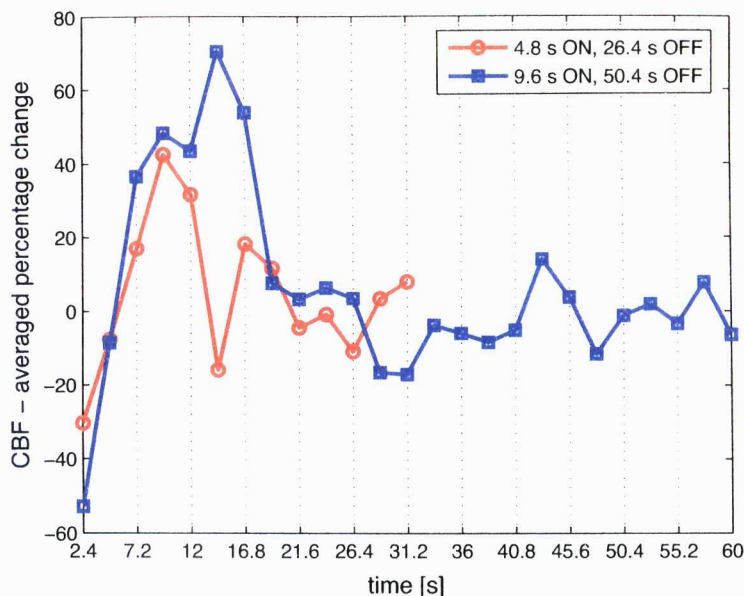


Figure 7.5: Comparison of the averaged percentage CBF responses for the short – 4.8 s (red curve) and long – 9.6 s (blue curve) stimulus.

7.1.2.2 CBV_a

We have extended previous work that has measured the change in the CBF haemodynamic response to study two lengths of visual stimuli [75] to measure the change in the CBV_a haemodynamic response to a 4.8 s and 9.6 s stimulus. Figure 7.6 shows the CBV_a percentage intensity change averaged within the V_1 region of interest for the short (a) and long (b) stimulus for all four subjects individually (coloured curves), and the averaged response (black curve). Again, results from the two (same as for CBF) subjects deviate in a small degree from the other characteristics. The maximum signal appears to peak at the same time (about 7.2 s) for both the short and long stimulus. After reaching the maxima, the short stimulus experiment indicates a quicker and much steeper decrease in the relative CBV_a signal (Fig 7.6(a)), while signal drops more gradually for the longer duration stimulus.

Figure 7.7 combines the average percentage intensity changes in the CBV_a responses over all subjects for both short and long visual stimuli averaged.

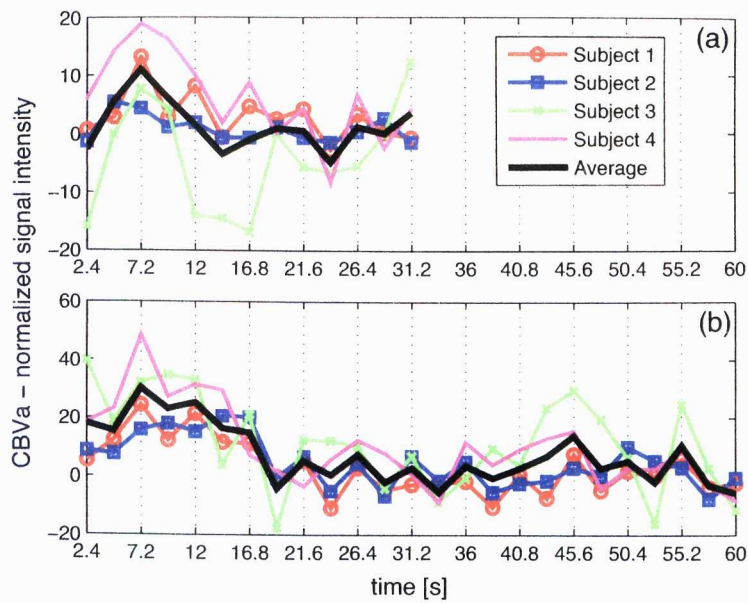


Figure 7.6: Percentage CBV_a response of the visual cortex V₁ to the short – 4.8 s (a) and long – 9.6 s (b) stimulus for all the subjects (coloured lines). The response was measured based on the averaged pixels' intensity of the region of interest. ROI was masked to consider parts with high vessels concentration. The black line in each panel represents the average response over all subjects.

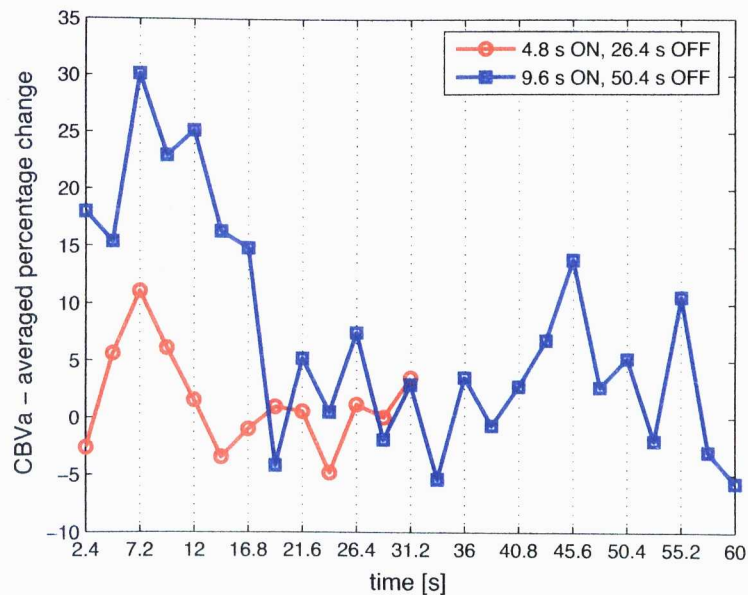


Figure 7.7: Comparison of the averaged percentage CBV_a responses for the short – 4.8 s (red curve) and long – 9.6 s (blue curve) stimulus.

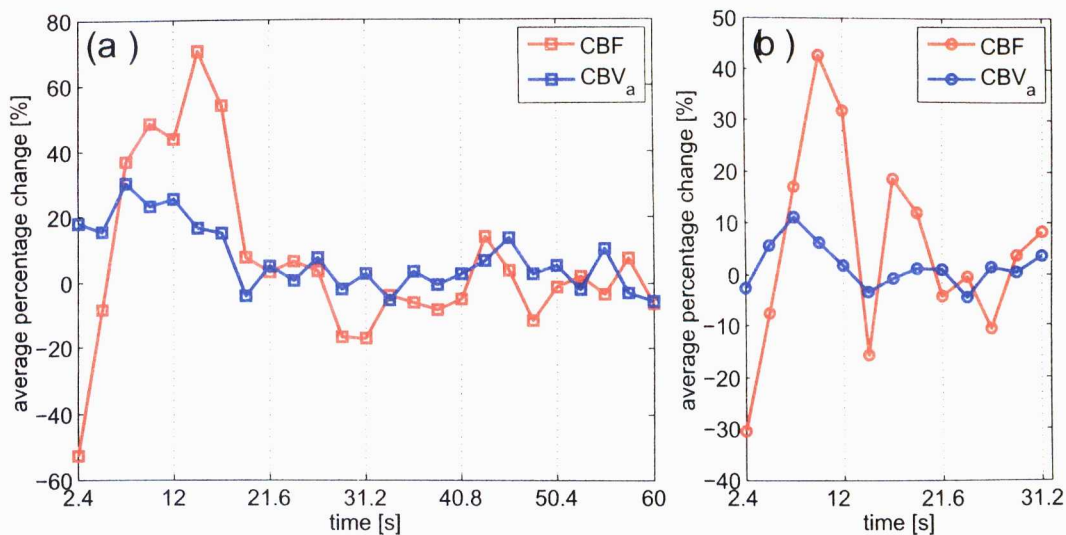


Figure 7.8: Time courses of the percentage in CBF (red curve) and CBV_a (blue curve) responses to the long – 9.6 s (a) and short – 4.8 s (a) stimulus.

Figure 7.8(a) and (b) shows the CBF and CBV_a data plotted together for the long and short stimulus durations, respectively. From the graphs it can be seen that the first peak in CBV_a change leads that in CBF, supporting the idea that CBV_a is the driving function for the CBF response. As expected, the changes in the relative CBV_a precede CBF changes, based on the time of maximal signal changes.

7.1.3 Conclusions

This study has shown that by using LL-FAIR, and summing over the read-out pulses, sufficient SNR can be achieved even from a single trial to assess the temporal response of CBF and CBV_a changes to both short and long duration visual stimuli. The CBV_a response is shown to lead that of CBF weighted signal, demonstrating the CBV_a changes act as a driving input function. These haemodynamic measures are important input parameters to measure, for example to assess input parameters to the BOLD effect such as the Balloon Model [74] and this is the focus of the following study in this chapter.

7.2 Functional Changes in CBV_a , CBF and contrast enhanced CBV_{tot}

The temporal dynamics of the BOLD response are determined by the haemodynamic parameters of cerebral blood flow (CBF), cerebral blood volume (CBV), both arterial and venous, and the oxygen extraction fraction ($CMRO_2$). BOLD contrast depends on deoxygenated blood in the venous blood volume, which is driven by CBF changes which are themselves driven by changes in arterial CBV. This represents the resistance to blood flow through capillary network. However there is only a limited number of published studies that examine the relationship between these haemodynamic input parameters [103–106]. This is largely due to a lack of suitable measurement techniques to assess changes in each of the parameters.

Few groups have studied arterial cerebral blood volume, most studies have used gadolinium based contrast agents to measure changes in total CBV and assumed that this provides a measure of venous CBV, with arterial blood changes being neglected. However, this assumption is unlikely to be true though it is still unclear as to what proportion of arterial and venous blood volume changes contribute to the total blood volume change and the BOLD response. Since venous blood volume comprises about 60 – 80% of total blood volume, to date, most biomechanical models of vascular response, such as the origin Balloon Model [74], have assumed that venous CBV (CBV_v) changes dominate. However, vascular physiology studies suggest that local and upstream arterial vessels dilate during increased neural activity [107] and this has been supported by recent MR studies [92]. Attempts are now being made to measure venous CBV directly, and the VERVE method [108, 109] has been suggested for this. This method uses the dependence of apparent T_2 of blood CPMG (Carr-Purcell Meiboom-Gill) refocusing interval to separate blood and

tissue signals. This sequence uses the intravascular BOLD T_2 effect of venous blood to modulate the blood signal. However, if the tissue signals show any dependence on refocusing intervals that will also contribute to the VERVE signal.

In the absence of a technique to measure venous CBV directly it is possible to measure total CBV (CBV_{tot}). One method to do this which was previously performed at the SPMMRC (Sir Peter Mansfield Magnetic Resonance Centre) was to use an infusion of paramagnetic contrast agent (PROHANCE), giving an increase in contrast agent with time [110–112] to measure the fractional change in CBV_{tot} during a stimulus. A key limitation of this technique was an inability to measure total CBV changes quantitatively. Quantitative maps of resting CBV_{tot} have long been produced by bolus tracking methods [113]. By combining the fractional change in CBV_{tot} (ΔCBV_{tot}) with the bolus tracking method, quantitative changes in CBV_{tot} can be measured.

The objective of this study is to measure changes in perfusion (CBF), arterial CBV (CBV_a) and total CBV (CBV_{tot}) to a visual stimulus, and assess the relation between these three haemodynamic responses. The LL-FAIR technique is used to provide a method to quantify changes in both CBF and CBV_a [96, 97]. To measure total CBV a bolus injection of contrast agent is used. This agent is excreted through the kidneys providing an exponential reduction in concentration, with a half life of about 40 minutes. From this it is possible to measure the change in BOLD signal intensity in response to the change in intravascular contrast agent concentration and thus ΔCBV_{tot} .

Data from this study will allow Grubb's power-law [101] to be assessed for neuronal activation. Grubb's quantitative relationship between CBF and CBV_{tot} has been taken to follow the power-law relationship:

$$CBV_{tot} = 0.80 \cdot CBF^{0.38}. \quad (7.1)$$

However, this was derived for primate data during hypercapnia and under steady state conditions. A hypercapnic challenge causes global changes in haemodynamics, and it is likely that this will result in a very different response to the local effects of dilation and oxygen extraction that occur on neuronal activation. Grubb's power-law is extensively used in calibrated BOLD [87,88] and yet its application in situations of dynamic changes is thus questionable [74], and a matter of current debate.

7.2.1 Experimental Methods and Analysis

Data were acquired on a Philips Achieva 3 T system, equipped with a volume transmit coil and an 8 channel SENSE receive coil. For all three haemodynamic parameter measurements a resolution of $(3 \times 3 \times 5 \text{ mm}^3)$ and SENSE acceleration of 2 were used. At the time of these studies, the LL-FAIR acquisition to measure CBF and CBV_a was limited to a single slice acquisition, therefore an initial functional localiser scan was performed in order to select an axial single slice through the visual cortex with the largest region of BOLD activation. This geometry was then used throughout the rest of the experiment.

Visual stimulation was provided by red LED goggles flashing at 8 Hz. Lights were ON for the first 19.2 s of each 60 s cycle. The number of stimulus cycles varied between modalities reflecting the differing SNR of each method. For CBV_a measurements 8 cycles were collected; for CBF, which has lower CNR, 12 cycles were collected (see Section 7.1) and for CBV_{tot} 14 cycles were collected.

A LL-FAIR acquisition was used for both CBF and CBV_a measurements. The sequence parameters for the CBF measurement were an inversion delay $TI = 600 \text{ ms}$, time interval between EPI readouts $TA = 350 \text{ ms}$, flip angle $\theta = 35^\circ$ and 5 readout pulses with vascular crushing (bipolar lobe of 5 ms

duration per lobe and amplitude of $15 \frac{mT}{m}$). For the CBV_a measurement the parameters were $TI = 150$ ms, $TA = 100$ ms, $\theta = 50^\circ$, with 19 readout pulses. In both CBF and CBV_a measurements the shortest achievable echo time of 16 ms was used and the final LL-FAIR pulse had a flip angle of 90° to maximise SNR. The LL-FAIR scheme was performed with in-plane pre- and post-saturation pulses to provide signal suppression of the imaging slice to reduce any offset signals due to imperfections between the selective and non-selective pulses. The application of a 90° pulse at the end of each TR simplified the fitting as each tag/control remained independent, removing the need for an iterative fit. The TR between inversion pulses was 2.4 s, giving a tag/control pair every 4.8 s. The thickness of inversion slab was alternated between 30 mm and 200 mm for tag and control conditions, respectively.

For the measurement of CBV_{tot} dual-echo GE-EPI images were acquired with $TE = 13 \mid 35$ ms. A TR of 1.2 s was used in order to better characterise the first pass of the bolus of contrast agent. Contrast agent injections consisted of two single doses of ProHance (Bracco Imaging Spa). The first bolus was injected at the beginning of the 5th stimulus cycle and the second at the beginning of the 6th cycle. For these cycles (5 and 6), the visual stimulus was not presented to preserve the analysis from being confounded by the BOLD response. Resting CBV_{tot} was measured from the first and second bolus and was found to increase the blood contrast agent concentration to approximately 1 mM. The final 8 cycles of visual stimulus were acquired at different contrast agent concentration levels as the contrast agent washed out allowing ΔCBV_{tot} to be measured.

Eight healthy volunteers gave written consent and were scanned as part of this study (approved by the local ethics committee). The age range was from 20 to 31 years (mean 24, standard deviation 3).

CBF, CBV_a and BOLD data sets were first realigned. Realignment was

performed first within each data set and then across all data sets for each subject using SPM with a standard algorithm (5 mm FWHM Gaussian smoothing kernel and 2nd Degree B-Spline interpolation). For the CBF and CBV_a data, the last LL-FAIR readout pulse (90° flip angle) of the data set was realigned, and the transforms then applied to the other readout pulses within that TR period. The CBV_{tot} data were realigned using the first echo and the transforms applied to the second echo data. The average time series of the signal changes due to CBF, CBV_a and CBV_{tot} were then formed by averaging across cycles, accounting for jittering, to produce a time series with 2.4 s temporal resolution. This data was then fitted on a voxel-by-voxel, time point-by-time point basis. CBF-weighted and CBV -weighted images were formed by summing over the LL-EPI readout pulses (as described in Section 7.1).

Data sets were also quantified for CBV_a using a two-parameter fit, as previously described [96], to measure changes in arterial transit time and CBV_a . CBF data were initially analysed using a two-parameter fit for capillary transit time and CBF [97]. However since the data had lower SNR than the CBV_a data, a two parameter fit for each time point was found to increase the noise in CBF measures. Therefore instead, a mean estimate of the transit time at rest and on activation was computed, and the data for these states then fitted to a one parameter fit assuming these estimates.

CBV_{tot} data sets were quantified by Dr. N. Blockley. The first pass bolus transit of the contrast agent was used to determine the resting absolute CBV_{tot} [114]. This was achieved by first selecting an Arterial Input Function (AIF) by averaging together the time courses of several voxels within large arteries. A gamma variate function was then fitted to the AIF and each tissue voxel of the brain [113]. The area under the curve was then calculated for each tissue voxel and normalised by the area under the AIF curve. The relative change in CBV_{tot} was calculated by considering the effect of a steady

state concentration of contrast agent on the R_2^* changes that occur during the BOLD response. Previously this was achieved with the aid of an infusion [112]. However, here two bolus injections of contrast agent were used to reach an initial blood contrast agent concentration. Visual stimulation was continued from this point as the contrast agent was washed out through the kidneys. Instead of a continually increasing concentration, as in the case of an infusion, in this experiment the concentration was gradually decreasing. In all other aspects this method is the same as in previous reports [112].

Activation regions for CBV_a , CBF and CBV_{tot} were then generated using a correlation analysis applied to their respective quantified data sets, on a voxel-by-voxel basis. Statistical maps were then thresholded at a z-score of 2.31, $p < 0.02$ to form binary region-of-interest masks. These ROI masks were then combined to form a mask of activated voxels common to CBV_a , CBF and CBV_{tot} . The use of a common ROI was chosen to enhance specificity to microvasculature, therefore we could assume that we are looking at relationship between haemodynamic variables with the same vascular components.

Grubb's constant was then calculated for neuronal activation assuming the relationship between CBV_{tot} and CBF, as previously assessed for hypercapnia [101]

$$CBV_{tot} = \zeta CBF^\alpha, \quad (7.2)$$

where ζ is a constant based on the gradient offset and estimated to be ($\zeta = 0.80$). Differentiating this equation then gives

$$\frac{\Delta CBV_{tot}}{CBV_{tot}} = \alpha \frac{\Delta CBF}{CBF} \quad (7.3)$$

where each side of the equation represents the percentage change in CBV_{tot} and CBF respectively. Since venous blood volume change is driven by CBF which is itself driven by CBV_a , here the relationship between CBF and CBV_a

was assumed to be described by

$$\frac{\Delta CBF}{CBF} = \alpha_{FA} \frac{\Delta CBV_a}{CBV_a}. \quad (7.4)$$

The relationship between CBV_{tot} and CBV_a was also assumed:

$$\frac{\Delta CBV_{tot}}{CBV_{tot}} = \alpha_{TA} \frac{\Delta CBV_a}{CBV_a}, \quad (7.5)$$

Grubb's constant, α , as well as α_{FA} and α_{TA} , can then be estimated from linear fits of relative change in total cerebral blood volume, cerebral blood flow and arterial cerebral blood volume. Data was analysed in two ways.

1. inter-subject estimates of α ; mean steady-state change in CBF, CBV_a and CBV_{tot} were estimated for each subject, and each subject's data plotted on a single graph
2. for each subject each data point in the time series was used to form a linear fit of relative change in haemodynamic parameters and hence estimate α on a subject-by-subject basis:
 - (a) CBV_a and CBF weighted data were plotted and used to estimate α , α_{FA} and α_{TA} ; values were then averaged across the 7 subjects (to form an estimate of "average α ");
 - (b) fitted values of CBV_a and CBF were used to estimate α , α_{FA} and α_{TA} , and then averaged across the 7 subjects (to form an estimate of "average α ");
 - (c) all quantified data points for all subjects were combined into a single fit and the value of α , α_{FA} and α_{TA} estimated (this α is referred to as the "average image α ").

7.2.2 Results

In Figure 7.9 (a-c) shows the masked ROIs for CBV_{tot} , CBF and CBV_a activation maps (blue) for one subject (Subject 6), and the common ROI of the three haemodynamic measures are shown overlaid (red). Below, Fig. 7.9(d), the corresponding time course for each haemodynamic response for the common (dashed lines) and individual ROIs (solid lines) are shown.

Table 7.1 shows the numbers of activated voxels for each of the haemodynamic responses for each individual subject and the size of common ROI for individual subjects. Subject 8 was excluded from further analysis due to lack

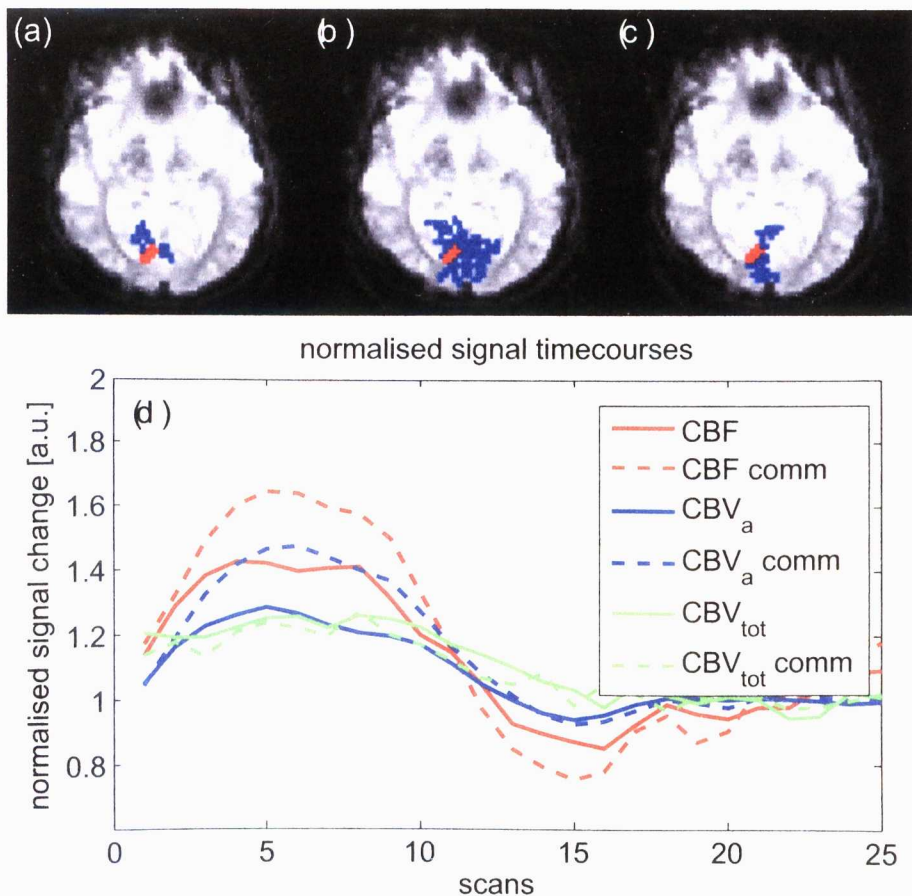


Figure 7.9: Base images with overlaid activated area for CBV_a (a), CBF (b) and CBV_{tot} (c) marked in blue, and common ROI for all three haemodynamic responses, marked in red. Corresponding time courses for each haemodynamic measure for individual regions (solid line) and common ROI (dashed line) are shown below (d).

Table 7.1: Number of voxels of activated ROIs for CBV_a , CBF, CBV_{tot} and common ROI for individual subjects obtained for z-score of 2.31.

Subject	CBV_a	CBF	CBV_{tot}	common ROI
1	8	22	42	1
2	35	41	21	6
3	19	80	104	6
4	12	5	11	2
5	23	70	10	1
6	33	107	45	9
7	60	77	22	10
8	5	13	21	0

of a common activated ROI.

Figure 7.10(a) shows the steady state Grubb relationship (ΔCBV_{tot} vs. ΔCBF), formed from the inter-subject data. The gradient of each linear fit equals the steady state α (α_{FA} and α_{TA}) according to Grubb's power-law. The other assessed relationships of ΔCBV_a are shown in Figure 7.10(b) and (c). The fits of (α , α_{TA} and α_{FA}), are presented in Table 7.2. There can be seen to be a large scatter in the data points likely to result from the variability in ROI placement across subjects, as will be discussed later.

The results of fitting each time point (method 2) were then used to esti-

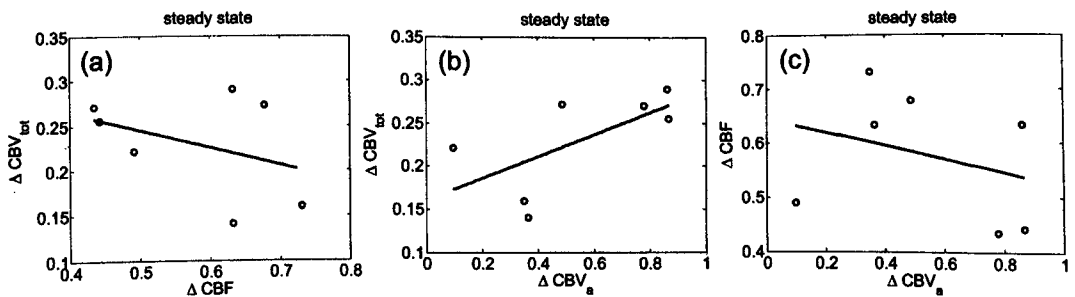


Figure 7.10: Steady state Grubb's constant $\alpha = -0.09$ (ΔCBV_{tot} vs. ΔCBF) across seven subjects (a) and equivalent relations for $\alpha_{TA} = 0.15$ (ΔCBV_{tot} vs. ΔCBV_a) (b) and $\alpha_{FA} = -0.27$ (ΔCBF vs. ΔCBV_a) (c).

mate Grubb's constant on an individual subject basis. In this way the data includes both dynamic and steady state changes in the three haemodynamic measures. Figure 7.11 shows plots to determine the dependency between changes in ΔCBV_{tot} and ΔCBF (Grubb's constant α [101]) for each of the seven subjects for their common ROI of functionally activated CBF, CBV_a and CBV_{tot} . The last panel in Figure 7.11 shows the same plot for the time courses averaged across all subjects. It should be noted that the clusters of points at the minima and maxima of the axes represent the steady state signals. These plots indicate both steady state (far points) and dynamic changes (intermediate points). Although for some subjects the data is very scattered there is no indication that the relationship is not linear (i.e. that α changes under dynamic conditions). Figures 7.12 and 7.13 represent the same plots for α_{FA} and α_{TA} for each subject and their averages are again presented.

Table 7.2 shows Grubb's constant values for each subject for α (CBV_{tot} vs. CBF), α_{TA} (CBV_{tot} vs. CBV_a) and α_{FA} (CBF vs. CBV_a) respectively. Values are presented firstly for the CBF and CBV_a weighted data and secondly for quantitative fits. It can be seen that the estimates of α are similar between these methods (methods 2(a) and 2(b)).

7.2.3 Discussion

This study has combined the measurement of CBF, CBV_a and CBV_{tot} in individual subjects in a single experimental session to assess the coupling of neurovascular responses as determined by their Grubb's constant (α , α_{FA} and α_{TA}). The use of LL-FAIR has allowed the measurement of CBF and CBV_a accounting for transit time effects and in a reasonable experimental time. Using inter-subject data to estimate Grubb (method 1) was found to introduce a large scatter and poor linear fits. Fitting each temporal data point for each individual subjects was found to result in improved linear fits. Using this

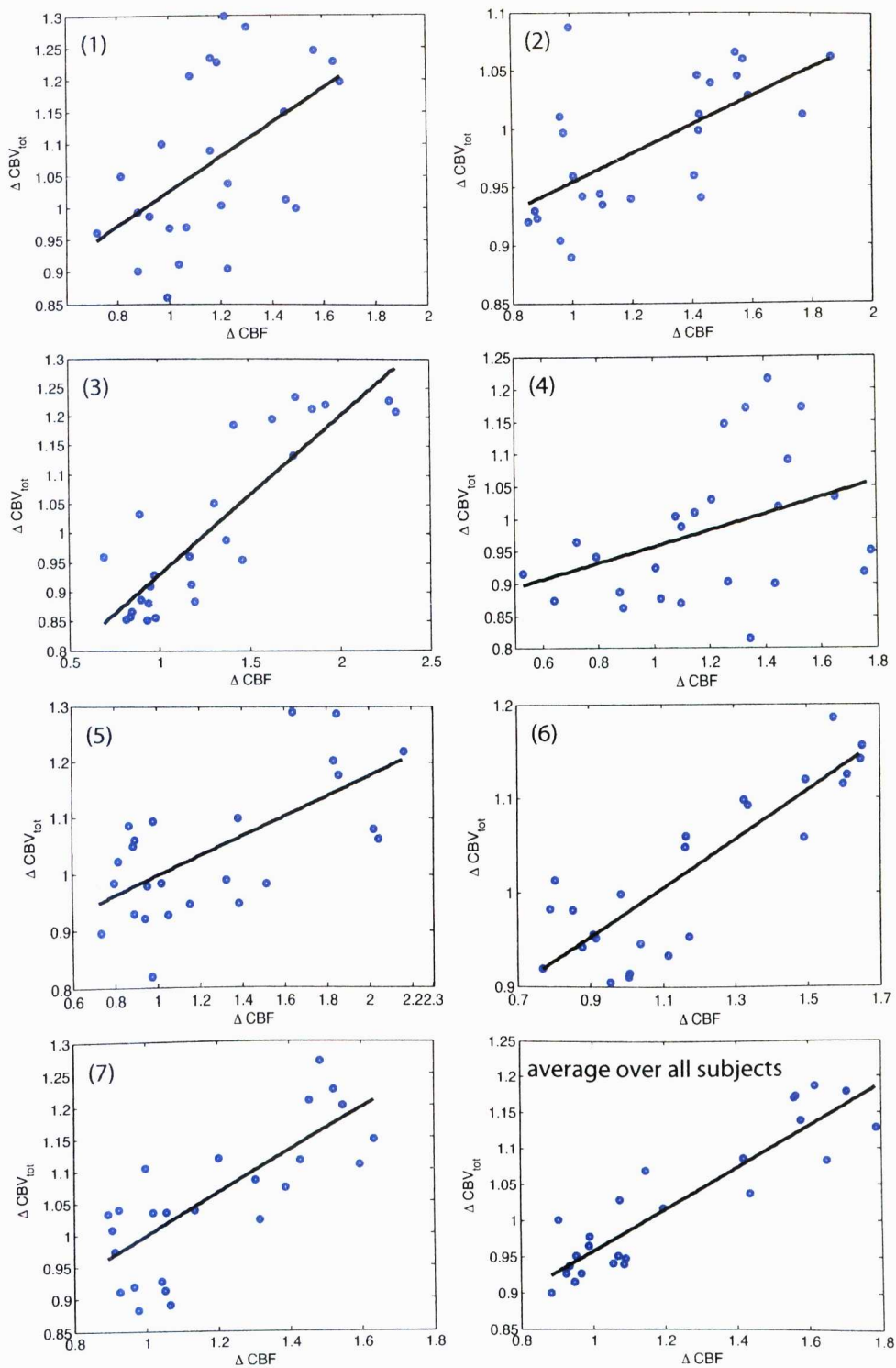


Figure 7.11: Absolute change in CBV_{tot} as a function of absolute change in CBF for subjects 1 – 7. Last panel represents the average of all the subject.

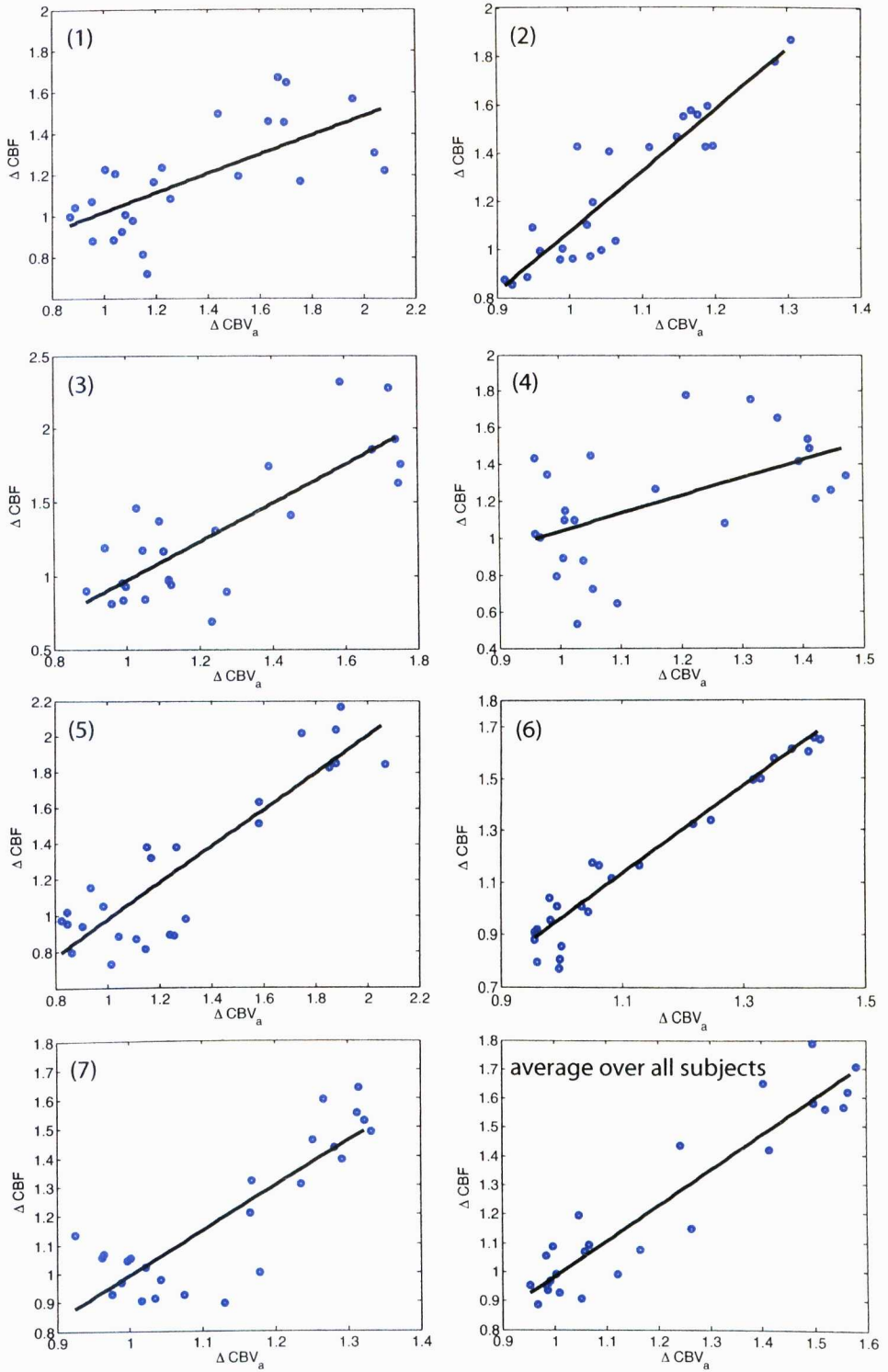


Figure 7.12: Absolute change in CBF as a function of absolute change in CBV_a for subjects 1 – 7. Last panel represents the average of all the subject.

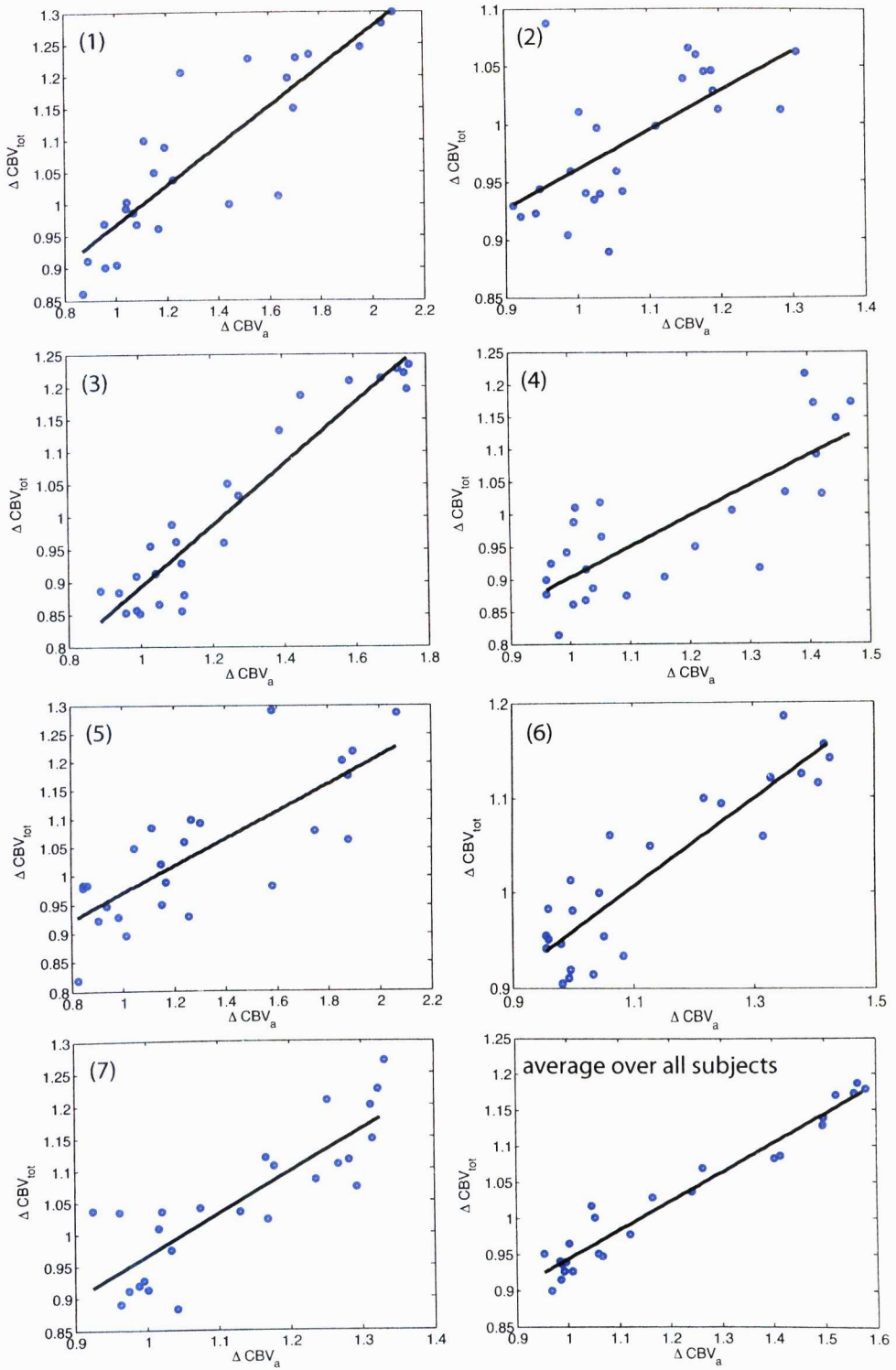


Figure 7.13: Absolute change in CBV_{tot} as a function of absolute change in CBV_a for subjects 1 – 7. Last panel represents the average of all the subject.

Table 7.2: Calculated dependencies for linear approximation: $\Delta CBV_{tot} = \alpha \cdot \Delta CBF$, $\Delta CBV_{tot} = \alpha_{TA} \cdot \Delta CBV_a$ and $\Delta CBF = \alpha_{FA} \cdot \Delta CBV_a$.

Subject	change in signal			quantitative change		
	α	α_{TA}	α_{FA}	α	α_{TA}	α_{FA}
1	0.30	0.21	0.34	0.27	0.31	0.47
2	0.13	0.30	1.79	0.12	0.34	2.48
3	0.30	0.30	0.72	0.27	0.47	1.30
4	0.06	0.20	0.45	0.13	0.47	0.96
5	0.18	0.28	1.27	0.18	0.24	1.03
6	0.27	0.44	1.51	0.25	0.46	1.69
7	0.36	0.34	0.77	0.33	0.65	1.52
average α	0.23	0.30	0.98	0.22	0.42	1.35
STDev	± 0.11	± 0.08	± 0.55	± 0.08	± 0.14	± 0.64
average image	0.31	0.29	0.81	0.29	0.40	1.21

method, classical Grubb's constant, α , was found to be 0.26 ± 0.11 or 0.34 when fitted across all subjects. This value is in a good agreement with the value of the Grubb's constant originally estimated ($\alpha = 0.38$) [101], which was based on a steady state measurement of global changes in non-human primates using hypercapnia-based modulation, with CBF data acquired using PET. This relation has been a fundamental approximation used in many studies of calibrated BOLD and oxygen consumption $CMRO_2$ [88, 115, 116], blood volume and perfusion using hypo- | hyper-capnic modulations and other functional stimuli throughout the years. Since the original study by Grubb, several groups have assessed this power-law with varying results; $\alpha = 0.40$ during hypercapnia [35], $\alpha = 0.3$ [117] and 0.29 [118] in PET studies based on visual stimulation and hypo- | hyper-capnia, respectively. In addition when regional spatial variability in α has been assessed using PET, and a value of 0.64 was found for the cortex compared to 0.46 for subcortical grey matter [119]. It is also worth noting that VERVE found a venous Grubb's constant of 0.23 [108].

The study also allowed the dependency between CBF and CBV_a to be assessed, fitting a linear fit of change in these parameters returned a value of 0.81 ± 0.29 and 1.09 (Table 7.2) for methods 2(b) and 2(c). A similar power-law dependency of CBF to $CBV_a^{1.2}$ was found in rats [35]. Modelling the arteriole as an expanding cylinder [102] would suggest α_{FA} to be 2 for a laminar flow approximation (proportional to r^4 , where “r” is the radius) [76,102,120] and 1 for a plug flow approximation (proportional to r^2) [76,102,120]. However, if a spherical expansion of arterioles would be considered, α_{FA} would be in the vicinity of $\frac{4}{3}$ and $\frac{2}{3}$ for a laminar and plug flow model, respectively.

Simultaneous measurement of CBV_{tot} , CBF and CBV_a has not previously been conducted in humans. Until recently it was believed that blood volume changes arise from the venous compartment. However, this and other recent studies now suggest that CBV_a contributions play a large role. Considering the relation that $CBV_{tot} = CBV_a + CBV_v$ (where CBV_v is the venous CBV), an increase of volume in the arterial compartment to be α_a and $\alpha_a \cdot k$ represents the increase of volume in the venous compartment, then the absolute changes in CBV_{tot} and CBV_a can be expressed as:

$$\Delta CBV_{tot} = \frac{\alpha_a(1+k)}{CBV_{tot}} \quad \text{and} \quad \Delta CBV_a = \frac{\alpha_a}{CBV_a}. \quad (7.6)$$

The ratio of changes in CBV_{tot} to changes in CBV_a can be described as:

$$\frac{\Delta CBV_{tot}}{\Delta CBV_a} = (1+k) \frac{CBV_a}{CBV_{tot}}, \quad (7.7)$$

where $\frac{\Delta CBV_{tot}}{\Delta CBV_a} = \alpha_{TA}$. We can then describe “k” as:

$$k = \alpha_{TA} \frac{CBV_{tot}}{CBV_a} - 1. \quad (7.8)$$

Since quantitative estimates of all three haemodynamic responses (CBV_{tot} ,

Table 7.3: Calculated “k” values for all subjects.

Subject	$CBV_{tot} \left[\frac{ml}{100g} \right]$	$CBV_a \left[\frac{ml}{100g} \right]$	arterial contribution [%]	k
1	24.44	3.01	12	1.68
2	9.18	3.78	41	-0.63
3	3.08	3.94	128	-0.70
4	5.16	8.86	172	0.71
5	4.53	2.07	46	-0.27
6	5.33	6.91	130	0.31
7	7.06	5.83	83	-0.72

CBF , and CBV_a) and their changes were measured above, data from the common ROI can be used to estimate $\frac{CBV_{tot}}{CBV_a}$, the contribution of arterial blood volume to total blood volume, and thus calculate “k” .

Table 7.3 lists the absolute resting state values for CBV_{tot} and CBV_a , from which the percentage contribution of arterial blood to total blood volume was calculated, and the corresponding “k” values for each subject, using Eq. 7.8. A large variability in the estimated values of “k” is seen across the seven subjects. For Subject 1 (Table 7.3, Subject 1) “k” > 1 indicating that the venous changes exceed the contribution of arterial changes in the total CBV change. Clearly, in that ROI only a small percentage of the blood is contained within arterioles. For “k” = 1 the changes of both CBV_a and CBV_v would contribute equally to the changes in total CBV. For $0 < \text{“k”} < 1$ the CBV_a changes are larger than the CBV_v (Table 7.3, Subject 6). “k” = 0 would indicate no changes in the venous compartment, therefore the changes in the total CBV would depend entirely on changes in CBV_a . The interesting situation is when “k” < 0 (Table 7.3, Subjects 2, 3, 4, 5 and 7). This can be explained as a negative change in blood volume of the venous compartment driven by the increase of the arterial blood.

The absolute values for both CBV_{tot} and CBV_a carry errors (and this can be seen to result in an arterial contribution of over 100 %, Table 7.3, Subject 3, 4, and 6). Errors may arise in the estimation of CBV_a due to the inaccurate estimation of the M_0 of blood. For the spatial resolution of the data in this study, it is difficult to find a voxel with 100 % blood volume, and so partial voluming effects are likely leading to errors in the M_0 of blood. Errors in CBV_{tot} are likely to arise from the misrepresentation of the AIF. It is expected that the error in CBV_{tot} is greater than that associated with CBV_a . Nevertheless, values of α_{TA} , which play a key role in calculating “k”, are only based on changes in CBV_{tot} and CBV_a , and therefore fairly accurate (for all subjects errors in relative change are less than 5 %, estimated using last 4 points of the baseline signal). Taking the average value of $\alpha_{TA} = 0.42$ (Table 7.2), the venous blood content of a voxel (or an ROI) would have to be over 3.7 times larger than the arterial blood content of the same voxel (or ROI) for the changes in CBV_v to exceed the changes in CBV_a .

Because the ROI chosen in this study for the calculations is common to all three haemodynamic responses, this region should be dominated by small vessel effect, and therefore no draining veins where ballooning may occur were included. Instead, we hypothesise that arterial expansion could actively lead to compression of the venous volume. Previous, non MR data have found no change in CBV_v in response to hypercapnia [36], but for BOLD calibration the component of venous compartment is of key interest. Error in estimating CBV_v will lead to erroneous estimation of $CMRO_2$ change and could have a great impact on cerebrovascular modelling.

7.3 Conclusions

The studies presented in this chapter show applications of the LL-FAIR technique. It has been shown that the qualitative measurements of relative changes in cerebral blood flow and arterial cerebral blood volume can be acquired in a significantly reduced time in comparison to traditional ASL techniques. Averaging over LL-EPI readout pulses (five for CBF and four for CBV_a) results in sufficient signal-to-noise ratio in a single shot acquisition. Time courses and their characteristics were assessed for two durations of visual stimulus. Future work is suggested to perform a multiple-length stimuli in order to find possible dependency. Optimisation of LL-FAIR technique for single shot acquisition can also be performed at the ultra-high field where the SNR is increased.

This chapter also shows the application of LL-FAIR sequences as a part of a larger multi-parameter study. The LL-FAIR sequence was used to obtain CBF and CBV_a data, and in addition a further GE-EPI acquisition was used to measure CBV_{tot} to observe visually induced changes in neurovascular response. Absolute and relative changes were then quantified and various haemodynamic relationships were addressed and compared against the values found in the literature. Values obtained for traditional Grubb's constant α are in reasonable agreement with the power-law relation of $CBV_{tot} = CBF^{0.38}$, although our value was slightly lower. Differences may arise because Grubb's constant was originally measured using PET and will have included very large vessels. For calibrated BOLD this would lead to an over estimate of venous volume contributing to the BOLD effect. Many other studies returned different values of Grubb, also suggesting spatial variation of the power-law. In these studies a broad spectrum of acquired data allowed us to find and discuss relationships between these three haemodynamic responses in order to better

understand neurovascular brain functions. Future work will extend the analysis to form voxel-by-voxel maps of the dependencies between CBV_{tot} , CBF and CBV_a in order to better understand spatial and temporal relations between these haemodynamic responses on visual stimulation.

Chapter 8

Summary

The work described in this thesis was directed towards developing and improving Arterial Spin Labelling techniques to improve MRI brain function mapping. It has been shown that ASL methods can find their applications in medical research, diagnostic medicine as well as in pharmaceutical trials.

In Chapter 5, it was shown that ASL experiments at ultra-high field are challenging; the discovery of a new artefact (characteristic only to Philips Achieva MR scanners and termed the Roman Artefact) was one of the biggest obstacles. To eliminate this artefact, a technique known as Double Acquisition Background Suppression (DABS) was developed. This technique was then combined with the PASL FAIR method, and has proven to not only reduce the influence of the Roman Artefact on images, but also decrease the contribution of cardiac and respiratory induced physiological noise. It was also proven that DABS, by reducing physiological noise at source, has statistically surpassed the RETROICOR method for post-processing removal of physiological noise. Potentially, DABS can be combined with any ASL labelling sequence, thus removing static tissue signal and maintaining its sensitivity to inflowing blood. Simultaneous acquisition of a second stack of high CNR images can provide additional BOLD contrast data or simply be used as a tool for improved re-

alignment of background suppressed images.

The use of the ASL FAIR technique continues to be the core technique for all the experiments throughout this thesis. In Chapter 6, the advantages of combining Look-Locker sampling method with ASL labelling over the traditional, single TI, FAIR acquisition in quantifying CBV_a , are outlined. It was confirmed, that both arterial and arteriolar transit times (Δ and δ , respectively) change on activation and vary on a voxel-to-voxel basis. Although Look-Locker sampling usually requires a complicated quantification process, this work has introduced and verified a simplified model for accurate estimation of CBV_a . LL-FAIR significantly reduces the acquisition time in comparison with an arduous approach of sampling at many TIs separately, as in the traditional FAIR method.

LL-FAIR can be modified for sensitivity to either CBV_a or CBF, therefore it is an excellent tool to study multi-parameter haemodynamics. Chapter 7 assesses the relative changes in arterial blood volume (ΔCBV_a) and blood flow (ΔCBF) in response to visual stimuli. The reduction of the acquisition time over a traditional FAIR technique is emphasised. Qualitative (perfusion weighted) images are obtained from co-adding several LL-EPI readout pulses to significantly increase SNR, making LL-FAIR technique a good candidate for single-trial studies. The second study combines quantitative measurements of CBV_a , CBF, and CBV_{tot} . These data are used to estimate Grubb's constant and to show the flexibility of this method and possibility to extract important information about relationships between these three haemodynamic responses.

Future work will continue the analysis of haemodynamic responses, CBV_a , CBF, and CBV_{tot} , mapping the spatial variability in α , α_{TA} and α_{TA} on a voxel-by-voxel basis. Further studies will pursue a more clinical direction, applying ASL methods in diseased patients with altered cerebral blood volume or perfusion. Also research of comatose patients could benefit from application

of a fast acquisition techniques (patients in a comatose state frequently experience involuntary spastic muscle movements) in assessing basic brain perfusion and haemodynamic responses.

Glossary

AIF	Arterial Input Function
ASL	Arterial Spin Labelling
BBB	Blood-Brain Barrier
BOLD	Blood Oxygenation Level Dependent
CASL	Continuous ASL
CE-MRA	Contrast Enhanced MRA
CBF	Cerebral Blood Flow
CBV	Cerebral Blood Volume
CBV_a	Cerebral Blood Volume (arterial)
CBV_{tot}	Cerebral Blood Volume (total)
CBV_v	Cerebral Blood Volume (venous)
COW	Circle Of Willis
CMRO₂	Cerebral Metabolic Rate of Oxygen (O ₂)
CPMG	Carr-Purcell Meiboom-Gill
CSF	Cerebro-Spinal Fluid
CTA	Computed Tomography Angiography
DABS	Double Acquisition Background Suppression
DSA	Digital Subtraction Angiography
DSC-MRI	Dynamic Susceptibility Contrast MRI
EPI	Echo Planar Imaging
FAIR	Flow-sensitive Alternating Inversion Recovery

FID	Free Induction Decay
FISP	Fast Imaging with Steady-state Precession
FLASH	Fast Low Angle SHot
FOCI	Frequency Offset Corrected Inversion
FT	Fourier Transform
FWE	Family Wise Error
GE-EPI	Gradient Echo EPI
GRASE	GRadient And Spin Echo
HRF	Haemodynamic Response Functions
LL-EPI	Look-Locker EPI
LL-FAIR	FAIR with Look-Locker EPI readout
MCA	Middle Cerebral Artery
MTT	Mean Transit Time
MRA	Magnetic Resonance Angiography
MRI	Magnetic Resonance Imaging
MT	Magnetisation Transfer
NMR	Nuclear Magnetic Resonance
PASL	Pulse ASL
PC-MRA	Phase Contrast MRA
PCASL	Pseudo-Continuous ASL
PET	Positron Emission Tomography
PICORE	Proximal Inversion with a Control for Off-Resonance Effects
PW	Perfusion Weighted
RA	Roman Artefact
RARE	Rapid Acquisition with Refocused Echoes
RF	Radio Frequency
SAR	Specific Absorption Rate
SCM	Step-wise Compartmental Model

SE-EPI	Spin Echo EPI
SNR	Signal-to-Noise Ratio
SPECT	Single Photon Emission Computed Tomography
SPMMRC	Sir Peter Mansfield Magnetic Resonance Centre
STAR	Signal Targeting with Alternating Radiofrequency
TE	Echo Time
TI	Inversion Time
TILT	Transfer Insensitive Labelling Technique
TOF	Time-Of-Flight
TR	Repetition Time
VERVE	VENous Refocusing for Volume Estimation

Bibliography

- [1] J. A. Detre, J. S. Leigh, D. S. Williams, and A. P. Koretsky. Perfusion imaging. *Magn. Reson. Med.*, 23(1):37–45, Jan 1992.
- [2] L. Axel. Blood flow effects in magnetic resonance imaging. *AJR Am. J. Roentgenol.*, 143(6):1157–1166, Dec 1984.
- [3] E. M. Purcell, H. C. Torrey, and R. V. Pound. Resonance absorption by nuclear magnetic moments in a solid. *Phys. Rev.*, 69:37–38, 1946.
- [4] F. Bloch, W. W. Hansen, and M. Packard. Nuclear induction. *Phys. Rev.*, 69:127, 1946.
- [5] M. H. Levitt. *Spin dynamics: basics of nuclear magnetic resonance*. John Wiley & Sons Ltd., 2001.
- [6] C. P. Slichter. *Principles of magnetic resonance*. Springer-Verlag, 1989.
- [7] P. Mansfield and P. K. Grannell. NMR ‘Diffraction’ in solids? *J. Physics D*, 6:422, 1973.
- [8] P. C. Lauterbur. Image formation by induced local interactions: examples employing nuclear magnetic resonance. *Nature*, 242:190–191, 1973.
- [9] P. Mansfield and A. A. Maudsley. Medical imaging by NMR. *Brit. J. of Radiology*, 50:188–194, 1977.

- [10] R. N. Bracewell. *Fourier transform and its applications*. New York: McGraw-Hill, 1978.
- [11] R. S. Likes. Moving gradient zeugmatography. U.S. Patent 4307343, 1981.
- [12] S. Ljunggren. A simple graphical representation of Fourier-based imaging methods. *J. Magn. Reson.*, 54:338–343, 1983.
- [13] P. C. Lauterbur, D. M. Kramer, W. V. House, and C.-N. Chen. Zeugmatographic high-resolution nuclear magnetic-resonance spectroscopy — images of chemical inhomogeneity within microscopic objects. *J. Am. Chem. Soc.*, 97:6866–6868, 1975.
- [14] P. Mansfield, A. A. Maudsley, and T. Baines. Fast scan proton density imaging by NMR. *J. Phys. E.*, 9:271–278, 1976.
- [15] D. I. Hoult. Zeugmatography—criticisim of concept of a selective pulse in presence of a field gradient. *J. Magn. Reson.*, 26(1):165–167, 1977.
- [16] P. Mansfield. Multi-planar image formation using NMR spin echoes. *J. Phys. C: Solid Phys.*, 10:L55, 1977.
- [17] K. K. Kwong, J. W. Belliveau, D. A. Chesler, I. E. Goldberg, R. M. Weisskoff, B. P. Poncelet, D. N. Kennedy, B. E. Hoppel, M. S. Cohen, and R. Turner. Dynamic magnetic resonance imaging of human brain activity during primary sensory stimulation. *Proc. Natl. Acad. Sci. U.S.A.*, 89: 5676–5679, 1992.
- [18] M. K. Stehling, R. J. Ordidge, R. Coxon, and P. Mansfield. Inversion-recovery echo-planar imaging (IR-EPI) at 0.5 T. *Magn Reson Med*, 13 (3):514–517, Mar 1990.

- [19] M. Poole. *Improved Equipment and Techniques for Dynamic Shimming in High Field MRI*. PhD thesis, University of Nottingham, 2007.
- [20] N. P. Blockley. *Investigating the BOLD Haemodynamic Response*. PhD thesis, University of Nottingham, 2007.
- [21] M. Poole and R. Bowtell. Volume parcellation for improved dynamic shimming. *MAGMA*, 21(1-2):31–40, Mar 2008. URL <http://dx.doi.org/10.1007/s10334-007-0102-2>.
- [22] M. J. de Leon, A. E. George, S. H. Ferris, S. Rosenbloom, D. R. Christman, C. I. Gentes, B. Reisberg, I. I. Kricheff, and A. P. Wolf. Regional correlation of PET and CT in senile dementia of the Alzheimer type. *AJNR Am. J. Neuroradiol*, 4(3):553–556, 1983.
- [23] L. R. Schad, R. Boesecke, W. Schlegel, G. H. Hartmann, V. Sturm, L. G. Strauss, and W. J. Lorenz. Three dimensional image correlation of CT, MR, and PET studies in radiotherapy treatment planning of brain tumors. *J. Comput. Assist. Tomogr.*, 11(6):948–954, 1987.
- [24] A. Villringer, B. R. Rosen, J. W. Belliveau, J. L. Ackerman, R. B. Lauffer, R. B. Buxton, Y. S. Chao, V. J. Wedeen, and T. J. Brady. Dynamic imaging with lanthanide chelates in normal brain: contrast due to magnetic susceptibility effects. *Magn. Reson. Med.*, 6(2):164–174, Feb 1988.
- [25] D. L. Thomas, M. F. Lythgoe, G. S. Pell, F. Calamante, and R. J. Ordidge. The measurement of diffusion and perfusion in biological systems using magnetic resonance imaging. *Phys. Med. Biol.*, 45(8):R97–138, Aug 2000.
- [26] P. Gillis and S. H. Koenig. Transverse relaxation of solvent protons induced by magnetized spheres: application to ferritin, erythrocytes, and magnetite. *Magn. Reson. Med.*, 5(4):323–345, Oct 1987.

- [27] D. S. Williams, J. A. Detre, J. S. Leigh, and A. P. Koretsky. Magnetic resonance imaging of perfusion using spin inversion of arterial water. *Proc. Natl. Acad. Sci. U.S.A.*, 89(1):212–216, Jan 1992.
- [28] R. R. Edelman, B. Siewert, D. G. Darby, V. Thangaraj, A. C. Nobre, M. M. Mesulam, and S. Warach. Qualitative mapping of cerebral blood flow and functional localization with echo-planar MR imaging and signal targeting with alternating radio frequency. *Radiology*, 192(2):513–520, Aug 1994.
- [29] L. Ostergaard, R. M. Weisskoff, D. A. Chesler, C. Gyldensted, and B. R. Rosen. High resolution measurement of cerebral blood flow using intravascular tracer bolus passages. Part I: Mathematical approach and statistical analysis. *Magn. Reson. Med.*, 36(5):715–725, Nov 1996.
- [30] L. Ostergaard, A. G. Sorensen, K. K. Kwong, R. M. Weisskoff, C. Gyldensted, and B. R. Rosen. High resolution measurement of cerebral blood flow using intravascular tracer bolus passages. Part II: Experimental comparison and preliminary results. *Magn. Reson. Med.*, 36(5):726–736, Nov 1996.
- [31] E. T. Petersen, I. Zimine, Y.-C. L. Ho, and X. Golay. Non-invasive measurement of perfusion: a critical review of arterial spin labelling techniques. *Br. J. Radiol.*, 79(944):688–701, Aug 2006. URL <http://dx.doi.org/10.1259/bjr/67705974>.
- [32] M. A. Bernstein, K. F. King, and X. J. Zhou. *Handbook of MRI Pulse Sequences*. Elsevier Academic Press, 2004.
- [33] G. E. Morgan, M. S. Mikhail, and M. J. Murray. *Clinical Anesthesiology*. The McGraw-Hill Companies, 2002. 615 pp.

- [34] T. Q. Duong, D. S. Kim, K. Uurbil, and S. G. Kim. Localized cerebral blood flow response at submillimeter columnar resolution. *Proc. Natl. Acad. Sci. U.S.A.*, 98(19):10904–10909, Sep 2001. URL <http://dx.doi.org/10.1073/pnas.191101098>.
- [35] S. P. Lee, T. Q. Duong, G. Yang, C. Iadecola, and S. G. Kim. Relative changes of cerebral arterial and venous blood volumes during increased cerebral blood flow: implications for BOLD fMRI. *Magn. Reson. Med.*, 45(5):791–800, May 2001.
- [36] S. K. Piechnik, P. A. Chiarelli, and P. Jezzard. Modelling vascular reactivity to investigate the basis of the relationship between cerebral blood volume and flow under CO₂ manipulation. *Neuroimage*, 39(1):107–118, Jan 2008. URL <http://dx.doi.org/10.1016/j.neuroimage.2007.08.022>.
- [37] J. B. Gonzalez-Atevalas, D. C. Alsop, and J. A. Detre. Cerebral perfusion and arterial transit time changes during task activation determined with continuous arterial spin labeling. *Magn. Reson. Med.*, 43(5):739–746, May 2000.
- [38] Y. Yang, W. Engelen, S. Xu, H. Gu, D. A. Silbersweig, and E. Stern. Transit time, trailing time, and cerebral blood flow during brain activation: measurement using multislice, pulsed spin-labeling perfusion imaging. *Magn. Reson. Med.*, 44(5):680–685, Nov 2000.
- [39] W. T. Dixon, L. N. Du, D. D. Faul, M. Gado, and S. Rossnick. Projection angiograms of blood labeled by adiabatic fast passage. *Magn. Reson. Med.*, 3(3):454–462, Jun 1986.

- [40] L. Maccotta, J. A. Detre, and D. C. Alsop. The efficiency of adiabatic inversion for perfusion imaging by arterial spin labeling. *NMR Biomed.*, 10(4-5):216–221, 1997.
- [41] J. F. Utting, D. L. Thomas, D. G. Gadian, and R. J. Ordidge. Velocity-driven adiabatic fast passage for arterial spin labeling: results from a computer model. *Magn. Reson. Med.*, 49(2):398–401, Feb 2003. URL <http://dx.doi.org/10.1002/mrm.10363>.
- [42] C. Franke, F. A. van Dorsten, L. Olah, W. Schwindt, and M. Hoehn. Arterial spin tagging perfusion imaging of rat brain: dependency on magnetic field strength. *Magn. Reson. Imaging.*, 18(9):1109–1113, Nov 2000.
- [43] H. M. Gach and W. Dai. Simple model of double adiabatic inversion (DAI) efficiency. *Magn. Reson. Med.*, 52(4):941–946, Oct 2004. URL <http://dx.doi.org/10.1002/mrm.20240>.
- [44] R. Trampel, T. H. Jochimsen, T. Mildner, D. G. Norris, and H. E. Miller. Efficiency of flow-driven adiabatic spin inversion under realistic experimental conditions: a computer simulation. *Magn. Reson. Med.*, 51(6):1187–1193, Jun 2004. URL <http://dx.doi.org/10.1002/mrm.20080>.
- [45] E. C. Wong. Vessel-encoded arterial spin-labeling using pseudocontinuous tagging. *Magn. Reson. Med.*, 58(6):1086–1091, Dec 2007. URL <http://dx.doi.org/10.1002/mrm.21293>.
- [46] E. C. Wong, R. B. Buxton, and L. R. Frank. Implementation of quantitative perfusion imaging techniques for functional brain mapping using pulsed arterial spin labeling. *NMR Biomed.*, 10(4-5):237–249, 1997.

- [47] R. J. Ordidge, M. Wylezinska, J. W. Hugg, E. Butterworth, and F. Francini. Frequency offset corrected inversion (FOCI) pulses for use in localized spectroscopy. *Magn. Reson. Med.*, 36(4):562–566, Oct 1996.
- [48] M. N. Yongbi, C. A. Branch, and J. A. Helpert. Perfusion imaging using FOCI RF pulses. *Magn. Reson. Med.*, 40(6):938–943, Dec 1998.
- [49] M. N. Yongbi, Y. Yang, J. A. Frank, and J. H. Duyn. Multislice perfusion imaging in human brain using the C-FOCI inversion pulse: comparison with hyperbolic secant. *Magn Reson Med*, 42(6):1098–1105, Dec 1999.
- [50] R. R. Edelman and Q. Chen. EPISTAR MRI: multislice mapping of cerebral blood flow. *Magn. Reson. Med.*, 40(6):800–805, Dec 1998.
- [51] X. Golay, M. Stuber, K. P. Pruessmann, D. Meier, and P. Boesiger. Transfer insensitive labeling technique (TILT): application to multislice functional perfusion imaging. *J. Magn. Reson. Imaging*, 9(3):454–461, Mar 1999.
- [52] K. K. Kwong, D. A. Chesler, R. M. Weisskoff, K. M. Donahue, T. L. Davis, L. Ostergaard, T. A. Campbell, and B. R. Rosen. MR perfusion studies with T1-weighted echo planar imaging. *Magn. Reson. Med.*, 34(6):878–887, Dec 1995.
- [53] S. G. Kim. Quantification of relative cerebral blood flow change by flow-sensitive alternating inversion recovery (FAIR) technique: application to functional mapping. *Magn. Reson. Med.*, 34(3):293–301, Sep 1995.
- [54] K. Oshio and D. A. Feinberg. GRASE (Gradient- and spin-echo) imaging: a novel fast MRI technique. *Magn. Reson. Med.*, 20(2):344–349, Aug 1991.

- [55] R. R. Edelman, B. Wallner, A. Singer, D. J. Atkinson, and S. Saini. Segmented turboFLASH: method for breath-hold MR imaging of the liver with flexible contrast. *Radiology*, 177(2):515–521, Nov 1990.
- [56] K. Scheffler, O. Heid, and J. Hennig. Magnetization preparation during the steady state: fat-saturated 3D TrueFISP. *Magn. Reson. Med.*, 45(6):1075–1080, Jun 2001.
- [57] F. S. Pereles, V. Kapoor, J. C. Carr, O. P. Simonetti, E. A. Krupinski, V. Baskaran, and J. P. Finn. Usefulness of segmented trueFISP cardiac pulse sequence in evaluation of congenital and acquired adult cardiac abnormalities. *AJR Am. J. Roentgenol.*, 177(5):1155–1160, Nov 2001.
- [58] S. G. Kim, N. V. Tsekos, and J. Ashe. Multi-slice perfusion-based functional MRI using the FAIR technique: comparison of CBF and BOLD effects. *NMR Biomed.*, 10(4-5):191–196, 1997.
- [59] S. G. Kim and K. Ugurbil. Comparison of blood oxygenation and cerebral blood flow effects in fMRI: estimation of relative oxygen consumption change. *Magn. Reson. Med.*, 38(1):59–65, Jul 1997.
- [60] J. Hendrikse, M. J. P. van Osch, D. R. Rutgers, C. J. G. Bakker, L. J. Kappelle, X. Golay, and J. van der Grond. Internal carotid artery occlusion assessed at pulsed arterial spin-labeling perfusion MR imaging at multiple delay times. *Radiology*, 233(3):899–904, Dec 2004. URL <http://dx.doi.org/10.1148/radiol.2333031276>.
- [61] J. Hendrikse, J. van der Grond, H. Lu, P. C. M. van Zijl, and X. Golay. Flow territory mapping of the cerebral arteries with regional perfusion MRI. *Stroke*, 35(4):882–887, Apr 2004. URL <http://dx.doi.org/10.1161/01.STR.0000120312.26163.EC>.

- [62] A. P. Kansagra and E. C. Wong. Quantitative assessment of mixed cerebral vascular territory supply with vessel encoded arterial spin labeling MRI. *Stroke*, 39(11):2980–2985, Nov 2008. URL <http://dx.doi.org/10.1161/STROKEAHA.108.515767>.
- [63] A. P. Kansagra and E. C. Wong. Mapping of vertebral artery perfusion territories using arterial spin labeling MRI. *J. Magn. Reson. Imaging*, 28(3):762–766, Sep 2008. URL <http://dx.doi.org/10.1002/jmri.21462>.
- [64] P. Martirosian, U. Klose, I. Mader, and F. Schick. FAIR true-FISP perfusion imaging of the kidneys. *Magn. Reson. Med.*, 51(2):353–361, Feb 2004. URL <http://dx.doi.org/10.1002/mrm.10709>.
- [65] S. Ogawa, T. M. Lee, A. S. Nayak, and P. Glynn. Oxygenation-sensitive contrast in magnetic resonance image of rodent brain at high magnetic fields. *Magn. Reson. Med.*, 14(1):68–78, Apr 1990.
- [66] S. Ogawa and T. M. Lee. Magnetic resonance imaging of blood vessels at high fields: *in vivo* and *in vitro* measurements and image simulation. *Magn. Reson. Med.*, 16(1):9–18, Oct 1990.
- [67] S. Ogawa, T. M. Lee, A. R. Kay, and D. W. Tank. Brain magnetic resonance imaging with contrast dependent on blood oxygenation. *Proc. Natl. Acad. Sci. U.S.A.*, 87(24):9868–9872, Dec 1990.
- [68] S. Ogawa, D. W. Tank, R. Menon, J. M. Ellermann, S. G. Kim, H. Merkle, and K. Ugurbil. Intrinsic signal changes accompanying sensory stimulation: functional brain mapping with magnetic resonance imaging. *Proc. Natl. Acad. Sci. U.S.A.*, 89(13):5951–5955, Jul 1992.
- [69] E. Yacoub and X. Hu. Detection of the early decrease in fMRI signal in the motor area. *Magn. Reson. Med.*, 45(2):184–190, Feb 2001.

- [70] E. Yacoub, A. Shmuel, J. Pfeuffer, P. F. Van De Moortele, G. Adriany, K. Ugurbil, and X. Hu. Investigation of the initial dip in fMRI at 7 Tesla. *NMR Biomed.*, 14(7-8):408–412, 2001.
- [71] Y. Behzadi and T. T. Liu. Caffeine reduces the initial dip in the visual BOLD response at 3 T. *Neuroimage*, 32(1):9–15, Aug 2006. URL <http://dx.doi.org/10.1016/j.neuroimage.2006.03.005>.
- [72] J. B. Mandeville, J. J. Marota, C. Ayata, G. Zaharchuk, M. A. Moskowitz, B. R. Rosen, and R. M. Weisskoff. Evidence of a cerebrovascular postarteriole windkessel with delayed compliance. *J. Cereb. Blood Flow Metab.*, 19(6):679–689, Jun 1999. URL <http://dx.doi.org/10.1097/00004647-199906000-00012>.
- [73] Hanzhang Lu, Xavier Golay, James J Pekar, and Peter C M Van Zijl. Sustained poststimulus elevation in cerebral oxygen utilization after vascular recovery. *J. Cereb. Blood Flow Metab.*, 24(7):764–770, Jul 2004.
- [74] R. B. Buxton, E. C. Wong, and L. R. Frank. Dynamics of blood flow and oxygenation changes during brain activation: the balloon model. *Magn. Reson. Med.*, 39(6):855–864, Jun 1998.
- [75] K. L. Miller, W. M. Luh, T. T. Liu, A. Martinez, T. Obata, E. C. Wong, L. R. Frank, and R. B. Buxton. Nonlinear temporal dynamics of the cerebral blood flow response. *Hum. Brain Mapp.*, 13(1):1–12, May 2001.
- [76] Y. Behzadi and T. T. Liu. An arteriolar compliance model of the cerebral blood flow response to neural stimulus. *Neuroimage*, 25(4):1100–1111, May 2005. URL <http://dx.doi.org/10.1016/j.neuroimage.2004.12.057>.

- [77] A. Zakhor, R. Weisskoff, and R. Rzedzian. Optical sampling and reconstruction of MRI signals resulting from sinusoidal gradients. *IEEE Trans. Signal Proc.*, 39:2056, 1991.
- [78] H. Bruder, H. Fischer, H. E. Reinfelder, and F. Schmitt. Image reconstruction for echo planar imaging with nonequidistant k-space sampling. *Magn. Reson. Med.*, 23:311–323, 1992.
- [79] J. K. Maier, M. Vavrek, and G. H. Glover. Correction of mri data acquired by an echo-planar technique. U.S. Patent 5151656, 1992.
- [80] F. Schmitt and G. Goertler. Method for suppressing image artifacts in a magnetic resonance imaging apparatus. U.S. Patent 5138259, 1992.
- [81] A. G. Gardener, P. A. Gowland, and S. T. Francis. Implementation of quantitative perfusion imaging using pulsed arterial spin labeling at ultra-high field. *Magn. Reson. Med.*, 61(4):874–882, Apr 2009. URL <http://dx.doi.org/10.1002/mrm.21796>.
- [82] C. Triantafyllou, R. D. Hoge, G. Krueger, C. J. Wiggins, A. Potthast, G. C. Wiggins, and L. L. Wald. Comparison of physiological noise at 1.5 T, 3 T and 7 T and optimization of fMRI acquisition parameters. *Neuroimage*, 26(1):243–250, May 2005. URL <http://dx.doi.org/10.1016/j.neuroimage.2005.01.007>.
- [83] G. H. Glover, T. Q. Li, and D. Ress. Image-based method for retrospective correction of physiological motion effects in fMRI: RETROICOR. *Magn. Reson. Med.*, 44(1):162–167, Jul 2000.
- [84] Y. Behzadi, K. Restom, J. Liau, and T. T. Liu. A component based noise correction method (CompCor) for BOLD and perfusion based fMRI. *Neuroimage*, 37(1):90–101, Aug 2007. URL <http://dx.doi.org/10.1016/j.neuroimage.2007.04.042>.

- [85] D. M. Garcia, G. Duhamel, and D. C. Alsop. Efficiency of inversion pulses for background suppressed arterial spin labeling. *Magn Reson Med*, 54(2):366–372, Aug 2005. URL <http://dx.doi.org/10.1002/mrm.20556>.
- [86] J. Pfeuffer, G. Adriany, A. Shmuel, E. Yacoub, P.-E. van de Moortele, X. Hu, and K. Ugurbil. Perfusion-based high-resolution functional imaging in the human brain at 7 Tesla. *Magn. Reson. Med.*, 47(5):903–911, May 2002. URL <http://dx.doi.org/10.1002/mrm.10154>.
- [87] T. L. Davis, K. K. Kwong, R. M. Weisskoff, and B. R. Rosen. Calibrated functional MRI: mapping the dynamics of oxidative metabolism. *Proc. Natl. Acad. Sci. U.S.A.*, 95(4):1834–1839, Feb 1998.
- [88] R. D. Hoge, J. Atkinson, B. Gill, G. R. Crelier, S. Marrett, and G. B. Pike. Investigation of BOLD signal dependence on cerebral blood flow and oxygen consumption: the deoxyhemoglobin dilution model. *Magn. Reson. Med.*, 42(5):849–863, Nov 1999.
- [89] R. D. Hoge, J. Atkinson, B. Gill, G. R. Crelier, S. Marrett, and G. B. Pike. Linear coupling between cerebral blood flow and oxygen consumption in activated human cortex. *Proc. Natl. Acad. Sci. U.S.A.*, 96(16):9403–9408, Aug 1999.
- [90] S. Naganawa, T. Ito, E. Iwayama, H. Fukatsu, T. Ishiguchi, T. Ishigaki, and N. Ichinose. Magnitude subtraction vs. complex subtraction in dynamic contrast-enhanced 3D-MR angiography: basic experiments and clinical evaluation. *J. Magn. Reson. Imaging*, 10(5):813–820, Nov 1999.
- [91] Y. Zhang, H. K. Song, J. Wang, A. Techawiboonwong, and F. W. Wehrli. Spatially-confined arterial spin-labeling with FAIR. *J. Magn. Reson. Imag.*, 22(1):119–124, Jul 2005. URL <http://dx.doi.org/10.1002/jmri.20362>.

- [92] T. Kim, K. S. Hendrich, K. Masamoto, and S.-G. Kim. Arterial versus total blood volume changes during neural activity-induced cerebral blood flow change: implication for BOLD fMRI. *J. Cereb. Blood Flow Metab.*, 27(6):1235–1247, Jun 2007. URL <http://dx.doi.org/10.1038/sj.jcbfm.9600429>.
- [93] T. Kim and S.-G. Kim. Quantification of cerebral arterial blood volume using arterial spin labeling with intravoxel incoherent motion-sensitive gradients. *Magn. Reson. Med.*, 55(5):1047–1057, May 2006. URL <http://dx.doi.org/10.1002/mrm.20867>.
- [94] F. Q. Ye, V. S. Mattay, P. Jezzard, J. A. Frank, D. R. Weinberger, and A. C. McLaughlin. Correction for vascular artifacts in cerebral blood flow values measured by using arterial spin tagging techniques. *Magn. Reson. Med.*, 37(2):226–235, Feb 1997.
- [95] http://kvhs.nbed.nb.ca/gallant/biology/blood_vessels.html, last seen: November 2009.
- [96] M. J. Brookes, P. G. Morris, P. A. Gowland, and S. T. Francis. Noninvasive measurement of arterial cerebral blood volume using Look-Locker EPI and arterial spin labeling. *Magn. Reson. Med.*, 58(1):41–54, Jul 2007. URL <http://dx.doi.org/10.1002/mrm.21199>.
- [97] S. T. Francis, R. Bowtell, and P. A. Gowland. Modeling and optimization of Look-Locker spin labeling for measuring perfusion and transit time changes in activation studies taking into account arterial blood volume. *Magn. Reson. Med.*, 59(2):316–325, Feb 2008. URL <http://dx.doi.org/10.1002/mrm.21442>.

- [98] E. T. Petersen, T. Lim, and X. Golay. Model-free arterial spin labeling quantification approach for perfusion MRI. *Magn. Reson. Med.*, 55(2): 219–232, Feb 2006. URL <http://dx.doi.org/10.1002/mrm.20784>.
- [99] P. Herscovitch and M. E. Raichle. What is the correct value for the brain–blood partition coefficient for water? *J. Cereb. Blood Flow Metab.*, 5(1): 65–69, Mar 1985.
- [100] E. L. Barbier, A. C. Silva, S. G. Kim, and A. P. Koretsky. Perfusion imaging using dynamic arterial spin labeling (DASL). *Magn. Reson. Med.*, 45(6):1021–1029, Jun 2001.
- [101] R. L. Grubb, M. E Raichle, J. O. Eichling, and M. M. Ter-Pogossian. The effect of changes in PaCO₂ on cerebral blood volume, blood flow, and vascular mean transit time. *Stroke*, 5:630–639, 1974.
- [102] N. P. Blockley, S. T. Francis, and P. A. Gowland. Perturbation of the BOLD response by a contrast agent and interpretation through a modified balloon model. *Neuroimage*, 48(1):84–93, Oct 2009. URL <http://dx.doi.org/10.1016/j.neuroimage.2009.06.038>.
- [103] R. B. Buxton, K. Uludag, D. J. Dubowitz, and T. T. Liu. Modeling the hemodynamic response to brain activation. *Neuroimage*, 23 Suppl 1: S220–S233, 2004. URL <http://dx.doi.org/10.1016/j.neuroimage.2004.07.013>.
- [104] M. J. Donahue, R. D. Stevens, M. de Boorder, J. J. Pekar, J. Hendrikse, and P. C. M. van Zijl. Hemodynamic changes after visual stimulation and breath holding provide evidence for an uncoupling of cerebral blood flow and volume from oxygen metabolism. *J. Cereb. Blood Flow Metab.*, 29(1):176–185, Jan 2009. URL <http://dx.doi.org/10.1038/jcbfm.2008.109>.

- [105] Q. Shen, H. Ren, and T. Q. Duong. CBF, BOLD, CBV, and CMRO(2) fMRI signal temporal dynamics at 500-msec resolution. *J. Magn. Reson. Imaging*, 27(3):599–606, Mar 2008. URL <http://dx.doi.org/10.1002/jmri.21203>.
- [106] A.-L. Lin, P. T. Fox, Y. Yang, H. Lu, L.-H. Tan, and J.-H. Gao. Evaluation of MRI models in the measurement of CMRO₂ and its relationship with CBF. *Magn. Reson. Med.*, 60(2):380–389, Aug 2008. URL <http://dx.doi.org/10.1002/mrm.21655>.
- [107] C. Iadecola, G. Yang, T. J. Ebner, and G. Chen. Local and propagated vascular responses evoked by focal synaptic activity in cerebellar cortex. *J Neurophysiol*, 78(2):651–659, Aug 1997.
- [108] B. Stefanovic and G. B. Pike. Venous refocusing for volume estimation: VERVE functional magnetic resonance imaging. *Magn. Reson. Med.*, 53(2):339–347, Feb 2005. URL <http://dx.doi.org/10.1002/mrm.20352>.
- [109] J. J. Chen and Pike G. B. Dynamic measurement of functional changes in venous blood volume at 3 T. In *Proceedings of the 15th Meeting of the ISMRM*, page 2617. Berlin, 2007.
- [110] R. P. Kennan, B. E. Scanley, and J. C. Gore. Physiologic basis for BOLD MR signal changes due to hypoxia/hyperoxia: separation of blood volume and magnetic susceptibility effects. *Magn. Reson. Med.*, 37(6):953–956, Jun 1997.
- [111] K. Scheffler, E. Seifritz, R. Haselhorst, and D. Bilecen. Titration of the BOLD effect: separation and quantitation of blood volume and oxygenation changes in the human cerebral cortex during neuronal activation and ferumoxide infusion. *Magn. Reson. Med.*, 42(5):829–836, Nov 1999.

- [112] J. A. Pears, S. T. Francis, S. E. Butterworth, R. W. Bowtell, and P. A. Gowland. Investigating the BOLD effect during infusion of Gd-DTPA using rapid T_2^* mapping. *Magn. Reson. Med.*, 49(1):61–70, Jan 2003. URL <http://dx.doi.org/10.1002/mrm.10340>.
- [113] K. A. Rempp, G. Brix, F. Wenz, C. R. Becker, F. Gckel, and W. J. Lorenz. Quantification of regional cerebral blood flow and volume with dynamic susceptibility contrast-enhanced MR imaging. *Radiology*, 193(3):637–641, Dec 1994.
- [114] B. R. Rosen, J. W. Belliveau, J. M. Vevea, and T. J. Brady. Perfusion imaging with NMR contrast agents. *Magn. Reson. Med.*, 14(2):249–265, May 1990.
- [115] A. Kastrup, G. Krger, T. Neumann-Haefelin, G. H. Glover, and M. E. Moseley. Changes of cerebral blood flow, oxygenation, and oxidative metabolism during graded motor activation. *Neuroimage*, 15(1):74–82, Jan 2002. URL <http://dx.doi.org/10.1006/nimg.2001.0916>.
- [116] P. A. Chiarelli, D. P. Bulte, D. Gallichan, S. K. Piechnik, R. Wise, and P. Jezard. Flow-metabolism coupling in human visual, motor, and supplementary motor areas assessed by magnetic resonance imaging. *Magn. Reson. Med.*, 57(3):538–547, Mar 2007. URL <http://dx.doi.org/10.1002/mrm.21171>.
- [117] H. Ito, K. Takahashi, J. Hatazawa, S. G. Kim, and I. Kanno. Changes in human regional cerebral blood flow and cerebral blood volume during visual stimulation measured by positron emission tomography. *J. Cereb. Blood Flow Metab.*, 21(5):608–612, May 2001. URL <http://dx.doi.org/10.1097/00004647-200105000-00015>.

- [118] H. Ito, I. Kanno, M. Ibaraki, J. Hatazawa, and S. Miura. Changes in human cerebral blood flow and cerebral blood volume during hypercapnia and hypocapnia measured by positron emission tomography. *J. Cereb. Blood Flow Metab.*, 23(6):665–670, Jun 2003. URL <http://dx.doi.org/10.1097/01.WCB.0000067721.64998.F5>.
- [119] E. Rostrup, G. M. Knudsen, I. Law, S. Holm, H. B. W. Larsson, and O. B. Paulson. The relationship between cerebral blood flow and volume in humans. *Neuroimage*, 24(1):1–11, Jan 2005. URL <http://dx.doi.org/10.1016/j.neuroimage.2004.09.043>.
- [120] Y. C. Fung. *Biomechanics: Circulation*. Springer-Verlag, New York, 1997.